

**MBE growth, Fabrication, and Electrical Characterisation of
Terahertz Frequency Quantum Cascade Lasers**

Jingxuan Zhu

Submitted in accordance with the requirements for the degree of
Doctor of Philosophy

The University of Leeds
Institution of Microwaves and Photonics
Electronic and Electrical Engineering

December, 2015

The candidate confirms that the work submitted is her own, except where work which has formed part of jointly-authored publications has been included. The contribution of the candidate and the other authors to this work has been explicitly indicated below. The candidate confirms that appropriate credit has been given within the thesis where reference has been made to the work of others.

The work in Chapter 2 and Chapter 4 of the thesis has appeared in publications as follows:

- [1] L. H. Li, J. Zhu, L. Chen, A. G. Davies, E. H. Linfield, The MBE growth and optimization of high performance terahertz frequency quantum cascade lasers, *Optics Express*, Vol. 23, No.3, 2720-2729, (2015).
- [2] L. H. Li, L. Chen, J. Zhu, J. Freeman, P. Dean, A. Valavanis, A. G. Davies, E. H. Linfield, Terahertz quantum cascade lasers with > 1 W output powers, *Electronics Letters*, Vol. 50, No. 4, 309-311, (2014).
- [3] Y. Halioua, G. Xu, S. Moudji, L. Li, J. Zhu, E. H. Linfield, A. G. Davies, H. E. Beere, D. A. Ritchie, R. Colombelli, Phase-locked arrays of surface-emitting graded-photonic-heterostructure terahertz semiconductor lasers, *Optics Express*, Vol. 23, No. 5, (2015).
- [4] A. Valavanis, Y. J. Han, N. Brewster, P. Dean, R. Dong, L. Bushnell, M. Oldfield, J. Zhu, L. H. Li, A. G. Davies, B. Ellison and E. H. Linfield, Mechanically robust waveguide integration and beam shaping of terahertz quantum cascade lasers, *Electronics Letters*, Vol. 51, No. 13, (2015).
- [5] T. Fobbe, H. Nong, R. Schott, S. Pal, S. Markmann, N. Hekmat, J. Zhu, Y. Han, L. H. Li, P. Dean, E. H. Linfield, A. G. Davies, A. D. Wieck, and N. Jukam, Improving the out-coupling of a metal-metal terahertz frequency quantum cascade laser through integration of a hybrid mode section into the waveguide, submitted to *Applied Physics Letters*.
- [6] J. Zhu, L. H. Li, P. Dean, E. H. Linfield, and A. G. Davies, Growth and Optimization of Terahertz frequency quantum cascade lasers, UK Semiconductors, Sheffield, (2013).
- [7] J. Zhu, L. H. Li, L. Chen, J. Freeman, P. Dean, A. Valavanis, A. G. Davies, E. H. Linfield, Terahertz-frequency quantum cascade lasers with >1-watt output power, UK Semiconductors, Sheffield, (2014).
- [8] L. H. Li, L. Chen, J. Zhu, J. R. Freeman, P. Dean, A. Valavanis, A. G. Davies, E. H. Linfield, THz quantum cascade lasers with output power over

1 W, IQCLSW2014 International Quantum Cascade Lasers School and Workshop, (2014).

[9] Y. J. Han, L. H. Li, J. Zhu, A. Valavanis, J. R. Freeman, P. Dean, A. G. Davies, E. H. Linfield, Silver-based surface plasmon waveguide for terahertz quantum cascade lasers, IQCSLW2014 International Quantum Cascade Lasers School and Workshop, (2014).

[10] D. Rui, Y. Han, I. Kundu, N. Brewster, L. Li, L. Chen, J. Zhu, L. Bushnell, M. Oldfield, et al., Waveguide-integrated terahertz-frequency quantum cascade lasers for trace-gas detection applications, UK semiconductors, (2015).

[11] A. Valavanis, Y. J. Han, N. Brewster, P. Dean, R. Dong, L. Bushnell, M. Oldfield, J. Zhu, L. H. Li, A. G. Davies, B. N. Ellison and E. H. Linfield, A robust waveguide integration, beam shaping and heat-sinking scheme for terahertz quantum cascade lasers, ITQW , (2015).

[12] A. Valavanis, P. Dean, L. H. Li, A. D. Burnett, J. Keeley, S. Chowdhury, R. Alhathloul, L. Chen, J. Zhu, Y. J. Han, et.al. High-power(>1-Watt) terahertz frequency quantum cascade lasers for stand-off imaging, SET-210 Specialist Meeting on Novel Infrared laser technology for modern battlefield requirements, Salisbury, UK, (2014).

For the above jointly-authored publications [3-5] and [9-12], I have contributed in the MBE growth and THz QCL device fabrications. For publications [1-2] and [6-8], my contributions include MBE growth, THz QCL device fabrication and characterisation.

This copy has been supplied on the understanding that it is copyright material and that no quotation from the thesis may be published without proper acknowledgement.

Assertion of moral rights:

The right of Jingxuan Zhu to be identified as author of this work has been asserted by her in accordance with the Copyright, Designs and Patents Act 2015.

Acknowledgements

I would like to express my gratitude to my supervisors Prof. E. H. Linfield, Prof. A. G. Davies and Prof. John Cunningham for their guidance and support during my PhD study. I gratefully acknowledge Dr. Lianhe Li who trained me on MBE growth and also gave me valuable advice.

I would like to thank many colleagues in my group: Dr. Paul Dean; Dr. Alexander Valavanis; Dr. Yingjun Han and Dr. Joshua Freeman, for their suggestions and assistance in my QCL characterisation, data analysis and thesis writing, and also Dr. Iman Kundu for the help in QCL band structure simulation, fabrication, and valuable comments in my thesis; Dr. Raed Alhathloul and Dr. Mohammed Salih; Mr. Dong Rui, and Ms. Reshma Anamari Mohandas, for their help with QCL device fabrication and measurement. I appreciate the help from Dr. Li Chen and Mr. Geoff Butterworth in the clean room training, and acknowledge Dr. Wilson Muchenje and Dr. Chris Russell for their assistance in electrical characterisations.

Thanks also to Mr. Peter Lynch MA for language corrections. I would also like to thank my family, and friends Ms. Weixi Chen, and Ms. Nini Chen for their support.

Abstract

The terahertz (THz) range in the electromagnetic radiation spectrum lies between the high-frequency edge of the microwave band and the long-wavelength edge of the far-infrared band. THz technology is important for both scientific and commercial applications so the production of coherent, high power sources operating at room temperature is of great interest. Quantum cascade lasers (QCLs) are unipolar emitters operating from THz to infrared range. Molecular beam epitaxy (MBE) is the main technique for the growth of THz QCLs, offering precise control of layer thickness and composition under ultra-high vacuum conditions.

The output power, maximum operating temperature, threshold and dynamic range are essential parameters in THz QCL performances. Since high power in THz QCLs is a desirable performance in particular to areas such as imaging and remote sensing. The threshold and dynamic ranges are influenced by the injector doping levels determining the losses. Moreover, the interface roughness affects the electrical and optical properties of semiconductor devices, which can be improved by misorientation of (100) GaAs substrates.

This thesis reviews the development of THz QCLs, investigates MBE growth, fabrication and electrical characterisation process, and the enhancement of THz QCL performances. Chapter 1 summarizes the development and application of THz technology, different THz sources, as well as the development of THz QCLs. Chapter 2 outlines the MBE system, and investigates the calibration methods, the growth process, and growth reproducibility. Chapter 3 explains the fabrication techniques, electrical characterisation of THz QCLs, and the factors that influence the device performance. Chapter 4 investigates the enhancement in THz QCL power performance; whilst Chapter 5 probes the injector doping effects and background impurity level influences on BTC and hybrid THz QCL performance. In Chapter 6, the effects and possible significance of misorientation on THz QCLs are discussed. Chapter 7 concludes the thesis and suggests future directions.

Table of Contents

Acknowledgements	iv
Abstract.....	v
Table of Contents	vi
List of Tables	ix
List of Figures	xi
Chapter 1 Introduction.....	1
1.1 THz sources and applications	2
1.1.1 THz sources	2
1.1.2 THz applications	3
1.2 THz QCLs	5
1.2.1 Development of QCLs.....	5
1.2.2 Active regions	8
1.2.3 Material system for THz QCLs.....	11
1.3 Thesis outline	12
Chapter 2 Molecular beam epitaxy	14
2.1 Introduction	15
2.2 MBE system.....	15
2.3 Calibration.....	17
2.3.1 Flux measurement	17
2.3.2 Growth rate calibration.....	18
2.4 Silicon doping calibration	21
2.4.1 Hall measurement.....	21
2.4.2 SIMS calibration method.....	25
2.5 Growth of THz QCLs.....	28
2.5.1 Growth procedure	28
2.5.2 Growth rate control of THz QCLs.....	30
2.5.3 Layer thickness control and growth reproducibility	33
2.6 Summary.....	37
Chapter 3 Fabrication and electrical characterisation of THz QCLs	39
3.1 Waveguides of THz QCLs	40
3.2 Fabrication of THz QCLs	41
3.2.1 Fabrication procedures	42

3.2.2 Photolithography	47
3.2.3 Wet etching	48
3.2.4 Ohmic contacts	50
3.3 Electrical characterisation of THz QCLs	51
3.4 Summary.....	53
Chapter 4 High power THz QCLs	54
4.1 Introduction	55
4.2 Active region structure	56
4.3 Modeling and simulation	57
4.3.1 SISP Waveguide simulation introduction	57
4.3.2 SISP Waveguide simulation result	59
4.4 Experimental results	63
4.4.1 Device measurement.....	63
4.4.2 Comparison between simulation and experimental results	63
4.4.3 Summary of results for different cavity lengths/widths	65
4.4.4 Facet coating and increasing of the device performance.....	66
4.4.5 Threshold current density dependence on device area	71
4.4.6 Output power dependence on device area	75
4.4.7 Maximum operating temperature dependence on device area	78
4.5 Summary	80
Chapter 5 Optimized of BTC and hybrid THz QCLs	81
5.1 Introduction	82
5.1.1 Historical review.....	82
5.1.2 Fabrication and measurement	83
5.2 Injector doping	83
5.2.1 Theoretical analysis	83
5.2.2 Active regions	85
5.2.3 Hybrid structure.....	87
5.2.4 Other BTC designs	90
5.2.5 CW operation	93
5.2.6 Temperature performance	97
5.3 Background doping	100
5.4 Summary	104

Chapter 6 THz QCLs on misorientated substrates	105
6.1 Historial review on misorientation	106
6.1.1 Interface roughness	106
6.1.2 Effects of misorientation.....	107
6.1.3 Chapter outline.....	107
6.2 Misorientation and growth mechanism	108
6.2.1 Introduction	108
6.2.2 Surface morphology.....	110
6.3 BTC THz QCLs on misorientated substrates.....	112
6.3.1 Active region structure	112
6.3.2 Results and analysis.....	113
6.4 Hybrid THz QCLs on misorientated substrates.....	117
6.4.1 Spectral property.....	118
6.4.2 Maximum operating temperature	119
6.4.3 Threshold and dynamic range	120
6.4.4 Power performance.....	122
6.5 Summary.....	123
Chapter 7 Conclusion and further work.....	125
7.1 Conclusions	126
7.1.1 Optimization of material quality.....	126
7.1.2 Optimization of device performances.....	128
7.2 Further work.....	129
Bibliography	131
List of Abbreviations	142
List of Symbols	144
Appendix A	146
A.1 Fabrication procedures for SISP THz QCLs.....	146
A.2 Fabrication procedures for DM THz QCLs	149

List of Tables

Table 2.1: Sample geometry and fabrication for VDP Hall measurement.....	23
Table 2.2: Required equipment of VDP Hall measurement.	24
Table 2.3: Structure and growth parameters of typical THz QCLs reported in the literature.	35
Table 3.1: Schematic cross view and microscope photographs of SISF QCL fabrication.....	45
Table 3.2: Main steps of DM THz QCL fabrication.	47
Table 4.1: Threshold gain for devices at different cavity lengths and ridge widths.	62
Table 4.2: Performance of THz QCLs with different ridge widths, for a device Length of 1.5 mm.	65
Table 4.3: Performance of THz QCLs with different ridge widths for a device. Length of 1 mm.	65
Table 5.1: Details of 3.5 THz BTC QCL devices (L1152 and L1171).	90
Table 5.2: Details of 3.1 THz QCL devices (L1153 and L1154).	91
Table 5.3: Hybrid THz QCL wafers with different injector doping levels.	97
Table 5.4: Hybrid THz QCL wafers with different sheet carrier densities.	99
Table 6.1: Measurement details of structure L904 on different misorientated substrates.	113

Table 6.2: Details of 2-mm long and 3-mm long L989 devices. 118

List of Figures

Fig. 1.1 The ‘THz gap’ in the electromagnetic spectrum.	2
Fig. 1.2: Conduction-band diagram and electron subband wave functions squared, calculated self-consistently using Schrödinger–Poisson solver [1] of a typical CSL QCL active region design.	10
Fig. 1.3: Conduction-band diagram and electron subband wave functions squared, calculated self-consistently using Schrödinger–Poisson solver [1] of a typical BTC QCL active region design.	10
Fig. 1.4: Conduction-band diagram and electron subband wave functions squared, calculated self-consistently using Schrödinger–Poisson solver [1] of a typical RP QCL active region design.	11
Fig. 1.5: Conduction-band diagram and electron subband wave functions squared, calculated self-consistently using Schrödinger–Poisson solver [1] of a typical hybrid QCL active region design.	11
Fig. 2.1: Part view of an MBE system illustrating the configuration of the major components.	16
Fig. 2.2: Principle of MBE. [2][45]	16
Fig. 2.3: Measured As BEP at different valve positions.	18
Fig. 2.4: Schematic illustration of the mechanism responsible for pyrometric oscillations.	19
Fig. 2.5: Pyrometric intensity oscillation for GaAs and AlGaAs layers, grown on top of an AlAs layer, itself deposited on a GaAs substrate. The Al cell temperature was=1184 °C, the Ga temperature 949 °C.	20

Fig. 2.6: Line profile of pyrometric intensity oscillations for GaAs and AIAs at a wavelength of=1220 nm, extracted from Fig. 2.5, the AIAs growth rate was 0.42 $\mu\text{m/hr}$, the GaAs growth rate 0.968 $\mu\text{m/hr}$.	20
Fig. 2.7: Dependence of GaAs growth rate on Ga cell temperature..	21
Fig. 2.8: Schematic diagram of the Hall effect.....	22
Fig. 2.9: Schematic diagram of VDP Hall resistance measurements.	23
Fig. 2.10: Resistance between two indium contacts as a function of doping concentration.	24
Fig. 2.11: Doping concentration measured at different depths of a sample, (a) L834, (b) L837.	26
Fig. 2.12: Doping concentration as a function of temperature for (a) L834, and (b) L837. Main figures show the doping concentration from all data, normalized to 1 $\mu\text{m}/\text{hour}$.	27
Fig. 2.13: Carrier/doping concentration as a function of silicon cell temperature.	27
Fig. 2.14: Flow chart of the QCL growth process.	29
Fig. 2.15: Experimental curves measured from calibration samples. Each curve is offset for clarity. (a) Typical oscillation curves at a wavelength of 1200 nm acquired by pyrometric spectrometer during growth. The blue curves originate from the growth of the thick $\text{Al}_x\text{Ga}_{1-x}\text{As}$ layers, whilst the red curves originate from the growth of the SPLs. (b) (004) x-ray diffraction curves taken after the sample growths.	31

Fig. 2.16: $\text{Al}_x\text{Ga}_{1-x}\text{As}$ refractive indices at a growth temperature of 600 °C. (a) The refractive index as a function of wavelength for different Al mole fractions, and (b) the dependence of the refractive index on the Al composition. Solid black circles and line are experimental data and the least fitting curve respectively, obtained at the growth temperature of 600 °C. The coloured curves are theoretical calculations according to [57]...... 32

Fig. 2.17: Typical variation of the Ga cell temperature required to achieve a 1 $\mu\text{m}/\text{hour}$ GaAs growth rate as a function of the total thickness of deposited GaAs during a growth run. Each data point corresponds to a single wafer growth. The Al data reflects the cell temperature required to achieve a constant growth rate of 0.176 $\mu\text{m}/\text{hr}$, as used for the majority of THz QCL growths. The Al data points thus correspond to THz QCL growths during the run—other device structures require different Al mole fractions. 34

Fig. 2.18: Typical pyrometric oscillations recorded during growth of a THz QCL structure using growth rate compensation. Theoretical simulation assumed a constant G_{QCL} of 1.036 $\mu\text{m}/\text{hr}$ 36

Fig. 2.19: Typical (004) x-ray diffraction curves taken from two THz QCLs with nominally identical structure but grown at different times. The active region is based on the design reported in [5]. The layer sequence of one period of the structure is 55/110/18/115/38/94/42/184 (starting from the injector barrier) where the thicknesses are in Å, and $\text{Al}_{0.15}\text{Ga}_{0.85}\text{As}$ layers are in bold type, GaAs layers are in regular, and the underlined layer is doped with Si. 37

Fig. 3.1 Schematic view of two QCL waveguides (left) and typical two-dimensional mode intensity pattern (right), (a) SISP waveguide, (b) DM waveguide. Taken from Ref. [83]. 40

Fig. 3.2 A microscope view (image scale: $\times 10$) showing proper and poor photolithography. 47

Fig. 3.3 Anisotropic etching, laser ridge vertical to wafer major flat (image scale: $\times 10$). 48

Fig. 3.4 GaAs substrate etching by (a) $\text{NH}_4\text{OH}:\text{H}_2\text{O}_2:\text{H}_2\text{O}=8:3:400$, (b) $\text{H}_2\text{SO}_4:\text{H}_2\text{O}_2:\text{H}_2\text{O}=1:8:40$ (image scale: $\times 50$).	48
Fig. 3.5 Surface after the laser ridge etching (sample L688) (image scale: $\times 10$).	49
Fig. 3.6 DM THz QCL ridge etching by $\text{H}_2\text{SO}_4:\text{H}_2\text{O}_2:\text{H}_2\text{O}=1:8:1$ (a) with some n+ GaAs material left (b) over etched surface (image scale: $\times 5$).	50
Fig. 3.7 Microscope view of an annealed surface of AuGeNi (image scale: $\times 10$).	51
Fig. 3.8 Experimental set-up for QCL characterisation.	52
Fig. 3.9 Comparison between the laser spectra and black body spectra (purged).	53
Fig. 4.1 Conduction-band diagram and electron subband wave functions squared at $T=10$ K, calculated self-consistently using Schrödinger–Poisson solver [1]. An electric field of 7.6 KV/cm is applied to align the structure. The GaAs/ $\text{Al}_{0.16}\text{Ga}_{0.84}\text{As}$ layer sequence of one period of the active layers starting from the injection barrier is: $52/103/17/107.5/36/88/39.5/172$, where the thicknesses are in Å, $\text{Al}_{0.16}\text{Ga}_{0.84}\text{As}$ barriers are in bold, and the underlined number correspond to a Si-doped layer with a concentration of $3 \times 10^{16} \text{ cm}^{-3}$	57
Fig. 4.2 Calculated mirror loss as a function of laser cavity length.	59
Fig. 4.3 (a) Schematics of the SISP waveguide (b) two-dimensional electromagnetic mode calculations for the fundamental lateral modes obtained using finite-element solver (COMSOL).	60
Fig. 4.4 2D confinement factor as a function of ridge width for active region doping levels of $3.5 \times 10^{16} \text{ cm}^{-3}$, and $4 \times 10^{16} \text{ cm}^{-3}$. The bottom contact doping is $3.5 \times 10^{18} \text{ cm}^{-3}$ and the laser cavity length was 1.5 mm.	61

Fig. 4.5 2D waveguide loss as a function of ridge width for active region doping levels of $3.5 \times 10^{16} \text{ cm}^{-3}$, and $4 \times 10^{16} \text{ cm}^{-3}$. The bottom contact doping is $3.5 \times 10^{18} \text{ cm}^{-3}$ and the laser cavity length was 1.5 mm.	61
Fig. 4.6 2D simulation results of threshold gain as a function of laser cavity length with ridge widths from 130 μm to 274 μm.	62
Fig. 4.7 Threshold gain as a function of laser ridge width for different cavity lengths with a plasma doping level at $3.5 \times 10^{18} \text{ cm}^{-3}$.	63
Fig. 4.8 Threshold current density as a function of laser cavity length for 145 μm and 426 μm ridge widths, at a heat-sink temperature of 10 K.	64
Fig. 4.9 Threshold current density as a function of laser cavity length at different heat-sink temperatures.	64
Fig. 4.10 L–I–V curves of a high power THz QCL (426 μm x 3 mm) with a hybrid THz QCL active region incorporating a single-quantum-well phonon extraction/injection stage. Results were measured with a 2% pulse duty cycle.	66
Fig. 4.11 Spectra recorded at 10 K with a 2% pulse duty cycle at different biases for a THz QCL of dimensions 426 μm x 3 mm.	66
Fig. 4.12 L–I–V curves of THz QCLs (L=1.8 mm, W=328 μm) obtained with a 2% pulse duty cycle at various heat-sink temperatures, (a) HR coated (b) uncoated.	68
Fig. 4.13 L-I-V characteristics comparison between facet coated and uncoated QCL devices for a cavity length of 1.8 mm, and a ridge width of 328 μm.	68
Fig 4.14 Threshold current density comparison between facet coated and uncoated devices as a function of temperature.	69
Fig. 4.15 Peak output power as a function of heat-sink temperature, (a) measured power, (b) normalized power.	70

Fig. 4.16 (a) L–I–V curves (b) spectra of THz QCLs (L = 4.2 mm, W = 426 μm) obtained with a 2% pulse duty cycle at various heat-sink temperatures.	71
Fig. 4.17 Threshold current density as function of heat-sink temperature, for a laser of width 426 μm, and ridge lengths of 1, 1.5, 3 mm.	72
Fig. 4.18 Threshold current density as function of heat-sink temperature, a laser width of 145 μm, and ridge lengths of 1, 1.5, 1.8, 2 mm.	72
Fig. 4.19 Threshold current density as a function of heat-sink temperature for 1.5 mm long lasers with ridge widths of 145, 174, 223, 374 and 426 μm.	73
Fig. 4.20 L–I–V curves of three THz QCLs (L=1.5 mm, W=145, 223, 426 μm) obtained with a 2% pulse duty cycle at heat-sink temperature of 10 K.	73
Fig. 4.21 Threshold current density as a function of laser area.	74
Fig. 4.22 Threshold current density as a function of inverse cavity length for devices with 145 μm ridge width and different cavity lengths.	74
Fig. 4.23 Peak power as a function of device ridge width.	75
Fig. 4.24 Peak power as a function of heat-sink temperature at different ridge widths (a) cavity length=1.5 mm (b) cavity length=1 mm.	76
Fig. 4.25 Peak power as a function of heat-sink temperature for a cavity width of 374 μm.	77
Fig. 4.26 Peak power as a function of device area.	77
Fig. 4.27 Threshold current density as a function of heat-sink temperature for different laser cavity lengths, ridge width=145 μm.	78

Fig. 4.28 Maximum operating temperature and T_0 as a function of laser cavity length.	79
Fig. 4.29 Maximum operating temperature as a function of device area.	80
Fig. 5.1 Conduction band diagram and electron subband wave functions squared calculated self-consistently using Schrödinger–Poisson solver of one period of the BTC THz QCL structure, with a single-quantum-well phonon extraction/injection stage under an applied electric field of 7.01 V. The layer sequence of one period of structure, in nanometers, right to left and starting from the injection barrier is 5.5/11.0/1.8/11.5/3.8/9.4/4.2/18.4 where $\text{Al}_{0.15}\text{Ga}_{0.85}\text{As}$ layers are in bold, and the doped layer is underlined. [47]	85
Fig. 5.2 Schematic conduction-band diagram of one stage of the structure under an average applied electric field of 2.55 KV/cm. The $\text{GaAs}/\text{Al}_{0.15}\text{Ga}_{0.85}\text{As}$ layer sequence of one period of active layers starting from injector barrier is as follows: 3.5/9.0/0.6/16.3/0.9/16.0/1.0/13.8/1.2/12.0/1.5/11.0/2.4/11.0/3.2/12.1 . Thicknesses are in nanometres, GaAs wells are in regular, $\text{Al}_{0.15}\text{Ga}_{0.85}\text{As}$ barriers in bold, and the doped layer is underlined, taken from Ref [106].	86
Fig. 5.3 Schematic conduction-band diagram of two stages of the structure under an applied electric field of 4.4 KV/cm. Layer sequence in nm is as follows: 10.1/0.5/16.2/1/12.9/2/11.8/3/9.5/3/8.6/3/7.1/3/17/3/14.5/4, (underlined layer is Si doped, figures in bold type are $\text{Al}_{0.15}\text{Ga}_{0.85}\text{As}$ layers), taken from Ref [46]	86
Fig. 5.4 Results of L916 with 3 mm length and 150 μm width measured with 2% duty cycle (a) L-I-V characteristics (b) threshold current density as a function of heat-sink temperature (c) spectral characteristic at heat-sink temperature of 10 K.	88
Fig. 5.5 (a) Current density as function of heat-sink temperature for devices with different injector doping levels. (b) Current density as a function of doping level, blue symbols represent maximum current density, pink symbols represent threshold current density. The lines are linear fits to the data.	89

Fig. 5.6 (a) Threshold current density as a function of heat-sink temperature for 3 mm L1152 and L1171. (b) L-I-V characteristics at heat-sink temperature of 10 K for 3 mm L1152 and L1171. Devices are measured in pulsed mode. Devices were measured in pulsed mode with 2% duty cycle. 91

Fig. 5.7 (a) Threshold current density as a function of heat-sink temperature for 1 mm L1153 and L1154, (a) threshold current density as a function of heat-sink temperature for 3 mm L1153 and L1154, (b) Length=3 mm, (c) L-I-V characteristics at heat-sink temperature of 10 K for 3 mm L1153 and L1154. Devices are measured in pulsed mode. Devices were measured in pulsed mode with 2% duty cycle. 93

Fig. 5.8 CW results of L1153 and L1154 devices, with length=3 mm and, width=150 μm , (a) spectra of L1153 (b) spectra of L1154 (c) L-I-V characteristics of L1153 (d) L-I-V characteristics of L1154. 94

Fig. 5.9 Threshold current density as a function of heat-sink temperature for L1153 and L1154 devices under CW mode, (a) Length=1 mm, width=150 μm (b) Length=3 mm, width=150 μm 95

Fig. 5.10 Comparison of threshold current density between pulsed and CW results at different heat-sink temperatures, (a) L1153, width=150 μm (b) L1154, width=150 μm 96

Fig. 5.11 (a) Maximum operating temperature as a function of injector doping level, (b) T_0 as a function of injector doping level. 98

Fig. 5.12 Threshold current density (J_{th}) and the maximum current density (J_{max}) at 78 K as a function of sheet carrier density of the active region. Samples were grown in Leeds and DM devices measured by E. Strupiechonski, Y. Halioua, G. Xu, R. Colombelli et al. in Universite Paris-Sud 11. 99

Fig. 5.13 Transit time as a function of sheet carrier density. 100

Fig. 5.14 Variation of (a) peak output power and (b) J_{\max} with injector doping level. The active region is based on hybrid design in [47]. Two Ga cells (Ga1, Ga2) were used for these growths. Ga1 had high purity, Ga2 was known to be contaminated and hence the GaAs was compensated and of low quality. The total unintentional doping from both cells was, however, $<2 \times 10^{14} \text{ cm}^{-3}$, – rather less than the intended injection level doping levels.	102
Fig. 5.15 L-I-V characteristic at the heat-sink temperature of 10 K for two lasers grown at different background doping levels.	103
Fig. 5.16 Peak power as a function of heat-sink temperature under two background doping levels: $1 \times 10^{13} \text{ cm}^{-3}$, and $2 \times 10^{14} \text{ cm}^{-3}$. ...	103
Fig. 6.1 A schematic diagram of misorientation. [113]	108
Fig. 6.2 A schematic diagram of step-flow growth.	109
Fig. 6.3 Epitaxial view of a 2-inch GaAs wafer.	109
Fig. 6.4 Surface profile image measured by AFM on L903 wafers with 0°, 2°, 4°, and 6° misorientation angles.	110
Fig. 6.5 Rms roughness as a function of mis-orientation angles.	111
Fig. 6.6 The improvement of surface roughness as a function of misorientation angle.	111
Fig. 6.7 Conduction-band diagram and electron subband wave functions squared, calculated self-consistently using Schrödinger–Poisson solver [1] of BTC structure of L904.	112
Fig. 6.8 Maximum operating temperature as a function of mis-orientation angle for L904.	114
Fig. 6.9 Threshold current density at 10 K as a function of misorientation angle.	114

Fig. 6.10 Peak power at heat-sink temperature of 10 K as a function of misorientation angle for wafer L904.	115
Fig. 6.11 Spectral characteristics of L904 (a) 0° off, 1.5 mm (b) 2° off, 1.5 mm (c) 4° off, 2 mm (d) 6° off, 2 mm.	116
Fig. 6.12 Current density as a function of heat-sink temperature for L904 for (a) 1.5 mm, (b) 2 mm, and (c) 3 mm-long devices. ..	117
Fig. 6.13 Spectral characteristics of L989 (a) 0° off, 2 mm (b) 4° off, 2 mm.	119
Fig. 6.14 Spectral characteristics of L903 (a) 0° off, 3 mm (b) 4° off, 3 mm.	119
Fig. 6.15 Maximum operating temperature as a function of misorientation angle for L989.	120
Fig. 6.16 Threshold current density as a function of misorientation angle for L989 with 150 μm width and 2 mm/3 mm cavity lengths.	120
Fig. 6.17 Threshold current density as a function of heat-sink temperature for L989 and L991 devices with 0° and 4° misorientation angles.	121
Fig. 6.18 J_{th} as a function of heat-sink temperature of wafer L991. ...	121
Fig. 6.19 Dynamic range as a function of heatsink temperature for L989 0° and 4° samples.	122
Fig. 6.20 Dynamic range as a function of heatsink temperature for L989 and L991 with 0° and 4° off samples.	123

Chapter 1

Introduction

1.1 THz sources and applications

The THz range of the electromagnetic radiation lies between the frequencies of 100 GHz to 10 THz (Fig. 1.1). It is between the high-frequency edge of the microwave band and the long-wavelength edge of the far-infrared band. [1] This region of the electro-magnetic spectrum has remained underdeveloped, due mainly to a lack of high power and convenient radiation sources. However, THz technology is important in both science and commercial applications, especially those related to spectroscopy and imaging. [2]

Owing to its shorter wavelength, THz radiation provides a better spatial resolution compared with microwaves. Comparing with imaging using high energy x-rays, THz imaging is non-invasive and can provide much better contrast in terms of identification of different materials, due to their largely different absorption and refraction indices across the THz spectrum. [3]

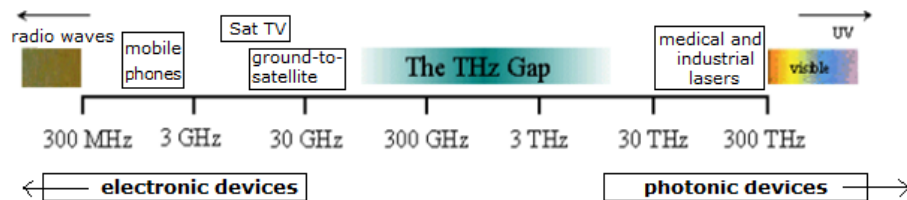


Figure 1.1 The 'THz gap' in the electromagnetic spectrum.

1.1.1 THz sources

Although a number of applications for THz radiation may use passive detection technology, such as heterodyne detection allowing for an improvement of many orders of magnitude in detection sensitivity, active sources are fundamental to improved detection and to many of the applications considered for THz radiation. High power, narrow line widths and high tunability of frequency are required for many of the potential THz applications. [4]

There are many sources of THz radiation. Vacuum electronic sources include the backward-wave oscillator, travelling-wave tubes, free-electron lasers and synchrotrons and so on. These sources typically are high

powered. Solid-state electronic sources include the Gunn diode and high-frequency transistors. Frequency multipliers are used to shift sub-THz radiation into the THz range. [5] Semiconductor lasers include electrically pumped photonic crystal lasers of low angular divergence. Much interest is currently in the QCL, a challenge being to raise the temperature of operation. [5]

Visible or near-infrared lasers, either operating continuously or in pulsed mode, are widely employed in various scenarios to generate THz radiation by optical pumping. Two continuous laser sources may be mixed and the mixed frequency lies in the THz range. The laser sources exploited include diode lasers, dual-mode lasers and multi-mode lasers. Photomixers are typically based on low-temperature grown GaAs. Difference frequency mixing occurs in a variety of materials. THz emission also occurs from continuous stimulation of microspheres by a single laser which produces mechanical resonance. Pulsed lasers are used to excite photoconductive switches or antennas. THz radiation also arises when a laser pulse pumps nothing more than air – the photoionization of the gas producing plasma. Other gases, including noble gases, may be used. The radiation is very broad in its frequency range. As a diagnostic method, gas photon-ionization allows the measurement of the carrier-envelope phase of short laser pulses. Solid targets may be used. The polarization may be coherently controlled, and is enhanced by electric fields. In ferromagnetic films, magnetic, rather than electric dipoles are employed. THz parametric oscillation in crystals can produce coherent, tunable and unidirectional radiation; efficient output coupling is critical in realizing high power. [2, 4-5]

1.1.2 THz applications

THz technology has been applied in many areas and used in a wide variety of applications, including information and communication technology, remote-sensing and communication, biology and medical sciences, non-destructive evaluation, quality control of food and agricultural products, and ultrafast computing. [3][6]

The THz part of the electromagnetic spectrum is rich in molecular rotational lines and fine structure lines of atoms or ions, which are useful for exploring the atmosphere in the space. For example, the ClI fine structure line is at 1.6 THz, the OH rotational transitions at 1.8 THz, 2.5 THz and 3.5 THz, and the OI fine structure line is at 4.7 THz. THz QCLs are more advantageous to be

used in local oscillators compared with traditional THz sources. Traditional sources, such as multiplied microwave, often deliver low power, and optically pumped gas lasers are relatively bulky and not tunable in frequency. [7]

In remote sensing, THz time domain spectroscopy (TDS) and frequency domain spectroscopy (FDS) are widely used. Moreover, intense femtosecond laser beams can be focused near objects and generate ambient plasma which produces THz waves, and the reflection from the target is detected in a similar way to THz-TDS. [6]

THz technology is also valuable in security applications. THz imaging has high imaging resolution since it combines macroscopic and microscopic imaging which allows the precise margin delineation. Therefore they can be used in identifying materials, security-related detection of weapons, drugs, and explosives. [6] A THz camera can image objects through fog and smoke, regardless of the background illumination. [2][6] THz imaging can also be used in biology and medicine, for example, cancer research, label-free DNA sensing, and non-destructive evaluation. [3] THz imaging was realized on systems based on picosecond THz pulses and continuous THz waves. THz pulse imaging provides broad imaging information between frequencies 0.1 and 5 THz. THz QCLs have been demonstrated with CW operation and mW output power level, so they provide a broader range of applications for imaging with CW THz radiation. [8]

In biological, medical and pharmaceutical sciences, intermolecular vibrations can be observed by THz spectroscopy in molecules where the intramolecular mode appears in the THz region. THz spectroscopy and imaging can also be used in the diagnosis of cancer, since the absorption of THz waves is sensitive to water and unusual reflections from cancer tissue due to the different hydration levels from normal tissue. [6]

In semiconductor and other industrial areas, applications include inspection of silicon solar cells, nano-composites, polymer films and dielectric films. THz TDS is also applied in the evaluation of semiconductor wafer properties, including mobility, conductivity, carrier density and plasma oscillations. THz imaging has been used as non-destructive evaluation to inspect the foam insulation used for the space shuttle. The sensitivity of THz waves to water could be used in monitoring food and agricultural products, for example evaluating the damage to fruits. A THz QCL can be a real-time THz-imaging tool for visualizing the doping level of ion-implanted silicon wafers. [6]

In the area of communication, THz technology is used in applications, such as wireless communication, high-speed data processing and satellite communication, communication in rural areas, communication between buildings during disasters, high-vision data delivery. The development of various basic circuits for THz information and communication technology is also progressing rapidly. [6]

1.2 THz QCLs

QCLs are unipolar emitters operating from the THz to the near-infrared range. The laser transitions take place within the conduction band in which the energy levels are quantized. The operation principle is inter-subband optical transitions in two-dimensional QWs of a semiconductor heterostructure. The challenge of THz QCLs is due to the lower energy of the photon than the energy of longitudinal optical (LO) phonon of the host material ($\hbar\omega_{LO} \approx 36 \text{ meV}$) for GaAs. Also, the free carrier absorption induces heavy waveguide losses for longer wavelength QCLs. [9]

1.2.1 Development of QCLs

Hetero-junction superlattices (SPLs) and their transport properties were first investigated by Esaki and Tsu in 1970. [10] The idea of using inter-subband transitions for electromagnetic wave (radiation) amplification was firstly proposed by Kazarinov and Suris in 1971 [11]. This inter-subband emission was observed in 1985 and the first sequential resonant tunnelling through a multi-quantum well SPL was reported in 1986 by Capasso et al. Such a structure has difficulty in practical use as a quantum cascade active region and is electrically unstable. [10] In 1994, Faist et al. demonstrated the first QCL based on inter-subband transition, designed to emit at $4.2 \mu\text{m}$ wavelength (75 THz) and grown by MBE, with a peak power at 8 mW. [12] QCL devices demonstrated in the following years covered the wavelengths from $3.5 \mu\text{m}$ to $24 \mu\text{m}$. Since then, mid-infrared QCLs have undergone rapid progress. The first operation at room temperature was shown in 1996 [13], the first distributed feedback (DFB) QCLs were reported in 1996, the first QCL based on GaAs/AlGaAs material system in 1998, the first operation in CW mode at room temperature in 2001 [13], and CW operation at 312 K in 2002 [10], and the first power exceeding 1 W in CW mode at room temperature in 2008 [14][15]. From the spectral standpoint, notable

milestones are the first DFB QCL in 1997 [16], the first broadly and continuously tunable external cavity QCL in 2004 [17].

With the rapid development of mid-infrared QCLs, researchers started to investigate whether QCLs could emit in the THz region. THz QCLs are essential for imaging applications and high-resolution spectroscopy techniques. [3] Nonlinear sources similar to photomixers have achieved more than 1 mW peak power in pulsed mode with room-temperature operation. [18] These sources have the advantage of wide tunability. Higher power in CW operation is one of the challenges. [18] THz QCLs based on inter-subband transitions in semiconductor SPLs have been demonstrated in different material systems, such as GaAs/AlGaAs, InGaAs/InAlAs, and InGaAs/GaAsSb.

The first step towards the accomplishment of THz QCLs emitting at frequencies below 8 THz was made in 1998 by Rochat et al. through the observation of THz (4.5 THz) electroluminescence from a quantum cascade structure, which triggered the investigation of several similar structures. [10] Since their initial demonstration, THz QCLs have made rapid and substantial progress. In 2001, the first THz QCL was reported operating at 4.1 THz in pulsed mode and with a maximum operating temperature of 65 K using the GaAs/AlGaAs materials system [19]. In 2002, 4.5 THz QCLs with the similar structure were demonstrated and this structure shows the first CW operation at THz frequencies by optimizing the processing technique. The first major improvement in THz QCL performance came with a bound-to-continuum (BTC) design with semi-insulating surface-plasmon (SISP) waveguide. THz QCLs based on $\text{In}_{0.52}\text{Al}_{0.48}\text{As}-\text{In}_{0.53}\text{Ga}_{0.47}\text{As}/\text{InP}$ material system was demonstrated in 2005. [10] The introduction of a design based on resonant optical phonon extraction, combined with the use of double metal (DM) waveguides, enabled a significant increase in the maximum operating temperature. The reported maximum temperature achieved by these devices was up to 200 K in pulsed mode [15][20]. Output power has also been improved by at least an order of magnitude. THz emission frequencies now range from 2.1 THz up to 4.8 THz and DFB THz QCL devices have been demonstrated to achieve single-mode operation of THz QCLs with narrow beam patterns. [21] Continuous frequency tuning in the range >300 GHz has also been established. [3] CW operation has been demonstrated above the technologically practicable temperature of liquid nitrogen for THz QCLs emitting at frequencies 1.5 THz~4 THz. [18]

THz QCLs can be used for other research and application purposes. For example, a THz optical amplifier based on a 2.9 THz QCL structure was demonstrated by depositing anti-reflective facet coating. [22] Dominic Bachmann et al. also demonstrated a broadband THz amplifier based on ultrafast gain switching in a QCL with a DM waveguide. An amplification bandwidth of more than 500 GHz was achieved due to the broadband THz gain. [23] Campa et al. demonstrated two different designs for resonant THz cavities based on wire-grid polarizers as input/output couplers, and injected by a CW QCLs emitting at 2.55 THz. [24] A new switching circuit for difference-intensity THz QCL imaging by amplitude modulation and lock-in detection has also been demonstrated and the stability for locking the amplitude modulation and detector output also improved. [25] The on-chip generation and detection of THz radiation in coupled cavity systems was demonstrated using a single semiconductor hetero-structure. Multiple sections of a THz QCL in a DM waveguide were optically coupled and operate either as a laser or an integrated emission monitor. [26]

Additionally, an active phase-nulling scheme for THz QCLs was realized by active electronic feedback control of the emission frequency under optical feedback. Real-time displacement sensing of targets was also demonstrated, overcoming the resolution limits. [27] QCL emission was also used for direct-absorption spectroscopy experiments, in order to study the dependence of the absorption coefficient on gas pressure and laser intensity. [28] A superconducting hot electron bolometer mixer and a QCL were integrated on the same 4-K stage of a single cryostat for the first time, reported by Miao et al. [29]

Many challenges, such as wide range tuning, lower emission frequencies and higher temperature operation have been investigated using a variety of approaches. [21] The main obstacle for THz QCLs to achieve room-temperature operation is the reduction of gain at higher temperatures because of the thermally activated relaxation mechanism between the upper and lower radiative states. [30] At high temperatures, electrons in the upper level will gain sufficient in-plane kinetic energy to emit an LO-phonon and relax to the lower level. Therefore, the upper level lifetime decreases with the increase of the electronic temperature, and consequently reduces the gain. [30] The maximum operating temperature of THz QCLs improves slowly with developments of material quality, active region and waveguide designs. [31] An additionally applied magnetic field can improve the operation temperature as well as operating at lower frequencies; however,

greater complexity during operation due to the magnetic field is required. [18] QCLs made of nanowire axial hetero-structures were proposed in 2014, suggesting that the lateral quantum confinement provided by the nanowires allows an increase of the maximum operation temperature and the reduction of the threshold current density. [32-33] QCLs with intra-cavity difference-frequency generation are currently the only room-temperature electrically pumped semiconductor sources that can operate in the range of 1-5 THz. [33] For electrical tuning, in 2015, the continuous electrical tuning of a single-mode THz QCL operating at a frequency of 3 THz is demonstrated, with a tuning range of 4 GHz and an optical output power of 0.7 mW. [34]

The emission properties of QCLs are determined by engineering the active region structures. The gain spectrum of a QCL depends on the design. There are two approaches [35]. One is the Fabry-Pérot laser. For this design, Fabry-Pérot cavities are formed by cleaving to allow emission. The advantage of these lasers is the broad spectrum, but it is difficult to output high power and the spectrum is unstable. DFB QCL is another option. It is similar to a Fabry-Pérot laser, but with a distributed Bragg reflector established on top of the waveguide in order to emit at the desired wavelength. DFB lasers can be tuned by 0.5% thermally, giving a well-defined wavelength [36]. The emission frequency of THz QCLs can now be adjusted in the range of 1-5 THz by choosing different layer thicknesses in the active region. [18]

1.2.2 Active regions

The active region designs of THz QCLs have developed rapidly in the past ten years. The three-quantum-well structure was used in the first QCL device with a diagonal transition [12]. Vertical transitions were demonstrated to improve the inter-subband gain [36]. A typical vertical transition design occurs in two coupled QWs, with a third very thin QW in the injection barrier to increase resonant tunnelling injection while preventing direct injection into the lower states.

New designs have been shown to improve the electron extraction from the active region. These include: CSL, BTC, resonant phonon (RP), and hybrid designs based on BTC and RP. The simulated band diagrams of each design are shown in Fig. 1.2 to Fig. 1.5. The curved conduction band energy levels are caused by the high injector doping level.

SPL based active region QCLs were first introduced in 1997. In this design, laser action takes place between minibands. Such lasers consist of a periodic stack of nanometre-thick layers of QWs and barriers. The period of this artificial crystal is typically much larger than the lattice constant of the bulk crystalline constituents. This superimposed crystal potential splits the conduction band (and the valence bands as well) into a series of narrow (typically, tens to a few hundreds of meV wide) mini-bands separated by the energy gaps in the strong-tunnel-coupling regime. For a given set of materials, mini-band and mini-gap widths can be engineered by suitable choice of the layer thicknesses [37].

The CSL design is based on the coupling of several QWs together in a SPL to create mini-bands of states when the appropriate electric field is applied. The upper and lower-state wave-functions extend (for THz lasers) over several coupled QWs. 'Chirping' the quantum well and barrier thickness restores the large dipole matrix element existing between the states at the edge of the minigap. [3] The main limitations in slope efficiency and maximum operating temperatures for these devices were attributed to a thermal backfilling of the lower miniband and a weak population inversion. [3] A typical band structure is shown in Fig. 1.2.

For the BTC design, the active region consists of SPLs with a diagonal transition between states. Electrons are injected in an isolated state created inside a minigap by a thin well adjacent to the injection barrier, while electron extraction occurs through a lower miniband. Both injection efficiency and lifetime are maximized by the diagonal transition, while the lower-state population is minimized by miniband transport.

Long-wavelength ($\lambda \approx 16 \mu\text{m}$), high performance QCLs based on this design concept, operating above room temperature, have already been demonstrated. This combination of long lifetime, injection efficiency of the upper state and extraction efficiency of the lower state is especially advantageous in THz QCLs where population inversion is difficult to achieve. [3] As is shown in Fig. 1.3, there is an energy gap formed in the minibands between two injector states. The advantage of the BTC QCL design is its large phase space for scattering out of upper and lower states. [38]

Another design is called the RP design (Fig. 1.4). For most early THz QCL active region designs, LO-phonon scattering was not used for the depopulation of the lower state. Depopulating the upper state would also occur since the subbands are very close. However, in the RP design, the tunnelling from lower state is quicker. [41]

Hybrid designs are based on both the RP and BTC schemes. They combine the BTC optical transition with the phonon-assisted depopulation. The advantage of the scattering-assisted hybrid design (Fig. 1.5) is that the current transport could be improved by increasing the overlap of electron wave-functions and LO phonon scattering, without being limited by resonant tunnelling. [42]

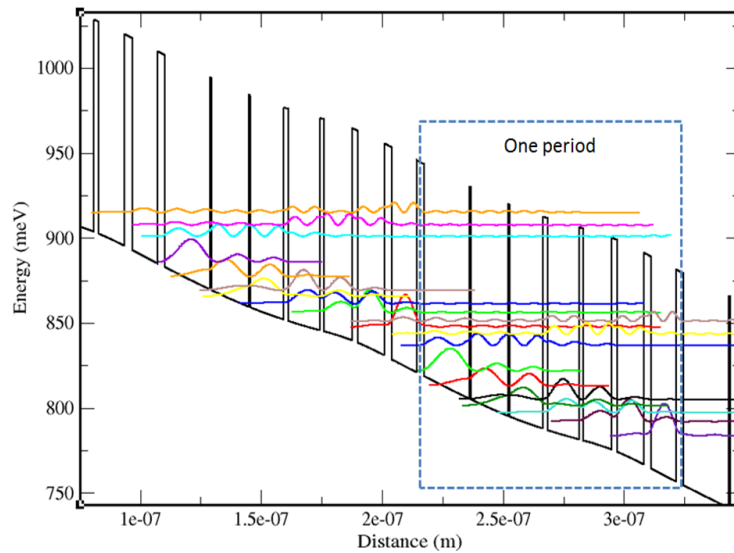


Figure 1.2 Conduction-band diagram and electron subband wave functions squared, calculated self-consistently using Schrödinger–Poisson solver [1] of a typical CSL QCL active region design.

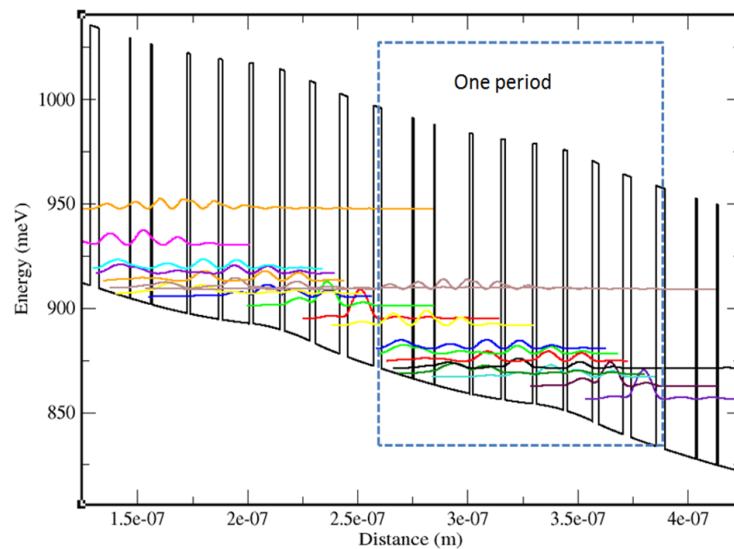


Figure 1.3 Conduction-band diagram and electron subband wave functions squared, calculated self-consistently using Schrödinger–Poisson solver [1] of a typical BTC QCL active region design.

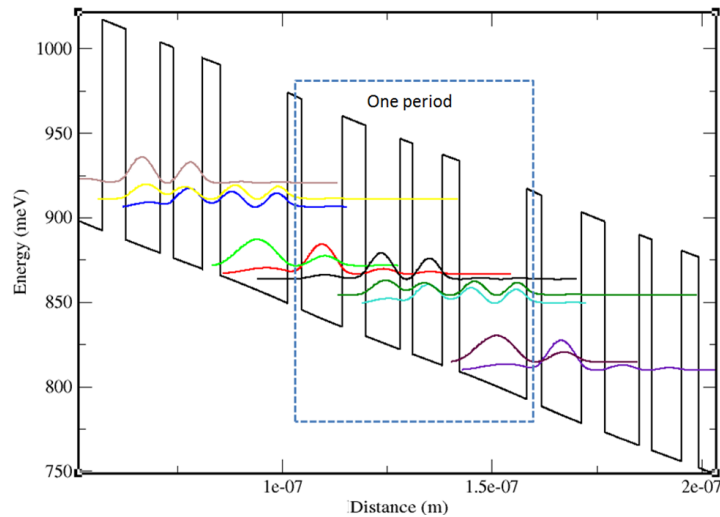


Figure 1.4 Conduction-band diagram and electron subband wave functions squared, calculated self-consistently using Schrödinger–Poisson solver [1] of a typical RP QCL active region design.

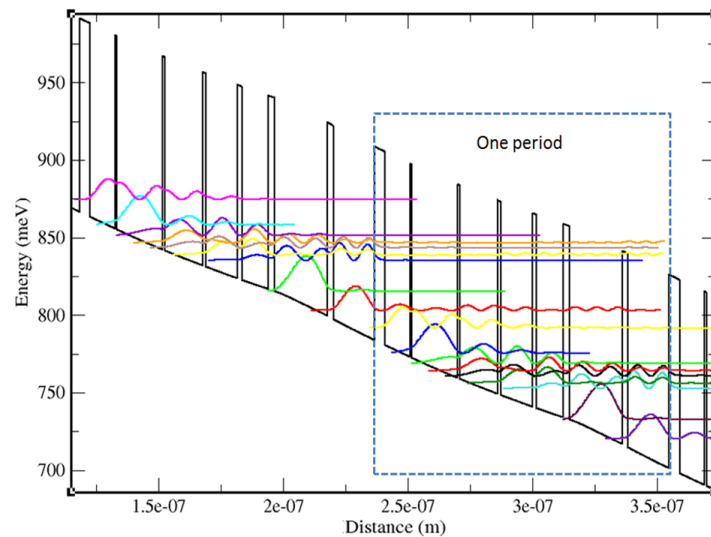


Figure 1.5 Conduction-band diagram and electron subband wave functions squared, calculated self-consistently using Schrödinger–Poisson solver [1] of a typical hybrid QCL active region design.

1.2.3 Material system for THz QCLs

Materials play a significant role in the device characteristics, by influencing barrier heights, scattering mechanisms, waveguide properties and so on.

QCL devices have been made by using four semiconductor material systems: InGaAs/InAlAs grown on InP substrates, GaAs/AlGaAs grown on GaAs substrates, AlSb/InAs grown on InAs, InGaAs/AlInAsSb, InGaAs/GaAsSb or InGaAs/AlInGaAs grown on InP substrates. [4]

InP/InGaAs/InAlAs and GaAs/AlGaAs material systems have been used most commonly for demonstrating QCLs. The remarkable aspect of these lasers is the wide spectral range of operation from a single material system. [43] High-performance mid-infrared QCLs are fabricated with the InP/InGaAs/InAlAs heterostructure system as a consequence of the large conduction band offset confining carriers in the QWs and minimizing carrier leakage into the energy continuum. [43] GaAs/AlGaAs mid-infrared QCLs were demonstrated by Sirtori et al. in 1998 [16][36]. They operate over wavelengths ranging from 8 μm to the THz wavelengths up to 160 μm . GaAs performs better than InP because of the material purity, which dramatically increases the mobility and the conductivity of the semiconductor at low temperature and guarantees lower waveguide losses. The first THz QCL based on GaAs was developed in 2001 by Köhler et al. Despite having a larger effective mass, smaller oscillator strength, and smaller gain coefficient, the THz material loss in GaAs-based heterostructures is significantly smaller compared to InP-based designs. [43] Other materials have been explored over the years. For the Si/SiGe materials system, intersubband transitions occur in the valence band, which is different from traditional materials. In addition, different hole-dispersions increase the number of subbands, which makes the control of their energy separation more difficult, and lasing has not been demonstrated.

1.3 Thesis outline

This thesis investigates the optimization on the THz QCL performances, by studying the MBE growth, fabrication and device characterisation. The performances of THz QCLs are enhanced, especially the output power. Four experimental chapters (Chapter 2, 4, 5 and 6) present the details on the MBE growth reproducibility and THz QCL device performance enhancement.

Chapter 1 is the general introduction of the development and application of THz technology. Different THz sources are reviewed and summarized. The QCLs are introduced by summarizing different active region designs, material systems, and the development in the past two decades.

Chapter 2 investigates the MBE growth of THz QCLs. The growth reproducibility is achieved by accurate control on growth rate, Si doping and so on. The procedure of MBE growth is introduced, including the flux, growth rate calibration and Silicon doping calibration.

Chapter 3 describes the fabrication and electrical characterisation of THz QCLs. Two primary waveguides of THz QCLs reviewed with their advantages and disadvantages are discussed. The approaches for fabricating both waveguide THz QCLs suggested, with detailed fabrication procedures given. Additionally, the electrical characterisation principle is summarized, and the experimental set-up introduced.

In Chapter 4, THz QCLs with the highest power so far at heat-sink temperature of 10 K are presented. The active region is described and the modification of this structure explained, with simulation and experimental results discussed. Different analysis are explained, including device performance on facet coating and output power dependence on device area.

Chapter 5 studies the optimization on BTC and hybrid THz QCLs, particularly for the structures with emission frequency at 3.1 THz and 3.5 THz. The simulation results being analysed. Injector doping and background impurity level influences on device performance are investigated and the optimization on three different THz QCL structures studied in terms of injector doping optimization.

Chapter 6 investigates GaAs misorientation angle influences on THz QCL device performance, with particular regard to the electrical performance, such as threshold current density. Research on misorientation is reviewed and the basis of misorientation explained. The results based on BTC and Hybrid THz QCL active region structure are presented. The conclusion suggests the influence of GaAs substrate misorientation angle on THz QCL device performance though not significantly.

Chapter 7 concludes the thesis. The work is summarized and possible future direction suggested. Problems encountered are also mentioned.

Chapter 2

Molecular beam epitaxy

2.1 Introduction

Molecular beam epitaxy (MBE) growth is a physical deposition method for growing thin epitaxial structures made of semiconductors, metals or insulators. MBE offers precise control of film thickness, composition and doping. The most important aspect of MBE is the slow deposition rate (less than 1000 nm per hour), which allows films to grow epitaxially. The slow deposition rates, however, require a proportionally better vacuum to achieve the same impurity levels as other deposition techniques.

This chapter outlines MBE growth, and introduces the necessary calibration methods by describing flux calibration, growth rate calibration and silicon doping calibration. Then, the MBE growth approach and the factors influencing the growth quality of THz QCLs are introduced.

2.2 MBE system

The VG-80H MBE system consists of three main chambers (see Fig. 2.1): a fast entry load lock (FEL), a preparation chamber and a deposition chamber. The FEL allows substrates to be loaded into and out of the system quickly, and degassed to 150 °C. The preparation chamber offers an outgassing stage for substrates, which can be heated up to 450 °C to remove N₂, CO, CO₂ and H₂O contaminants. Background-gas related impurities are thereby reduced to a minimum by reducing the density of background molecules. [44]

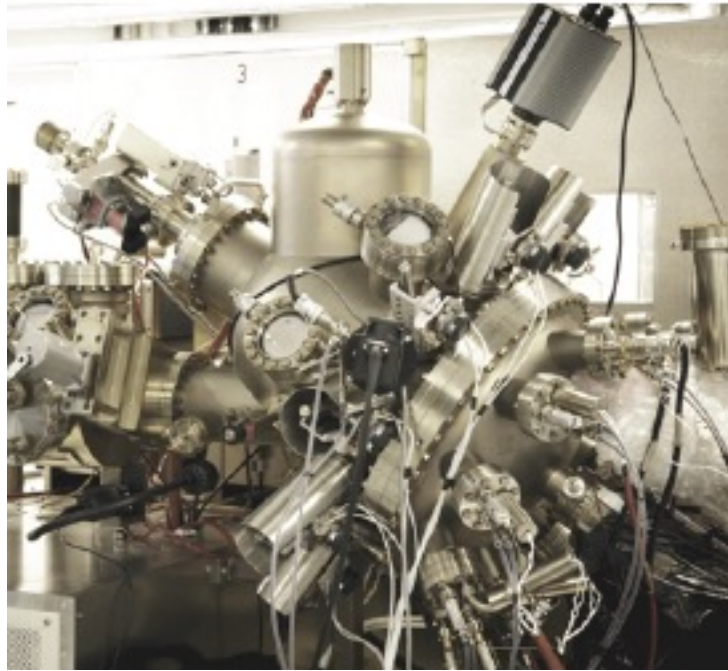


Figure 2.1 Part view of an MBE system illustrating the configuration of the major components.

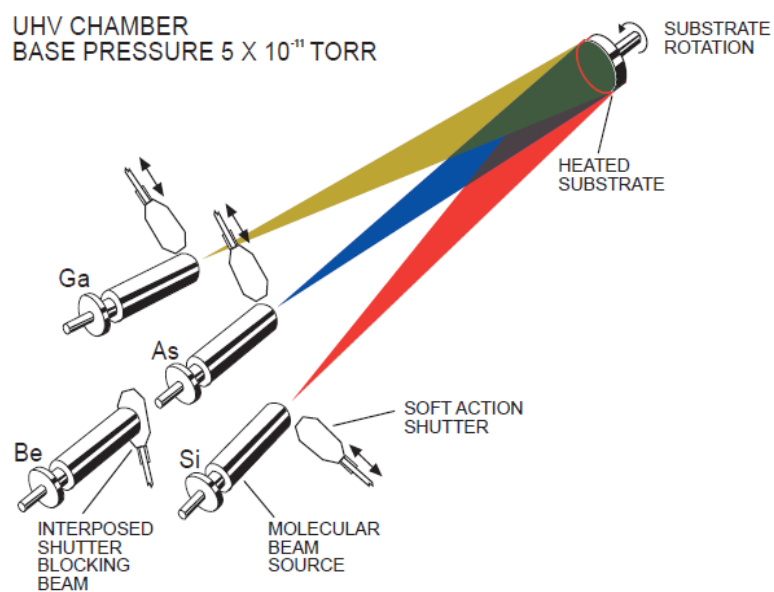


Figure 2.2 Principle of MBE. [2][45]

For the work described in this thesis, MBE growth takes place in the deposition chamber, where the background vacuum is better than 2×10^{-10} mbar. During layer growth, the deposition chamber pressure is between 1×10^{-8} to 1×10^{-6} mbar principally due to the group V species—arsenic in this case. The ultra-high vacuum environment within the growth chamber is

maintained by a cryopump, ion pump, titanium sublimation pump, and a liquid nitrogen cryopanel, which utilises cold nitrogen gas at a temperature close to $-160\text{ }^{\circ}\text{C}$.

Reflection high energy electron diffraction (RHEED) is used for monitoring the growth of the crystal layers. Shutters in front of each furnace allow precise control of the thickness of each layer (see Fig. 2.2). A quadrupole mass spectrometer (QMS) is used for monitoring the level of different residual gases in the chamber, and also for leak detection of the whole system using helium gas. For a full review of MBE growth, see [44].

2.3 Calibration

It is well-known that high-performance THz QCLs can only be obtained when the designed structure is strictly realized with the precise control of layer thickness and injector doping. This requires precise control of the layer thickness and alloy composition, which can be achieved by pre-growth calibration and post growth characterisation of the whole QCL structure by x-ray diffraction measurements [20, 46-53]. However, owing to the long growth time (10~15 hours) of a THz QCL, growth rate drifts occur over the whole THz QCL growth, as well as from run to run, affecting the control of layer thicknesses, alloy compositions. Therefore, it affects growth reproducibility. In order to demonstrate high performance devices, specific attention has to be paid to growth calibration [52].

2.3.1 Flux measurement

In solid-source MBE, elements such as gallium (Ga) and arsenic (As), in pure form, are heated in separate Knudsen effusion cells until they begin to evaporate. The gaseous elements condense on the wafer, where they may react with each other. In the example of Ga and As, single-crystal GaAs is formed. For each element, the flux needs to be calibrated, and beam equivalent pressure (BEP) measurements are normally used. Here, a monitor ion gauge (MIG) is used to measure the pressure from a particular cell at a set temperature, and the atomic/molecular flux can be obtained from the pressure reading. Fluxes from Ga, Al, and In cells can be modified by adjusting cell temperatures and then measured with the MIG. However, for an As cell, the flux is determined by the position of an As valve, with the source run at constant bulk and cracker zone temperatures. As shown in Fig.

2.3, for an As cell at a bulk zone temperature of 335 °C and a cracker set at 600 °C, the As flux increases linearly with the position of the As valve.

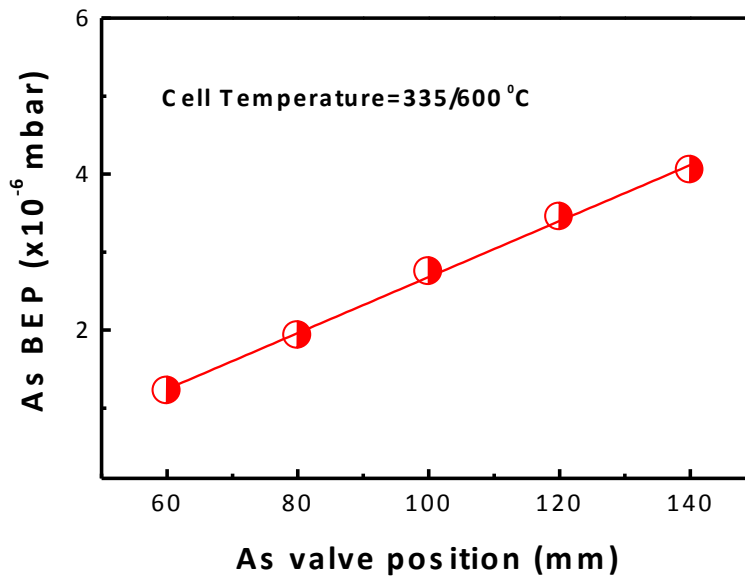


Figure 2.3 Measured As BEP at different valve positions.

2.3.2 Growth rate calibration

Most structures grown by MBE are composed of different compositional layers, so accurate thickness and composition control is required. Growth rates can be measured by x-ray diffraction, RHEED and pyrometry.

The pyrometry method provides both accuracy and efficiency for calibrating layer thicknesses and alloy compositions, and has principally been used for the work presented in this thesis. It also enables real-time growth rate monitoring [53-54], unlike techniques based on x-ray diffraction or RHEED. The technique also allows multiple, successive calibrations by analyzing pyrometric data acquired from the growth of a thick GaAs layer on AlAs, and vice-versa. In both cases, intensity oscillations result from interference effects in the semiconductor layer growth, as a function of time and wavelength.

As illustrated in Fig. 2.4, when different layers are grown on one substrate, the interfaces between the layers can be assumed to function as parallel reflecting mirrors. Incident light (e.g. from the substrate heater or an external light source) then travels through the etalon (θ_1) and undergoes internal reflection. Interferences occur between the light reflected by the two

surfaces. The thickness of the layer d_m can thus be obtained from interference fringes described by

$$n_2 d_m \cos(\theta_2) = m \frac{\lambda}{2} \quad (2.1)$$

With the growth rate determined by

$$G = \frac{d}{T} = \frac{d_{m+1} - d_m}{T} = \frac{1}{T} \frac{\lambda}{2n_2 \cos(\theta_2)} \quad (2.2)$$

Pyrometric intensity oscillations are determined by the wavelength and refractive indices of the different materials. The refractive index varies with the different materials. For an $\text{Al}_x\text{Ga}_{1-x}\text{As}$ layer, it is influenced by the AlAs mole fraction x , in $\text{Al}_x\text{Ga}_{1-x}\text{As}$, which can be obtained by Equation (2.3).

$$x = \frac{G(\text{AlAs})}{G(\text{AlAs}) + G(\text{GaAs})} \quad (2.3)$$

$$n = n_{\text{GaAs}}(\lambda) \times \eta(\text{Ga}) + n_{\text{AlAs}}(\lambda) \times x \times \eta(\text{Al}) \quad (2.4)$$

To measure the GaAs and AlAs growth rates, GaAs and AlAs films are grown on a (100) GaAs substrate. The pyrometric intensity oscillation is obtained by BandiT (Copyright 2002-2006, k-Space Associates, Inc) real time measurement. Fig. 2.5 shows the intensity oscillation image from GaAs and AlAs epilayers grown on a (100) GaAs substrate. Fig. 2.6 then shows a typical line profile, which is measured at the wavelength of 1220 nm.

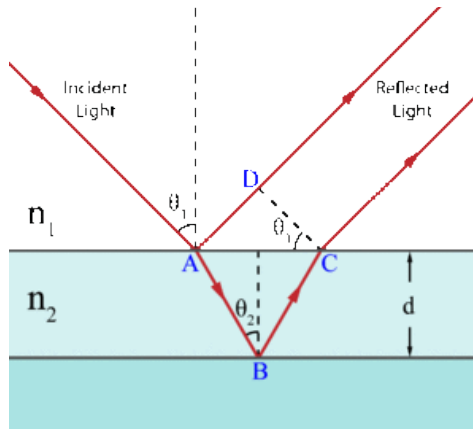


Figure 2.4 Schematic illustration of the mechanism responsible for pyrometric oscillations.

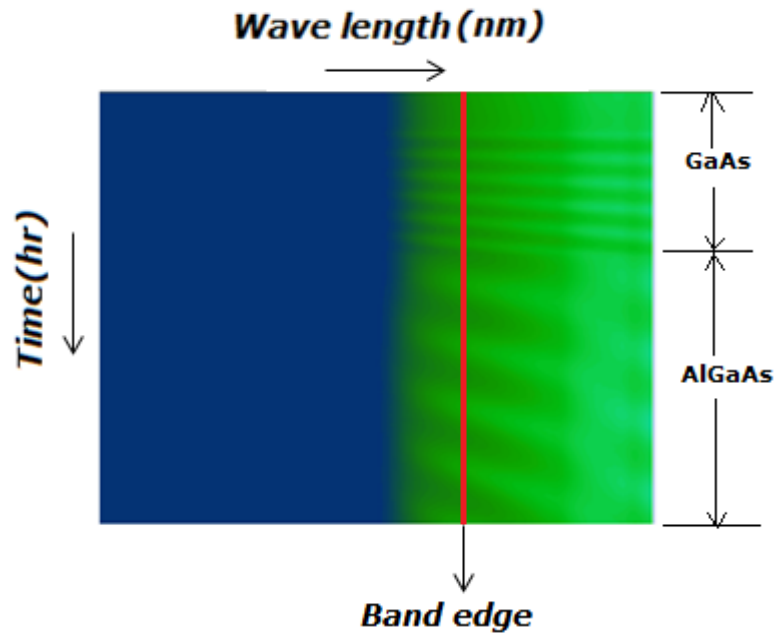


Figure 2.5 Pyrometric intensity oscillation for GaAs and AlGaAs layers, grown on top of an AlAs layer, itself deposited on a GaAs substrate. The Al cell temperature was=1184 °C, the Ga temperature 949 °C.

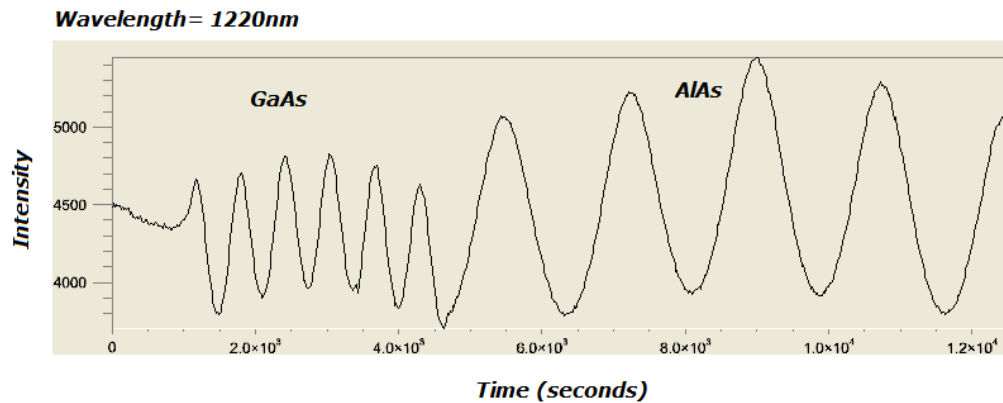


Figure 2.6 Line profile of pyrometric intensity oscillations for GaAs and AlAs at a wavelength of=1220 nm, extracted from Fig. 2.5, the AlAs growth rate was 0.42 μm/hr, the GaAs growth rate 0.968 μm/hr.

In Fig. 2.7, the growth rate calibrations of two Ga cells are shown as a function of cell temperature. An increase of growth rate has been observed as the Ga temperature is raised, due to increased evaporation at higher temperatures. As expected, the data fits to an Arrhenius equation, with the different behaviours reflecting the different cell designs.

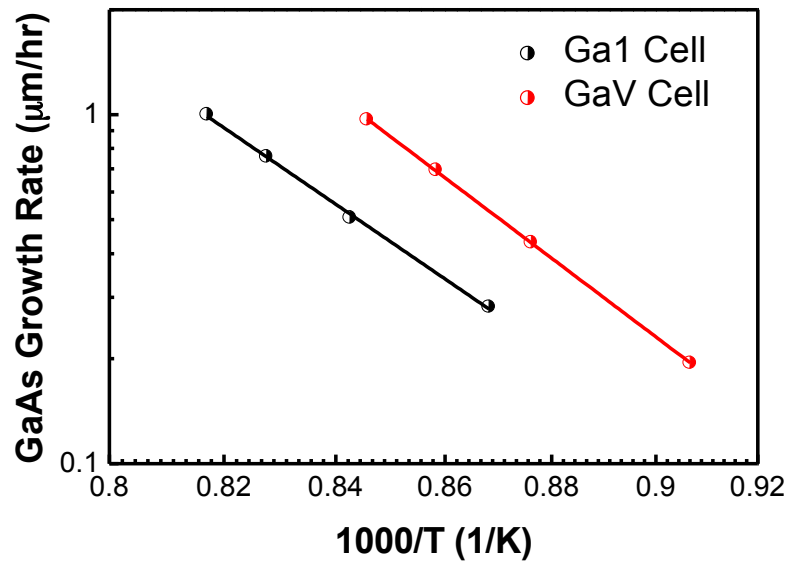


Figure 2.7 Dependence of GaAs growth rate on Ga cell temperature.

2.4 Si doping calibration

There are two principal ways to calibrate Si doping: Hall effect measurements, and secondary ion mass spectrometry (SIMS) measurements. Each has advantages and disadvantages. Hall measurements requires a relatively simple experimental set-up, and allow both the electrical carrier concentration and mobility to be measured. However, for low doping levels, thick layers are required to be grown in order to minimize depletion effects. SIMS can be used to measure different doping levels from a single device, which is more efficient than performing Hall measurements where a separate layer must be grown. Si doping can be measured by SIMS in GaAs down to doping levels lower than $1 \times 10^{16} \text{ cm}^{-3}$. SIMS thus combines high sensitivity with sufficient depth and spatial resolution to allow extensive characterisations of doping and compositional profiles of epitaxial semiconductors. [55] It cannot, however, give information on sample mobility, or on the electrical activation of the Si atoms.

2.4.1 Hall measurement

The Hall effect can be used to measure the charge polarity of carriers, the two-dimensional sheet charge density and the Hall carrier mobility. The free-carrier concentration is obtained from the sheet carrier density and the epilayer thickness. [56]

Mobility is one of the critical factors influencing device performance. A high value of carrier mobility in an epitaxial layer is widely accepted as a quality criterion, which means few scattering centres are present to limit the mobility. Mobility can be increased by limiting impurities from unintentional doping and improving any interface roughness. [56]

The Hall effect system consists of an electrically conducting material through which a uniform current density flows in a presence of a perpendicularly applied magnetic field. Due to the Lorentz force, charge carriers deflect to one side of the sample and generate an electric field perpendicular to both the current density and the applied magnetic field. Therefore, a potential drop is formed by the electrical charge called the Hall voltage (V_H) (see Fig. 2.8).

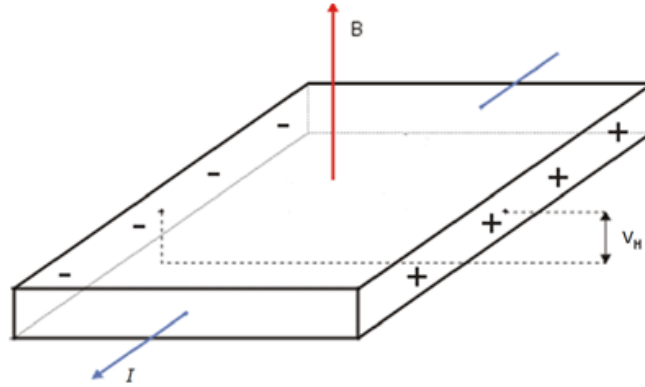


Figure 2.8 Schematic diagram of the Hall effect.

By measuring the Hall Voltage, the sheet density is obtained,

$$n_s = \frac{IB}{e|V_H|} \quad (2.5)$$

where I is the current, B is the magnetic field, and e (1.602×10^{-19} C) is the elementary charge.

In order to measure the resistivity of a semiconductor sample, a number of different device geometries can be envisaged. In our work, we have used a VDP geometry, owing to the simplicity of the fabrication where contacts are simply placed at the edge of a square/rectangular sample.

In order to then determine the sheet resistance (R_s), as shown in Equation (2.6). Since R_A and R_B can be obtained from the measured value of V_{43} , I_{12} , V_{14} , and I_{23} , R_s can be calculated by equation (2.6) (see Fig. 2.9).

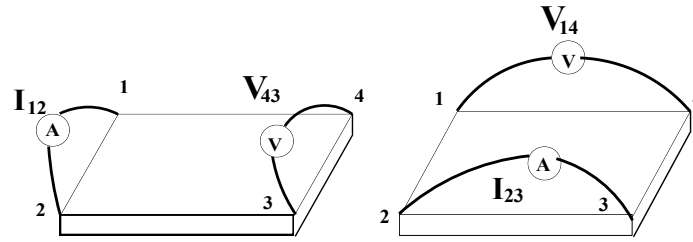


Figure 2.9 Schematic diagram of VDP Hall resistance measurements.

$$R_A = \frac{V_{43}}{I_{12}} \quad R_B = \frac{V_{14}}{I_{23}}$$

$$\exp\left(-\frac{\pi R_A}{R_S}\right) + \exp\left(-\frac{\pi R_B}{R_S}\right) = 1 \quad (2.6)$$

The Hall mobility can then be obtained from the equation

$$\mu = \frac{|V_H|}{R_S I_B} = \frac{1}{qn_s R_S} \quad (2.7)$$

If the conducting layer thickness d is known, the bulk resistivity ($\rho = R_S d$) and the bulk density ($n = n_s/d$) can also be calculated.

No.	Fabrication process	Van der Paw Sample geometries
1	Cleave sample to 3.5 x 3.5 square	
2	Form small Indium contacts in each corner of the square sample	
3	Heat sample on hot plate at 300°C for 1 hour	
4	Bond sample in chip pad	

Table 2.1 Sample geometry and fabrication for VDP Hall measurement.

To make VDP measurements, a square sample geometry is used, as outlined in Table 2.1. In order to obtain the most accurate results, contacts are required to be small and perfectly placed in the corners.

To set up the experimental VDP Hall measurement system, the measurement parameters used are shown in Table 2.2. Higher currents are used for highly doped samples owing to their lower resistances.

Equipment	Parameter
Magnetic field	700 Gauss
Constant-current source	from 10 μA to 100 mA (1 mA for Si-doped GaAs: 10^{16} - 10^{18} cm^{-3} , 10 μA ~200 μA for background doping of GaAs: 10^{13} - 10^{15} cm^{-3})
High input impedance voltmeter	1 μV ~ 1 V
Sample temperature-measuring probe	resolution of 0.1 $^{\circ}\text{C}$ for high accuracy work

Table 2.2 Required equipment of VDP Hall measurement.

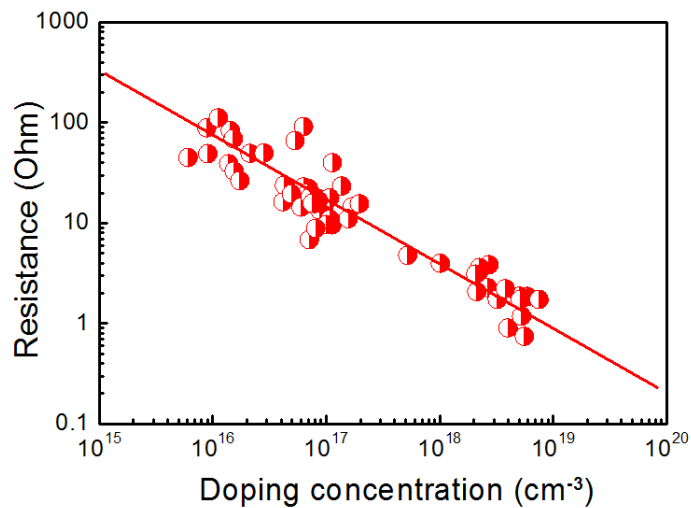


Figure 2.10 Resistance between two indium contacts as a function of doping density.

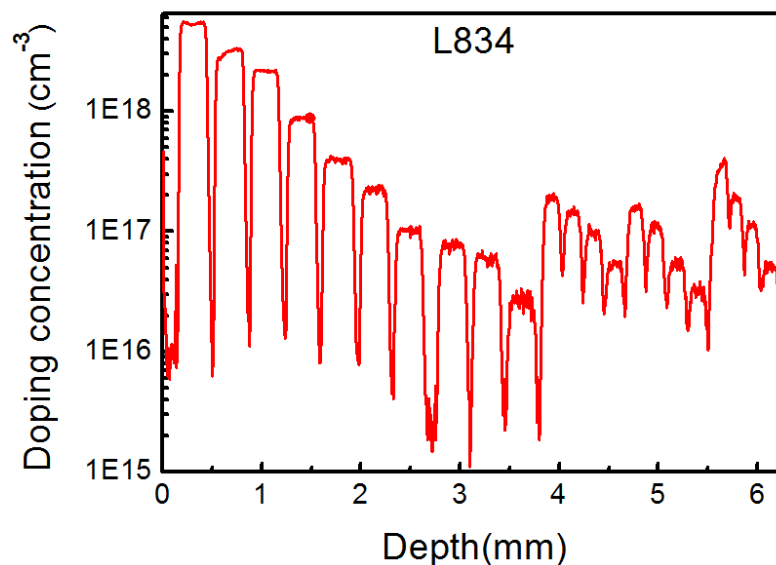
Fig. 2.10 shows data from a large number of samples in which the resistance between two indium contacts is measured. VDP data is compared with SIMS data in Fig. 2.13, and will be discussed later.

The resistance between two indium contacts decreases with the doping concentration, with an approximately linear relation, which provides a quick method for checking the doping of material.

2.4.2 SIMS calibration method

SIMS is based on the observation that charged particles (secondary ions) are ejected from a sample surface when bombarded by a primary beam of heavy particles. These secondary ions are accelerated into a double-focusing mass spectrometer where they are separated according to their energy and mass/charge ratio before being detected. The only sample preparation required is the production of a flat surface. Any vacuum compatible material can be analysed, including conductors (metals, alloys, and sulphides), non-conductors and biological material. [55] SIMS can thus be used in calibrating the silicon doping in MBE growth. By sequentially etching away the surface, a concentration as a function of depth can be obtained.

A typical structure designed for SIMS measurement has different layers, with varied Si doping concentration. The dopant concentrations at different depths from the surface of the sample are then measured by SIMS (see Fig. 2.11).



(a)

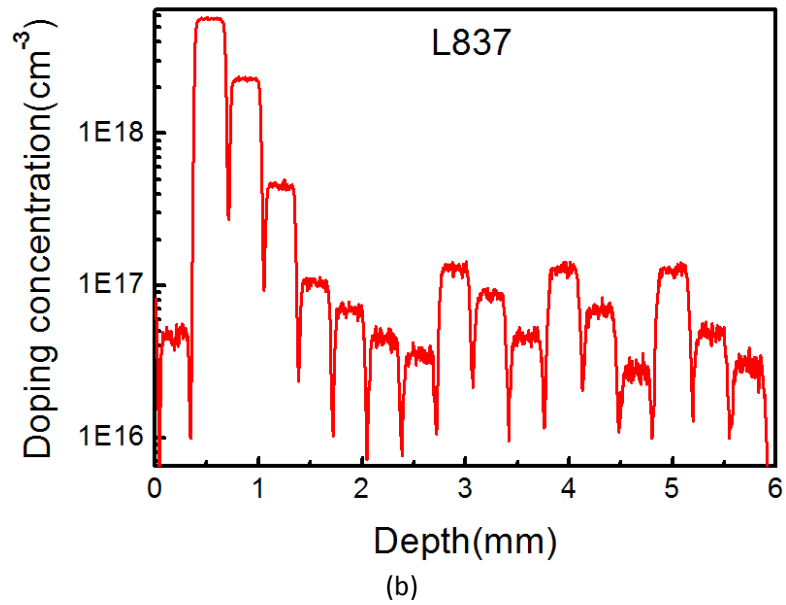
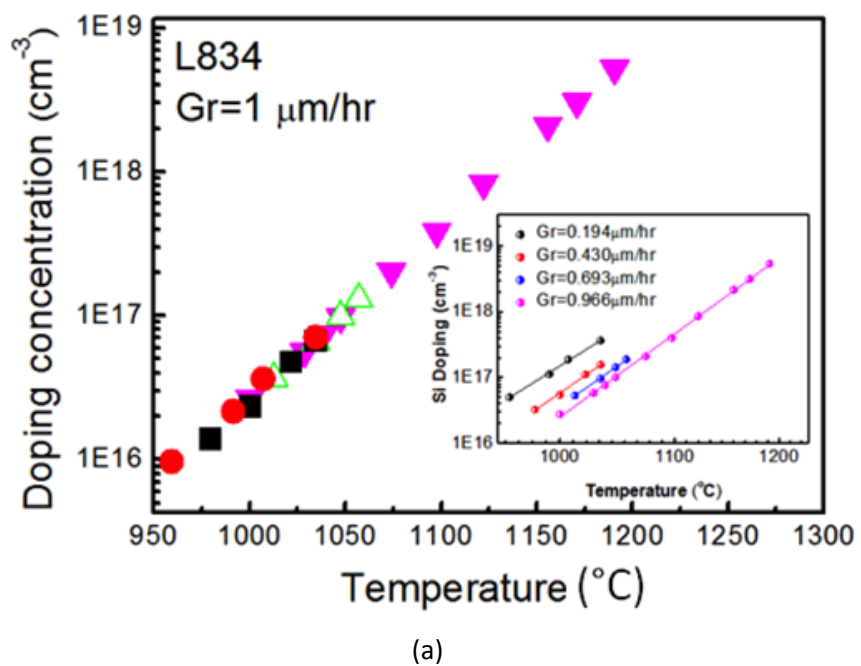
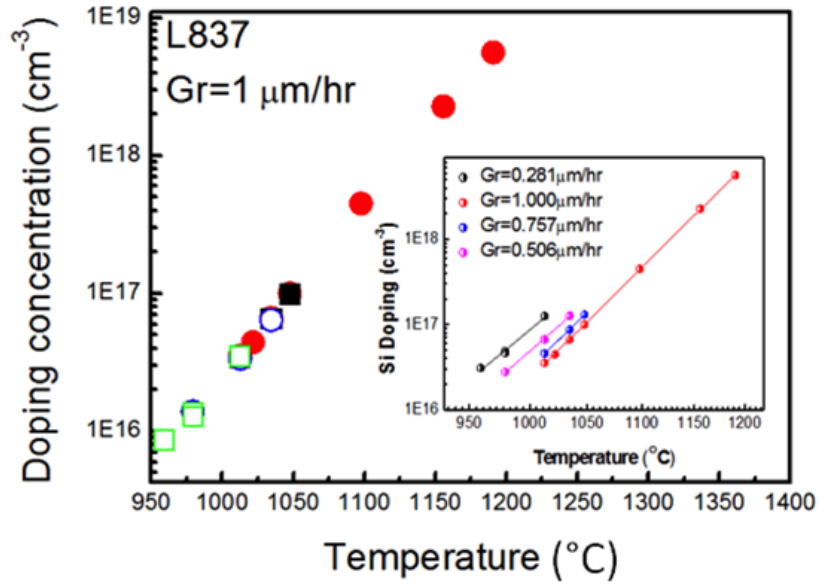


Figure 2.11 Doping concentration measured at different depths of a sample by SIMS, (a) L834, (b) L837.

In testing the SIMS approach to calibration, four different GaAs growth rates were used (see inset of Fig. 2.12, with the main figure showing data at a 1 $\mu\text{m/hr}$ growth rate). The average doping concentration was then calculated at each growth rate, showing a linear dependence on Si cell temperature (see Fig. 2.12) and confirming the reliability of the approach.





(b)

Figure 2.12 Inset: Doping concentration as a function of temperature for (a) L834, and (b) L837. Main figures show the doping concentration from all data, normalized to 1 μm/hour.

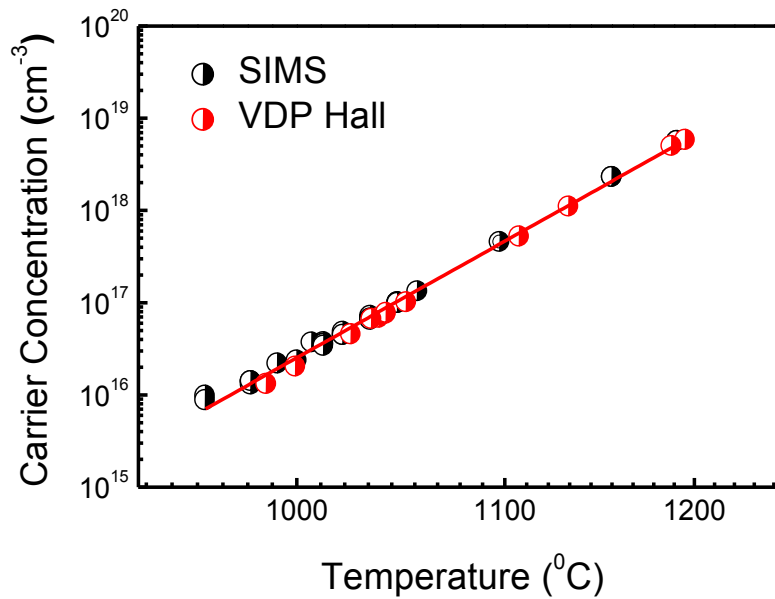


Figure 2.13 Carrier/doping concentration as a function of silicon cell temperature.

The SIMS result and VDP Hall measurement are compared in Fig. 2.13. A straight line is drawn fitting both SIMS and VDP Hall data, showing agreement between the two methods. The inset figures show the Si doping-temperature relation for different GaAs growth rate.

To calibrate the Si doping concentration, all growth rates can be normalized to 1 $\mu\text{m/hr}$. The normalized data can then be used for a calibration curve.

2.5 Growth of THz QCLs

THz QCLs are difficult to grow due to the thin layers in the device structures. Therefore the tiny variation of the layer thicknesses can induce the deviation from the original active region design. Thus, the precise control of MBE growth make it ideally suitable for THz QCL devices, and has been used for almost all structures reported in the literature, including all devices presented in this thesis.

2.5.1 Growth procedure

The quality of THz QCLs will be determined, amongst other things, by the growth rate stability, interface roughness, epitaxial defects and background doping levels. The growth rate stability affects homogeneity of all periods of the active region and hence the optical gain. The interface roughness, determined by atomic segregation, induces inhomogeneous broadening of the intersubband transition and consequently of the gain curve. Moreover, interface fluctuations create a scattering in-layer potential affecting elastic scattering of electrons in the QCL active regions, and thereby influencing the electron dynamics and the lifetime of electrons in excited states.

Normally, a QCL structure is grown on an undoped GaAs (100) oriented substrate. Growth begins with an undoped GaAs buffer layer, followed by an $\text{Al}_x\text{Ga}_{1-x}\text{As}$ etch-stop layer, and a high-doped GaAs layer. The active region then follows. Finally, a 50 nm GaAs layer with high doping is grown. [57]

During growth, the substrate temperature is monitored by a pyrometer. The aluminium (Al) and Ga flux is then kept constant during the entire growth and no growth interruptions between the layers of component materials are applied. Only the shutter in front of the Al effusion cell is activated and closed during the growth, with the Ga shutter open throughout. [58]

As is shown in Fig. 2.14, to grow a QCL structure, a few preparation steps are required. First, in order to minimize contamination, the new Si-GaAs substrate is required to be de-gased at 150 °C overnight in the FEL, to remove H_2O from the surface, followed by degasing at 450 °C until the pressure in the preparation chamber drops down to 1×10^{-9} mbar. Then, after

transferring the degassed substrate into the deposition chamber, the substrate is heated to 630 °C ~ 640 °C so that the oxide layer on the surface is removed. Meanwhile, the Ga and Al flux is measured and the As flux is measured and calibrated. This is followed with the growth rate calibration, by growing a 1 μm GaAs layer. The substrate rotation speed is set by monitoring the pyrometric oscillation output. Silicon doping accuracy should be guaranteed either by the VDP Hall method or by SIMS measurement. Once the QCL growth recipe starts running, the output of pyrometric oscillations by BandiT is used to monitor growth rate variation, followed by fine adjustment, and the As flux is adjusted according to the chamber pressure, at the stage of the GaAs buffer layer growth.

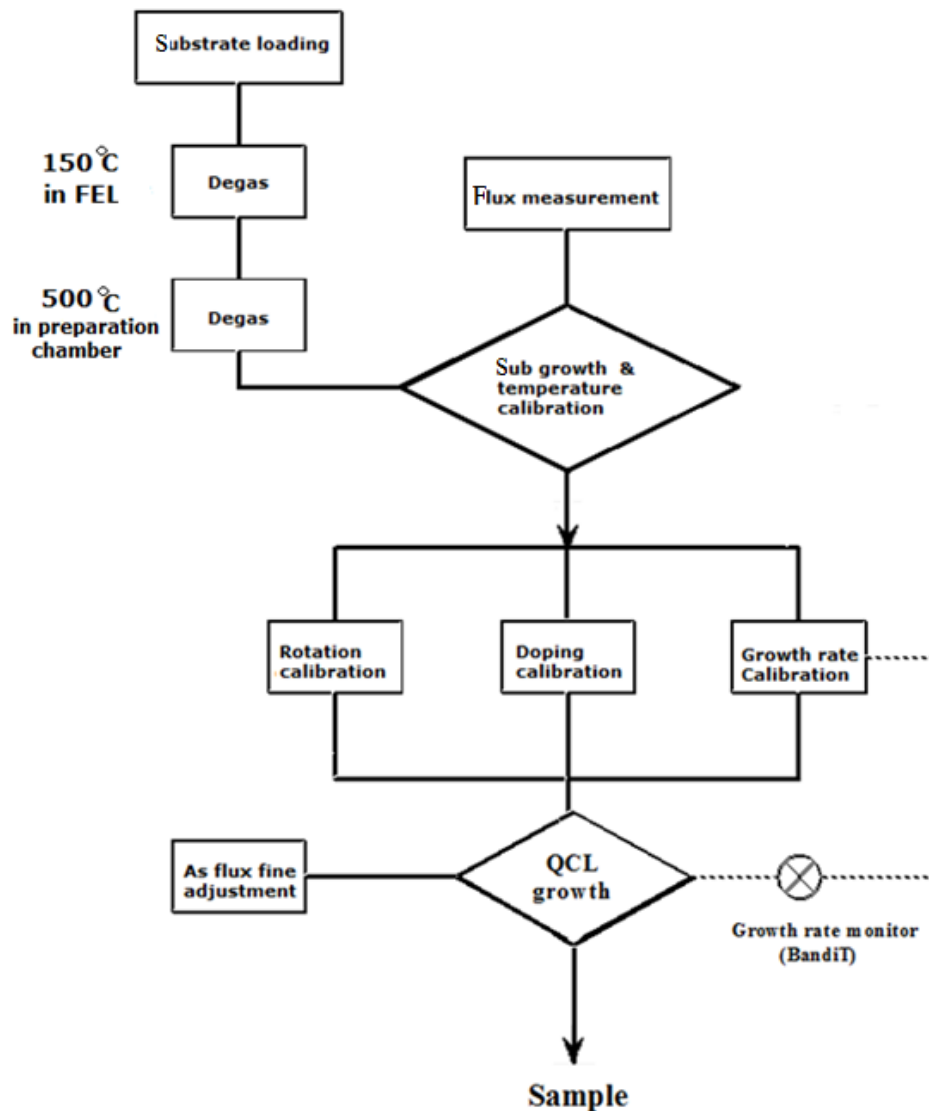


Figure 2.14 Flow chart of the QCL growth process.

The final output of pyrometric oscillation is crucial, which gives information about the average growth rate variation of AlGaAs and GaAs during the entire growth period.

2.5.2 Growth rate control of THz QCLs

To determine the growth rate during THz QCL growth, refractive index n is significant. However, there has been a lack of reported data on the refractive indices of GaAs and AlAs at the THz QCL growth temperature of ~ 600 °C, especially over the wavelength range of 1000-1400 nm. Pyrometric oscillations can provide an easy way for determining refractive index in THz QCLs.

To demonstrate, a set of samples were grown. Apart from the GaAs buffer and capping layers, The sample consists of a thick $\text{Al}_x\text{Ga}_{1-x}\text{As}$ layer, a 15 period $\text{Al}_x\text{Ga}_{1-x}\text{As}$ (~ 50 nm)/InAs (0.3 nm) SPL, and a thick $\text{Al}_x\text{Ga}_{1-x}\text{As}$ layer, with the mole fraction, x , changes in successive samples. The two separate thick $\text{Al}_x\text{Ga}_{1-x}\text{As}$ layers before and after the SPL, are used to acquire oscillation curves, as well as monitor growth rate drifts. The SPL is then used to determine precisely the $\text{Al}_x\text{Ga}_{1-x}\text{As}$ layer thickness using ex-situ techniques, such as x-ray diffraction or transmission electron microscopy measurements.

$\text{Al}_x\text{Ga}_{1-x}\text{As}$ (20 nm)/GaAs (6.5 nm) SPLs have been used to determine growth layer thicknesses using x-ray diffraction measurements [61]. However, by using this approach, strong deviations were observed between the expected and actual growth thicknesses, resulting from the uncertainty in determining the individual layer thicknesses [55]. In principle, the determination of individual layer thickness in the SPL by x-ray diffraction is achieved as follows: Firstly, the thickness of a single period of the SPL is deduced from the satellite peak separations of the diffraction curve. Then, individual layer thicknesses are determined by the average material alloy composition, deduced from the separation between the zero order satellite and substrate peaks. For $\text{Al}_x\text{Ga}_{1-x}\text{As}/\text{GaAs}$ SPLs, however, precise determination of the individual layer thicknesses is not straightforward, due to the difficulty in estimating the average Al composition [62]. In addition, the thin individual layer thickness in the $\text{Al}_x\text{Ga}_{1-x}\text{As}/\text{GaAs}$ SPL makes individual layers' growth more efficient. Flux transient, caused by shutter operations, can then influence the layer thickness [52]. The shorter the growth time, the more significant the effect, and it reduces the precision of the calibration procedure.

The issues associated with calibration using $\text{Al}_x\text{Ga}_{1-x}\text{As}/\text{GaAs}$ SPLs can be partly avoided by using $\text{Al}_x\text{Ga}_{1-x}\text{As}$ (~ 50 nm)/ InAs (0.3 nm) SPLs. The InAs layer is very thin, whilst the $\text{Al}_x\text{Ga}_{1-x}\text{As}$ layer is relatively thick. In fact, the InAs layer thicknesses in our calibrations are only about 5 ‰ of the total thickness of a single period. Therefore, when the single period thickness is determined by the satellite peak separation, it is dominated by the $\text{Al}_x\text{Ga}_{1-x}\text{As}$ layer thickness, reducing the uncertainty compared with estimating the average alloy composition of an $\text{Al}_x\text{Ga}_{1-x}\text{As}/\text{GaAs}$ SPL. This is a significant advantage. Furthermore, the thickness of the $\text{Al}_x\text{Ga}_{1-x}\text{As}$ layer is up to several tens of nm, thereby increasing the growth time and reducing the effects of flux transients. In our calibration samples, the $\text{Al}_x\text{Ga}_{1-x}\text{As}$ layers were grown at a temperature of ~ 600 °C, whilst the SPLs were grown at a temperature of 500 °C to avoid indium desorption. Very stable fluxes were used in order to minimize the effects of growth rate drift. All cell temperatures were kept constant through the entire growth of a single sample.

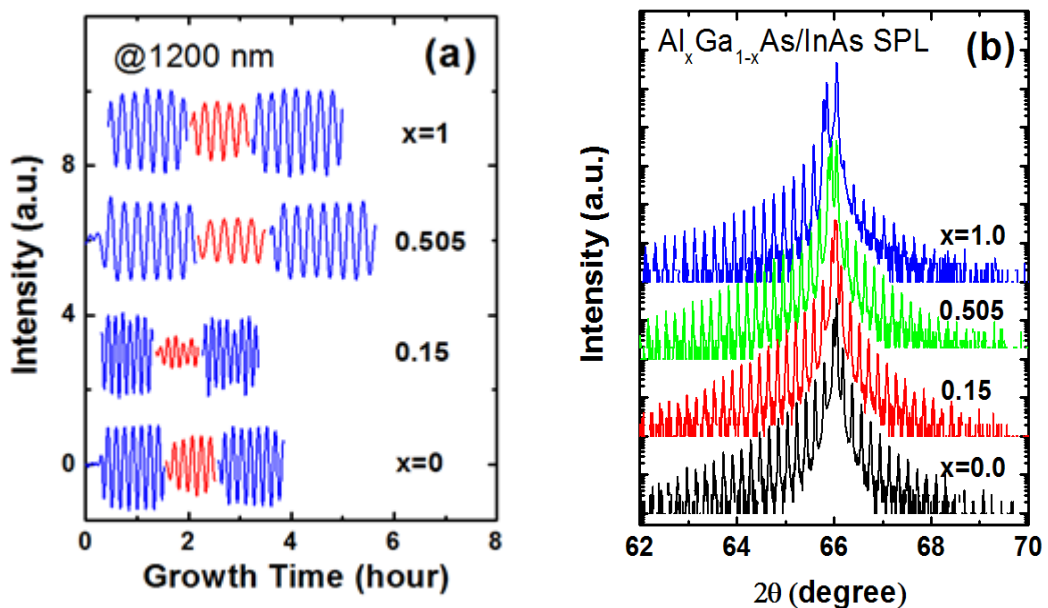


Figure 2.15 Experimental curves measured from calibration samples. Each curve is offset for clarity. (a) Typical oscillation curves at a wavelength of 1200 nm acquired by pyrometric spectrometer during growth. The blue curves originate from the growth of the thick $\text{Al}_x\text{Ga}_{1-x}\text{As}$ layers, whilst the red curves originate from the growth of the SPLs. (b) (004) x-ray diffraction curves taken after the sample growths.

Fig. 2.15 (a) shows the oscillation curves acquired at the wavelength of 1200 nm during the sample growths. The blue curves originate from the growth of

the $\text{Al}_x\text{Ga}_{1-x}\text{As}$ layers, whilst the red curves originate from the growth of the SPLs. From these curves, growth time T for each growth can be easily extracted. Fig. 2.15 (b) shows the (004) x-ray diffraction curves taken after these sample growths. Owing to the high structural quality, more than 30 well-defined satellite peaks are observed. From the peak separations, the $\text{Al}_x\text{Ga}_{1-x}\text{As}$ layer thicknesses in the SPLs were extracted with high precision. The growth rates were then calculated allowing n to be obtained at different wavelength by using values of T extracted from oscillation curves.

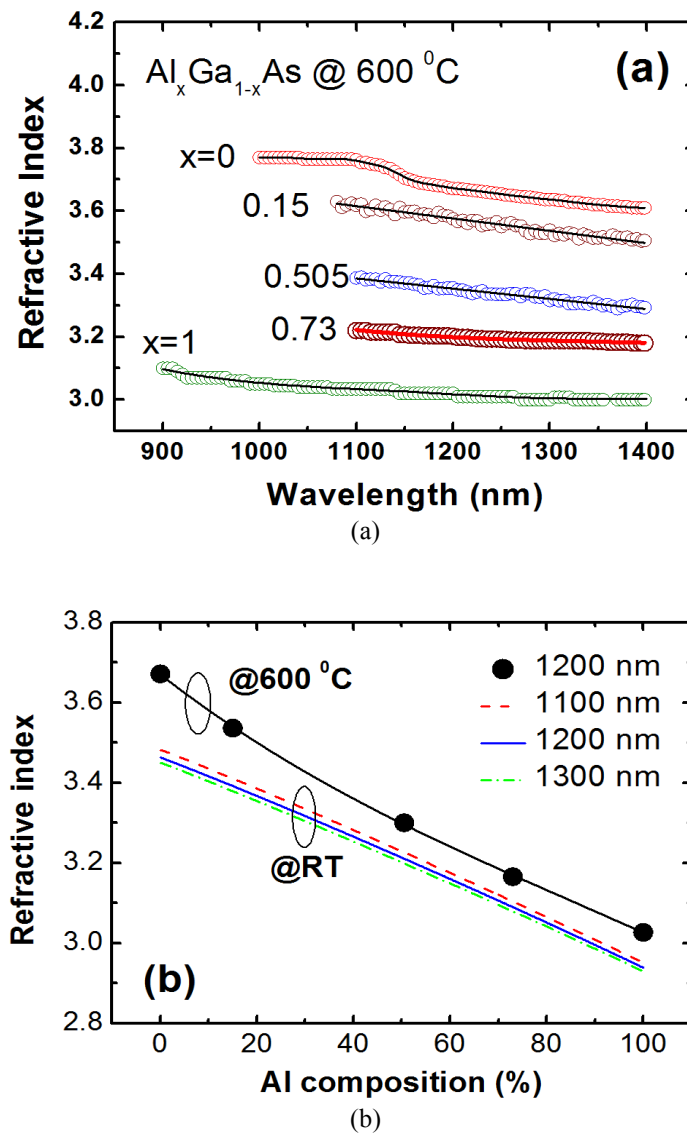


Figure 2.16 $\text{Al}_x\text{Ga}_{1-x}\text{As}$ refractive indices at a growth temperature of 600°C . (a) The refractive index as a function of wavelength for different Al mole fractions, and (b) the dependence of the refractive index on the Al composition. Solid black circles and line are experimental data and the least fitting curve respectively, obtained at the growth temperature of 600°C . The coloured curves are theoretical calculations according to [57].

The refractive indices, obtained from experiments at a growth temperature of 600 °C are summarized in Fig. 2.16. In Fig. 2.16 (a), n is plotted as a function of wavelength in the range of 900 to 1400 nm. n decreases with increasing wavelength. This follows the trend observed in the short wavelength range from 400 nm to 1000 nm in previous studies [63][64], with the refractive index values for GaAs and AlAs matching below 1000 nm. At ~ 1000 nm, n is ~ 3.78 and ~3.05 for GaAs and AlAs. To confirm the validity of the calibration approach, the values of n for GaAs and AlAs have been checked in multiple growths, which shows a high degree of reproducibility. In Fig. 2.16 (b), the dependence of n on Al composition is presented. Unlike the theoretically calculated curves at room temperature [65], there is a small deviation of the curve away from a strict linear correlation, similar to the observation in [59]. The refractive index curves in Fig. 2.16 are used for daily pre-growth calibration for THz QCLs, and the monitoring of THz QCL growth in our laboratory. The effect of temperature variation on n is very small [59][60]. Therefore, this set of data can be used over a wide growth temperature range. Over a temperature interval of 600 ± 40 °C, no significant errors were observed during the growth rate calibrations.

2.5.3 Layer thickness control and growth reproducibility

The growth rate drift, due to the consumption of the group III materials (Ga and Al), is important for the growth of high performance THz QCLs [52]. Although lasing action can still be achieved while the structural dimensions of a THz QCL vary from one period to the next, the overall performance is compromised [66]. This is only acceptable when maximum operating temperature or output power are not considered to be the most important performance requirements. However, for most applications, both high operating temperature and high output powers will be necessary. Therefore, the uniformity of the laser stack (or overall periodicity) is a high priority, demanding precise control of the material growth rates over the whole QCL growth period.

Based on the daily pre-growth calibration data recorded over a typical growth, the dependence of the required cell temperature to achieve a 1 $\mu\text{m}/\text{hour}$ growth rate for GaAs is plotted in Fig. 2.17, as a function of the total deposited GaAs layer thickness. As the total growth thickness increases, the gallium cell temperature needs to be increased to maintain a constant growth rate. This observation is very similar to that reported in [52] but with a significantly higher ramp rate, possibly due to cell differences. A Veeco

gallium SUMO cell was used in [52], while a dual-filament Ga cell was used in our MBE system. Unlike the variation observed in the gallium cell data, the aluminium cell temperature remains nearly constant over the whole growth run, even though there are slight temperature fluctuations. Our MBE system is equipped with two Al cells. One is only used for the growth of the THz QCLs. Al forms only less than 4% of the total deposited material in a THz QCL.

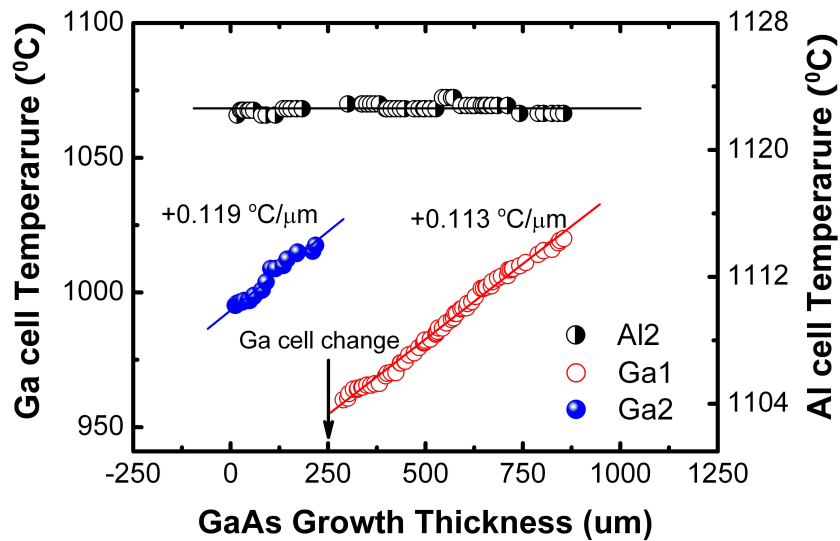


Figure 2.17 Typical variation of the gallium cell temperature required to achieve a 1 $\mu\text{m}/\text{hour}$ GaAs growth rate as a function of the total thickness of deposited GaAs during a growth run. Each data point corresponds to a single wafer growth. The aluminium data reflects the cell temperature required to achieve a constant growth rate of 0.176 $\mu\text{m}/\text{hr}$, as used for the majority of THz QCL growths. The aluminium data points thus correspond to THz QCL growths during the run – other device structures require different aluminium mole fractions.

Structure and growth parameters of typical THz QCLs reported in the literature are presented in Table 2.3. Thus, the Al is depleted by only a small amount during the limited number of THz QCLs (<70) realized during a growth run. Based on these observations, to ensure precise growth control of individual layer thicknesses/alloy compositions in THz QCLs, it is necessary to compensate for GaAs growth rate drifts, but variations in AIAs growth rate can be neglected.

QCL structure	G_{Ga} ($\mu\text{m/hr}$)	G_{Al} ($\mu\text{m/hr}$)	x_{Al} (%)	x_{QCL} (%)	G_{QCL} ($\mu\text{m/hr}$)
Worrall et al. 2006 [67]	1.00	0.111	10	1.75	1.018
Köhler et al. 2002 [68]	1.0	0.176	15	2.48	1.025
Fatholouloumi et al. 2012 [20]	1.00	0.176	15	3.70	1.038
Amanti et al. 2009 [47]	1.00	0.176	15	3.49	1.036
Kumar et al. 2011 [69]	1.00	0.176	15	3.81	1.040
Vitiello et al. 2007 [70]	1.00	0.176	15	2.15	1.022
Schrottke et al. 2013 [48]	0.75	0.25	25	3.18	0.775

Table 2.3 Structure and growth parameters of typical THz QCLs reported in the literature.

Despite theoretically-calculated and experimentally demonstrated growth rate drifts during wafer growth, an exact drift rate over a given time period is hard to predict, so precise growth rate uniformity is difficult to achieve. Pyrometric data, gives extensive information about the precision of the wafer growth, not only acting as an additional calibration approach during the growth of the QCL itself, but also providing information on growth rate drift during a structure's growth. For THz QCL structures, the GaAs growth rate drift can be indirectly extracted from pyrometric oscillations during THz QCL growth:

$$x_{Al} = \frac{G_{Al}}{G_{Ga} + G_{Al}} \quad (2.8)$$

$$x_{QCL} = \frac{d_{AlGaAs} \cdot x_{Al}}{d_{GaAs} + d_{AlGaAs}} \quad (2.9)$$

$$t_{GaAs} = \frac{d_{GaAs}}{G_{Ga}} \quad (2.10)$$

$$t_{AlGaAs} = \frac{d_{AlGaAs}}{G_{Ga} + G_{Al}} \quad (2.11)$$

$$G_{QCL} = \frac{d_{GaAs} + d_{AlGaAs}}{t_{GaAs} + t_{AlGaAs}} \quad (2.12)$$

G_{Ga} and G_{Al} are the GaAs and AlAs growth rate; x_{Al} is the aluminium mole fraction in the barrier; x_{QCL} is the average aluminium composition of the QCL; d_{GaAs} and d_{AlGaAs} are the total thicknesses of the GaAs wells and AlGaAs barriers in a single period of the QCL active region; t_{GaAs} and t_{AlGaAs} are the growth time of the GaAs wells and AlGaAs barriers; and, G_{QCL} is the average growth rate of the QCL, which can be written as:

$$G_{QCL} = \frac{G_{Ga}}{1-x_{QCL}} \quad (2.13)$$

The main structural and growth parameters of typical THz QCLs are listed in Table 2.3. In each case, x_{QCL} depends only weakly on G_{Ga} . For the QCL in [20], suppose the growth rate of GaAs drifts by +5%, this reduces x_{Al} from 15% to 14.4 %, but only reduces x_{QCL} from 3.70% to 3.58%. The resulting deviation of G_{QCL} is only about 1.3‰, leading to the conclusion that G_{QCL} is dominated by the changes in G_{Ga} . For a given THz QCL design, once G_{QCL} is known, G_{Ga} , as well as its growth rate drift, can be obtained. Growth rate compensation can then be realized more precisely, either during the growth itself or subsequent growths. Fig. 2.18 shows the pyrometric oscillation curve of a THz QCL structure in which growth rate compensation has been applied. Theoretical simulation, using a transfer matrix method [63][71], corresponds well with the experimental oscillation curve. Growth rate drift is negligible in Fig. 2.18, showing excellent control of the growth layer thickness.

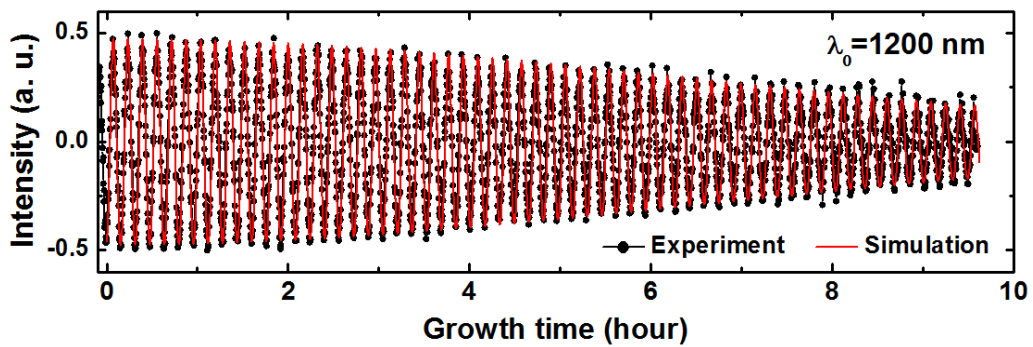


Figure 2.18 Typical pyrometric oscillations recorded during growth of a THz QCL structure using growth rate compensation. Theoretical simulation assumed a constant G_{QCL} of 1.036 $\mu\text{m/hr}$.

The growth rate compensation technique, together with the pre-growth calibration of GaAs and AlAs performed immediately prior to the QCL growth, enables high run-to-run growth reproducibility. Typical (004) x-ray diffraction

curves taken from two QCLs with nominally identical structures (based on [47]), but grown at different times, are shown in Fig. 2.19. Excepting the discrepancy of the satellite peak intensity at the extremes, both curves look almost identical. From the satellite peak separation, the actual single period thicknesses of the two QCLs are 65.4 and 64.8 nm, only ~ 0.2 and ~ 0.8 nm less than the designed value of 65.6 nm; this corresponds to $\sim -0.3\%$ and $\sim -1.22\%$ thickness deviation. It is worth noting that ~ 10 different THz QCLs were grown between these two samples. The thickness variation from the two QCLs in Fig. 2.19 is far less than the thickness variations of $\sim \pm 3\text{-}5\%$ generally reported using x-ray diffraction to calibrate the growth [46-48]. This confirms that pyrometric spectrometry is a powerful technique for achieving reproducible growth of THz QCLs, and enables run-to-run growth repeatability.

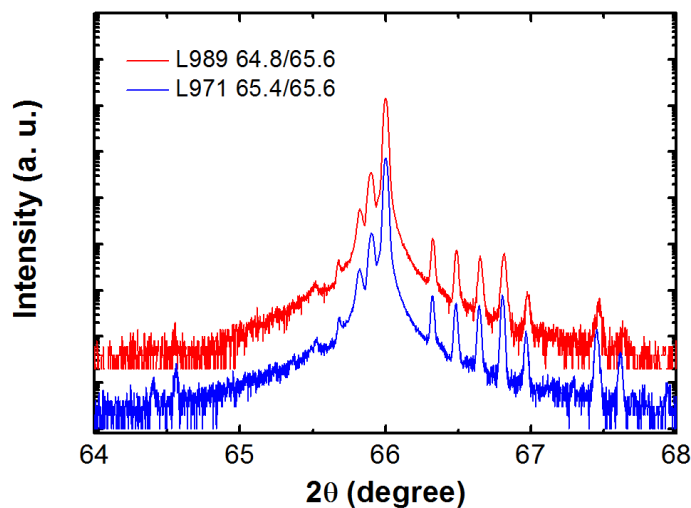


Figure 2.19 Typical (004) x-ray diffraction curves taken from two THz QCLs with nominally identical structure but grown at different times. The active region is based on the design reported in [5]. The layer sequence of one period of the structure is **55**/110/**18**/115/**38**/94/**42**/184 (starting from the injector barrier) where the thicknesses are in Å, and $\text{Al}_{0.15}\text{Ga}_{0.85}\text{As}$ layers are in bold type, GaAs layers are in regular, and the underlined layer is doped with Si.

2.6 Summary

Precise growth control is essential for achieving high quality THz QCLs. Pre-calibration on layer growth rate, material flux and Si doping are introduced in this chapter. Pyrometric spectrometry has been used in our material growth

providing high level of precision during growth rate calibration, and is proved to be a powerful tool for layer thickness and growth reproducibility control according to experimental analysis. The THz QCL wafers grown have achieved good performance and the results published in [72-82].

Chapter 3

Fabrication and electrical characterisation of THz QCLs

3.1 Waveguides of THz QCLs

The emission of a laser requires the gain medium to be confined inside a waveguide. Waveguides are used to confine emitted photons within the laser gain medium. Furthermore, mirrors at the waveguide terminals are used to reflect the photons back into the cavity. There are two fundamental waveguide designs for QCL devices, the SISP waveguide and DM waveguide.

An SISP waveguide is shown in Fig. 3.1 (a). The surface-plasmon mode is confined to the top metal contact and the bottom heavily doped GaAs layer used for the layer contact. [83] The mode confinement is determined by the refractive index contrast between the GaAs/AlGaAs layer and the GaAs substrate. In this waveguide design, the optical mode penetrates from the QCL hetero-structure into the Si-GaAs substrate. [84]

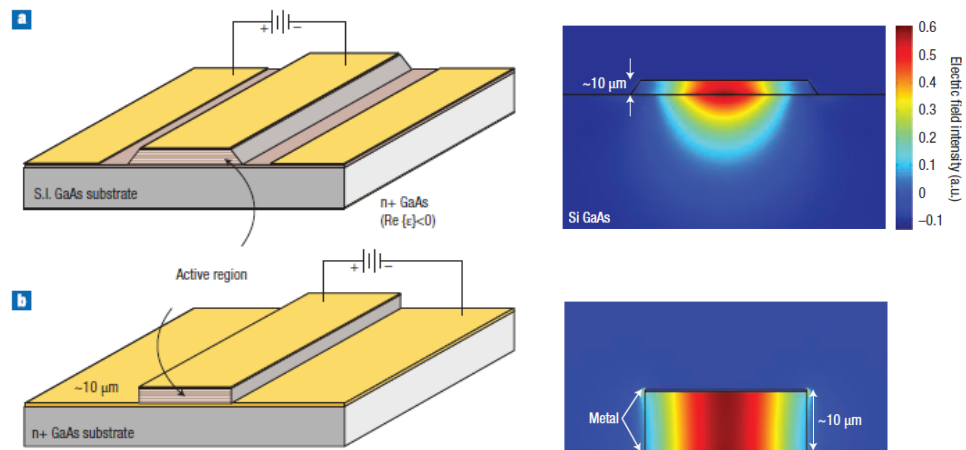


Figure 3.1 Schematic view of two QCL waveguides (left) and typical two-dimensional mode intensity pattern (right), (a) SISP waveguide, (b) DM waveguide. Taken from Ref. [83].

The second waveguide design is called the double metal waveguide (DM waveguide), which has been reported to exhibit better maximum operating temperature. In this design, the active region is sandwiched between two metal layers so that the optical mode is strongly confined within the active

medium, as is shown in Fig. 3.1(b). Both waveguide designs have their own advantages and disadvantages, whilst the SISP waveguide has high output power and better beam direction, the DM waveguides have better thermal performance. [83]

3.2 Fabrication of THz QCLs

The fabrication of THz QCLs includes both front side processing and substrate side processing. The essential steps include photolithography, mesa etching and metallisation.

THz QCL ridges with SISP waveguide are fabricated by a combination of photolithography using positive photoresist S1813, wet etching and metal evaporation techniques. The typical active region thickness is around 10 μm . Both the bottom and the top ohmic contacts are defined by photolithography followed by a premix alloy of AuGeNi evaporation and annealing. The ratio of Au:Ge:Ni is 86~94 wt%:3~7 wt%:3~7 wt%. The overlayer metallisation is to improve electrical contact, confine the optical mode and help dissipate excessive heating during lasing. For the fabrication of DM waveguide THz QCLs, Au based thermo-compression wafer bonding is used to bind a highly doped GaAs substrate with the THz QCL wafer. Before the wafer bonding, the THz QCL wafer is prepared by evaporating Ti/Au layers (20/600 nm) on the epilayer side. An n^+ GaAs receptor substrate is coated with Ti/Au (20/600 nm). [85] Following the wafer bonding, the SI GaAs substrate in the THz QCL wafer is chemically removed for 80% of the substrate using $\text{H}_2\text{SO}_4:\text{H}_2\text{O}_2:\text{H}_2\text{O}=1:8:1$ etchant and citric acid for the rest. The selective etch stops at $\text{Al}_{0.5}\text{Ga}_{0.5}\text{As}$ layer, which is then removed by 50% HF acid. The rest of the 600~700 nm n^+ GaAs material is subsequently removed by $\text{H}_2\text{SO}_4:\text{H}_2\text{O}_2:\text{H}_2\text{O}=1:8:160$. Similar to the THz QCLs with SISP waveguide, laser ridges are defined by photolithography and wet-chemical etching. Thin films of Ti/Au with thickness of 20/200 nm are evaporated by an electron-beam evaporator and followed by a lift-off process. [85] The aim of substrate thinning is to achieve good thermal dissipation to reduce extra heating during device operation, and the backside metallisation improves the adhesion of the indium mounting during device packaging.

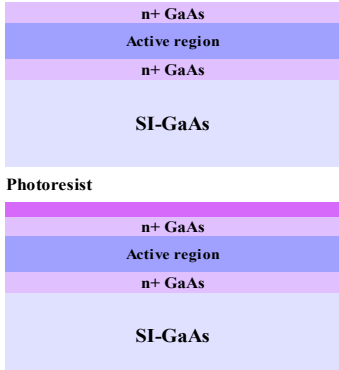

Parallel mirror facets are obtained by cleaving the laser ridges, which creates a Fabry-Pérot resonator. The mounting of QCLs plays an important role in their heat dissipation. The conduction path of heat flux from the laser

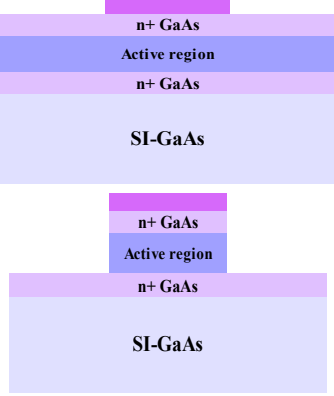
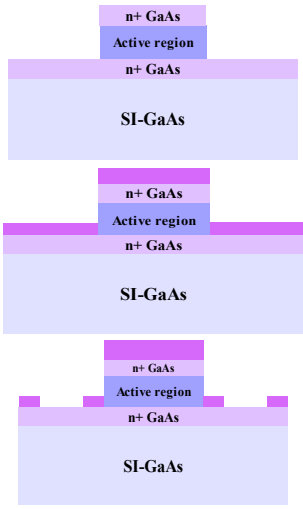
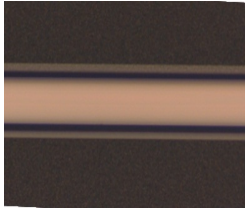

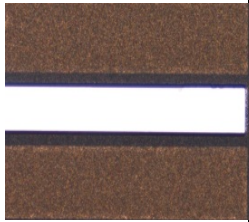
core directly to the heat-sink can be largely reduced in epilayer-down bonding. The possible technical problems include non-uniform bonding and solder voids. However, these problems can be overcome by optimising the bonding conditions, such as adjusting the ball size and the power. Moreover, thick electroplated Au provides an adequate area, thus preventing the laser facets or exposed device sides sinking into the indium solder, and improving the reliability of the epilayer-down bonding. [86]

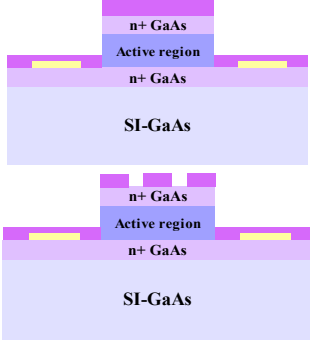
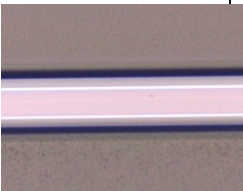
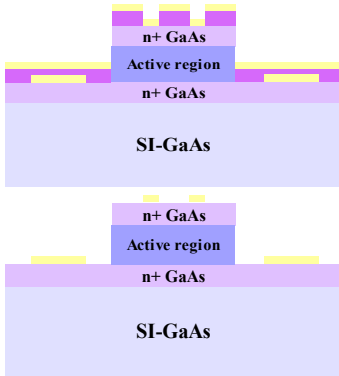
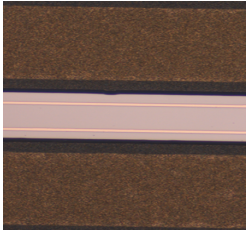

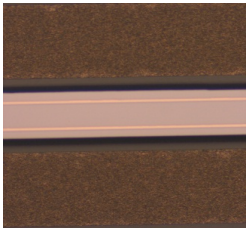
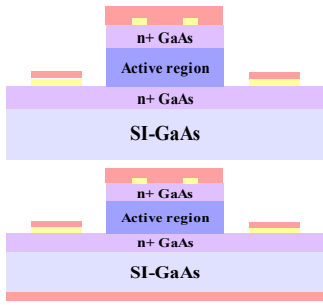
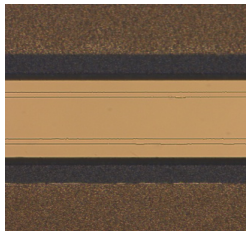
In the experiments, THz QCL devices were mounted epilayer up with a thin layer of indium on a copper block, and ceramic pads mounted on top of the copper block by high-thermal conducting glue GE Vanish. Gold wires were then bonded from the bottom and top contacts to the ceramic pads. The proper alignment of lasers requires the facets to be parallel to the edge of the copper block, ensuring that the emission of the laser is not blocked.

3.2.1 Fabrication procedures

The major steps of SISP QCL fabrication results, which includes both the schematic cross-sectioned diagrams of the device and the microscope photographs, are shown in Table 3.1. The main steps for DM THz QCL fabrication are shown in Table 3.2. The sloped walls after laser ridge etching are not shown in the pictures, since the shape of the wall would depend on the etchant and photolithography patterning direction.

Fabrication steps	Schematic cross section view	Microscope photograph (×10)
Photolithography for ridge and mesa etching		

		
<p>Photolithography for bottom contact</p>		
<p>Metallisation and annealing for bottom contact</p>		

<p>Photolithography for top contact</p>		
<p>Metallisation for top contact</p>		
<p>Photolithography for overlayer</p>		
<p>Backside thinning and metallisation</p>		

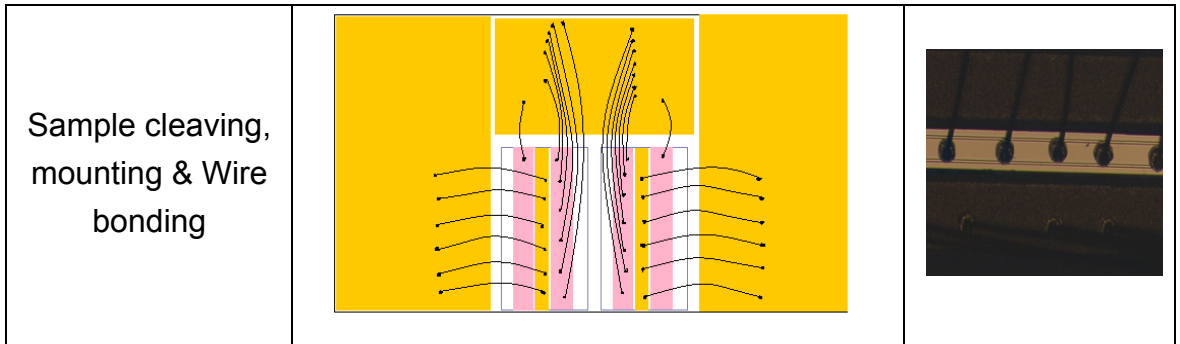
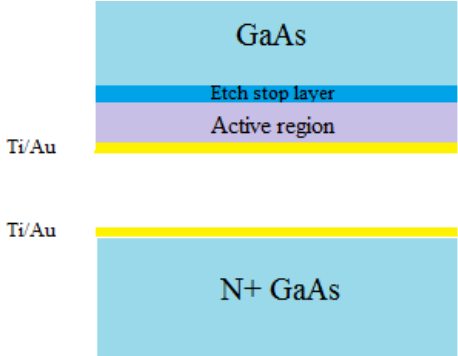
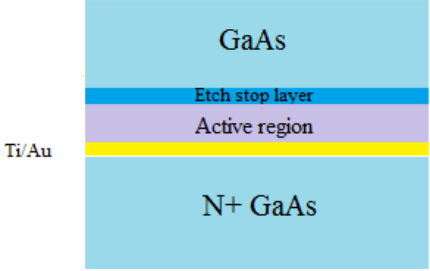
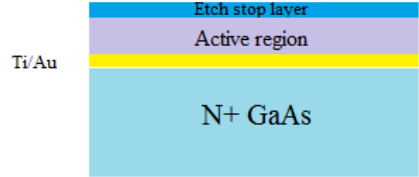
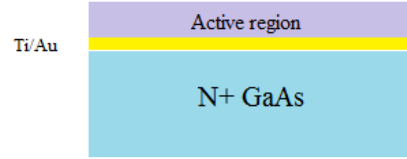
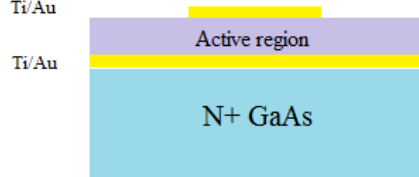
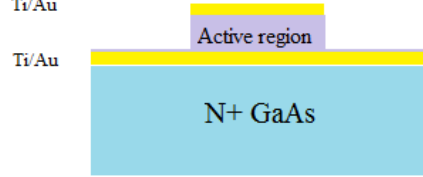


Table 3.1 Schematic cross view and microscope photographs of SISF QCL fabrication.

Task	Comments
Wafer cleaving and cleaning	Cleaning with Acetone, IPA, plasma ashing
Ti/Au coating	 <p>A cross-sectional diagram showing the layers of a device. From top to bottom: a light blue layer labeled 'GaAs', a thin blue layer labeled 'Etch stop layer', a purple layer labeled 'Active region', and a yellow layer labeled 'Ti/Au'. Below this, another yellow layer labeled 'Ti/Au' is shown above a light blue layer labeled 'N+ GaAs'.</p>

<p>Au thermo-compression bonding</p>	
<p>SI substrate removing</p>	
<p>The etch stop layer removing</p>	
<p>Photolithography and Ti/Au evaporation (Top contact)</p>	
<p>Ridge etching</p>	

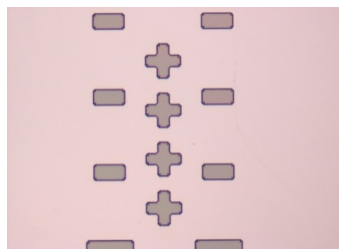
<p>Backside thinning</p>	
<p>Backside metallisation</p>	

Table 3.2 Main steps of DM THz QCL fabrication.

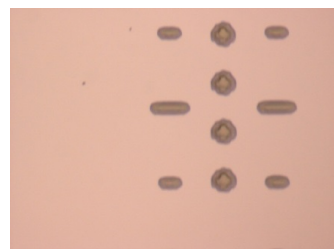
3.2.2 Photolithography

Photolithography is the process of reproducing geometric shapes on a mask to the surface of a wafer. The steps involved in the photolithographic process include wafer cleaning, photoresist spin, soft baking, mask alignment, UV exposure and development.

To transfer a pattern properly to the surface of a device, good contact between the mask and the sample is required without damaging the mask or the sample. Otherwise, as is shown in Fig. 3.2, the edges of the pattern will not be properly reproduced in the wafer, which can pose a serious problem, affecting subsequent processes.



(a) Proper contact



(b) False contact

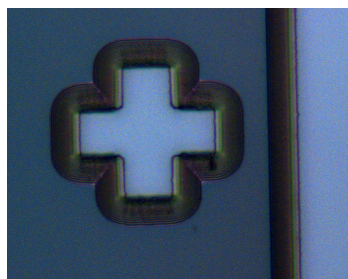
Figure 3.2 A microscope view (image scale: $\times 10$) showing proper and poor photolithography.

3.2.3 Wet etching

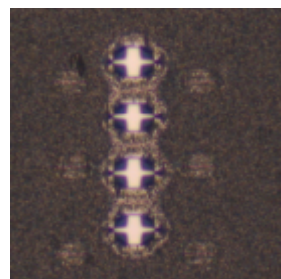
Wet etching was used in GaAs/AlGaAs THz QCL fabrication to avoid any surface electronic damage during processing. The chemical mechanism of GaAs wet etching is the oxidation of Ga and As on the surface, followed by chemical attack with acids to dissolve these oxides. [87] A wet etch process is more advantageous than a dry etch process when superior electronic properties are required, since the dry etch can cause surface damage by ion bombardment. [87] However, the main disadvantage of wet etching for many applications is the undercut of etch masks, which makes the dimension control inaccurate. This has been observed during both isotropic and anisotropic etching process. [87] Fig. 3.3 shows the cross-side image of a THz QCL ridge etching profile. The laser ridge has been deliberately defined vertical to the major flat of SI-GaAs substrate and was etched by the anisotropic etchant $\text{H}_2\text{SO}_4:\text{H}_2\text{O}_2:\text{H}_2\text{O}=1:8:40$. A clear undercut of the ridge can be observed. Fig. 3.4 shows the pictures of the same pattern etched by isotropic etchant ($\text{NH}_4\text{OH}:\text{H}_2\text{O}_2:\text{H}_2\text{O}=8:3:400$) and anisotropic etchant ($\text{H}_2\text{SO}_4:\text{H}_2\text{O}_2:\text{H}_2\text{O}=1:8:40$). Both show poor dimension control due to the side etch.



Figure 3.3 Anisotropic etching, laser ridge vertical to wafer major flat (image scale: $\times 10$).



(a)



(b)

Figure 3.4 GaAs substrate etching by (a) $\text{NH}_4\text{OH}:\text{H}_2\text{O}_2:\text{H}_2\text{O}=8:3:400$ (image scale: $\times 50$), (b) $\text{H}_2\text{SO}_4:\text{H}_2\text{O}_2:\text{H}_2\text{O}=1:8:40$ (image scale: $\times 10$).

To obtain a uniform etching surface, pre-cleaning and post-cleaning of the sample are critical steps. For example, to avoid local over-etching, the etching solution needs to be cleaned quickly after the sample is removed from the etchant. This problem becomes more significant when choosing a faster etching rate. Careful cleaning of residual organics from the exposed GaAs surface is important to avoid unwanted surface roughening. [87] In addition, the concentration of peroxide in the etching solution is a critical factor. For $\text{H}_2\text{SO}_4:\text{H}_2\text{O}_2:\text{H}_2\text{O}$ etchant, H_2O_2 is used to promote the formation of the surface oxides. However, a high concentration of H_2O_2 tends to cause bubbles on the substrate surface during etching, which can cause the surface roughness since the bubbles protect the surface from the etching solution. [87] The etching rate is also one of the most important factors which can be increased by increasing the H_2O_2 component of the etching solution. [87] However, poor surface quality can be caused by an excessively fast etching rate.

Fig. 3.5 shows a typical rough surface after laser ridge etching by $\text{H}_2\text{SO}_4:\text{H}_2\text{O}_2:\text{H}_2\text{O}=1:8:40$ ($1.2 \mu\text{m}/\text{min}$). A rough surface will cause potential problems in the metallisation and the final device bonding since the metal layer would be rough as well.

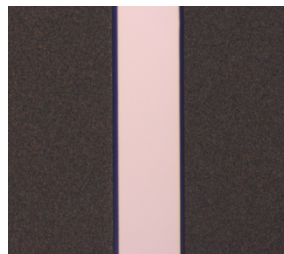


Figure 3.5 Surface after the laser ridge etching (sample L688) (image scale: $\times 10$).

Selective etching of $\text{Al}_x\text{Ga}_{1-x}\text{As}$ with $x > 0.4$ is possible with HF acid and the selectivity can be greater than 10:1. [87] Typically, $\text{Al}_{0.5}\text{Ga}_{0.5}\text{As}$ is used for the etch stop layer of DM waveguide THz QCL wafers. For the selective etching for GaAs over AlGaAs, organic acids such as citric acid and NH_4OH can be considered.

Fig. 3.6 shows the etching comparison between two DM THz QCL ridges, in which the active region material and a 600~700 nm n+ GaAs layer have been removed by $\text{H}_2\text{SO}_4:\text{H}_2\text{O}_2:\text{H}_2\text{O}=1:8:1$. However, in Fig. 3.6 (a), some n+ GaAs material is left, while in Fig. 3.6 (b) nearly all material has been etched

and the Ti/Au layer can be observed, which can possibly cause a short-circuit. Therefore, leaving some n+ GaAs material during etching is a more prudent option.

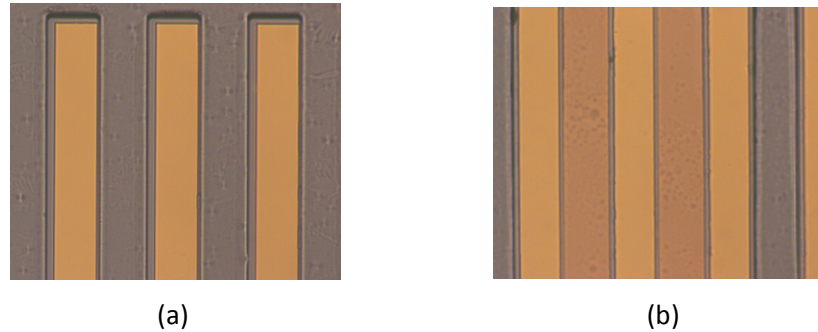


Figure 3.6 DM THz QCL ridge etching by $\text{H}_2\text{SO}_4:\text{H}_2\text{O}_2:\text{H}_2\text{O}=1:8:1$ (a) with some n+ GaAs material left (b) over etched surface (image scale: $\times 5$).

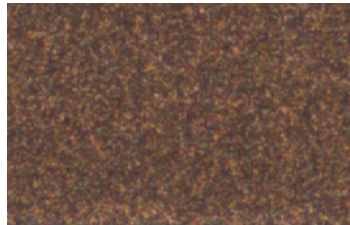
3.2.4 Ohmic contact

The close physical and chemical contacts between metals and semiconductors include Schottky and Ohmic contacts. For Ohmic contacts, the current increases linearly with the applied voltage, as per Ohm's law. To obtain the Ohmic contact, the barrier needs to be low or narrow enough to allow the current to cross the interface by thermionic or field emission. [87]

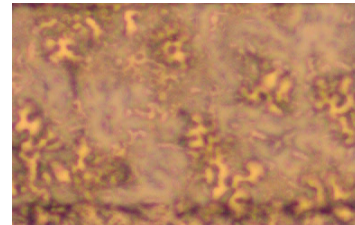
The metallisation is completed by a lift off process to remove all the unwanted metal. Annealing is used to diffuse Ge into the wafer and acts as a dopant [88]. During this process, Ni diffuses into GaAs material and reacts with the oxide. Intermediate complexes are formed between Ni and GaAs and the crystal lattice is disturbed, so that further diffusions and reactions can occur followed by the diffusion of Ge into GaAs. [87] Typically, this can be achieved by increasing the temperature to 430 °C for 1 min. Photographic examples of a normal annealing surface and an over-annealed (430 °C for 2 min) surface are shown in Fig. 3.7 (a) and (b). The over annealed surface is considerably rougher than the normal surface.

The main problem for the bottom contact is the lift-off after metallisation. Small pieces of Au can be observed sticking to the edge of the QCL ridges, in certain cases. This causes a short circuit between the top and bottom contacts. Some devices thus affected showed a high current at the beginning of a test and rapidly broke. In order to improve the lift-off process, another approach was attempted. The plasma ashing process before metal deposition was replaced by $\text{HCL}:\text{H}_2\text{O}$ (1:1) immersion, since plasma ashing

can damage the photoresist on the sample surface, especially the slope area of the ridge, and therefore cause difficulty in lift-off. Another role of the HCL:H₂O (1:1) solution is to remove the oxide layer of GaAs, which cannot be achieved by the plasma ashing. The reason to add this process is to decrease the resistance of the device as far as possible.



(a) Normal annealing



(b) Over annealed

Figure 3.7 Microscope view of an annealed surface of AuGeNi (image scale: $\times 10$).

3.3 Electrical characterisation of THz QCLs

There are several measurements that can provide information about a laser's performance. The most important are of the light-current-voltage (L-I-V) and spectral properties. The L-I-V provides the electrical property of a QCL, including its threshold current density and dynamic range, as well as the maximum operating temperature. The spectral properties, gives the information on the emission frequency of a QCL, as well as the guidance to the growth condition and the active region design.

Fig. 3.8 shows the measurement procedure for characterising QCLs. First, the laser is mounted on the cold finger of a helium flow-cryostat which is pumped down by a turbo pump. Liquid Helium is then connected to the cryostat to cool down the device. The facets of the devices are required to be parallel to a polythene window which allows laser emission to be collected by a QMC bolometer. The output signal of the bolometer is measured using a lock-in amplifier.

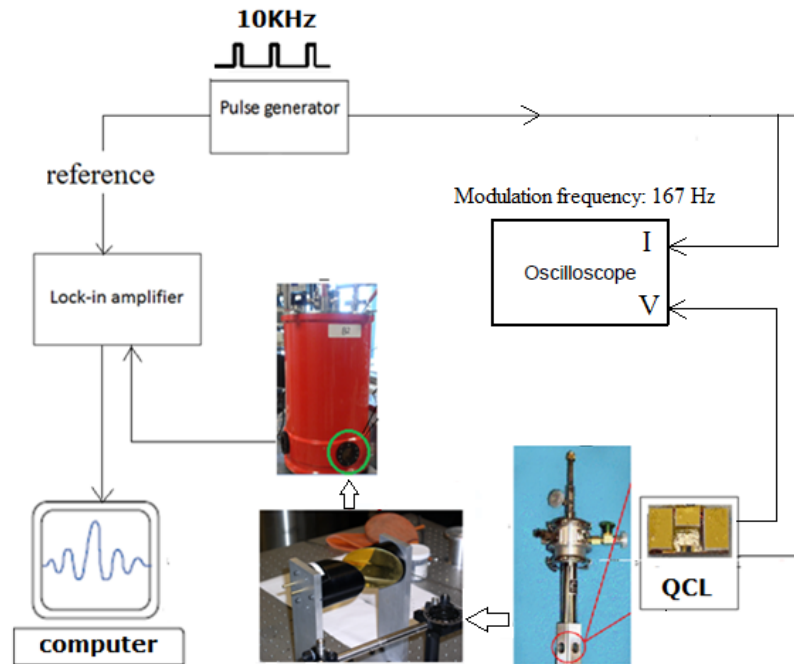


Fig. 3.8 Experimental set-up for QCL characterisation.

The measurement system consists of an Agilent 8114A signal generator for the electrical supply in pulsed mode, a 7225 DSP Lock-in amplifier and a QMC bolometer for THz radiation detection, a Tektronix TDS 2014 Digital Storage Oscilloscope for the voltage and current signal display, a temperature controller to control the temperature of the cold finger and a QMC bolometer detector. A Thomas Keating Power Meter is used for measuring the average power of THz QCLs. A Fourier Transform Infrared Spectrometer (FTIR) is used to measure the spectral properties of the QCL. Spectral measurements can be made more complicated by atmospheric and water absorption. By using dry nitrogen gas purging, the absorption can be minimized. Fig. 3.9 gives a comparison between QCL spectra and the blackbody spectra with nitrogen gas purging. [88]

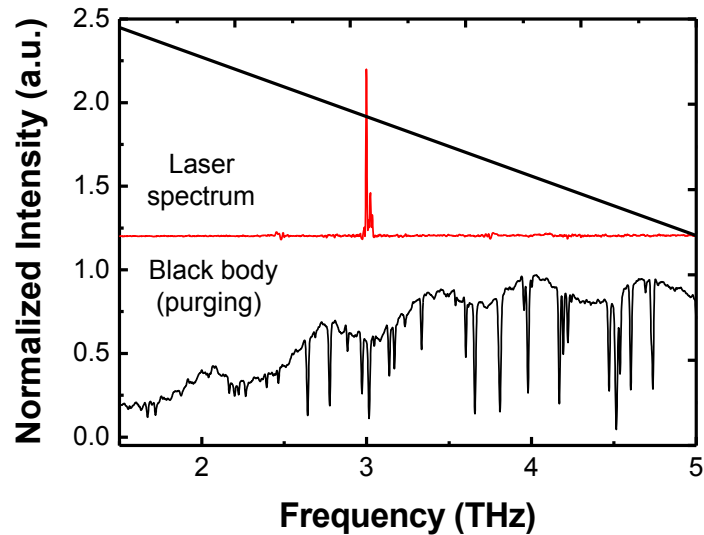


Figure 3.9 Comparison between the laser spectra and black body spectra (purged).

3.4 Summary

This chapter introduces the fabrication techniques and electrical characterisation of THz QCLs. The factors that influence the device performance during fabrication are explained and examples are given for comparison. The fabrication procedures for both SISP and DM THz QCLs are presented by cross-section diagrams and the details are explained. The measurement set-up for the electrical characterisation of THz QCLs is then outlined. Equipment details are given and the characterisation process, including power mapping, absolute power and spectra measurements, are illustrated in detail.

Chapter 4

High power THz QCLs

4.1 Introduction

High power THz sources have potential applications in many areas, including imaging and remote sensing. Spectroscopy involves illuminating many pixels and requires significant material penetration. Therefore high optical power is beneficial, especially since water vapour in air significantly attenuates THz radiation. [89]

THz QCLs are electrically driven and currently covering a frequency range from 1.2 to 5.2 THz; they are promising candidates for the above applications. There are different ways to improve the power performance of a THz QCL: optimizing the active region design, improving the material quality during growth, optimizing the fabrication process and improving the thermal dissipation. [86] Increasing the active region thickness can also considerably increase the power. Since the confinement factor is increased, the waveguide losses are reduced, and more optical power is generated inside the laser cavity. [90]

Two waveguides are used for THz QCLs, namely, the SISP waveguide and the DM waveguide. SISP waveguide provides a higher output power compared with DM waveguide. The active region is located between a metal layer at the top and a semi-transparent highly-doped GaAs layer at the bottom, in order to confine the optical mode within the active region. The resulting surface plasmon modes extend into the substrate and therefore the SISP waveguide suffers from poor optical confinement in the active region. The facet reflectivity of the SISP waveguide, which is calculated from the refractive index between the active region and air, is lower than in a DM waveguide, enabling higher out-coupling of radiation. [90] For the DM waveguide, the active region is located between a top and bottom metal layer, and this provides high confinement of the optical mode within the active region. However, the comparatively high facet reflectivity prevents the efficient out-coupling of the generated optical power. [90]

There has been notable progress in the development of high power THz QCLs. In 2006, 4.4 THz QCLs were demonstrated with 248 mW peak power in pulsed mode, and 138 mW in continuous mode at heat-sink temperatures

of 10 K, by Williams et al. from Massachusetts Institute of Technology. [89] In 2007, 145 mW peak output power at 5 K was achieved from a DM waveguide 4.1 THz QCL with an abutted silicon hyper-hemispherical lens, by Lee et al. from Massachusetts Institute of Technology. [91][92] In 2013, a 3.9 THz QCL with SISP waveguide employing a stack of two symmetric active regions was demonstrated by the Technical University of Vienna with 470 mW from a single facet (940 mW two-facet output power) in pulsed mode. [90]

In this chapter, a new method (large area) for improving THz QCL power is explained, and the factors that influence THz QCL power performance are investigated. The simulation and experimental details are given and analysed in order to optimize the output power. The highest ever reported power (1 W) is demonstrated for a THz QCL (in pulsed mode, at a heat-sink temperature of 10 K), and this result has also been presented in [53, 72-75].

4.2 Active region structure

The structure used in our high power demonstration is based on a BTC THz QCL design with a single-quantum-well phonon extraction/injection stage. More details can be found in [47].

This structure combines the advantages of both BTC and RP designs. The lasing relies on a diagonal transition between a bound state and doublet of states, that themselves are tunnel coupled to the upper state of a phonon extraction stage. This structure has the advantage of a wide gain bandwidth, and favourable high-temperature characteristics. [47] It is, therefore, a good choice for demonstrating high output power.

The active region of the laser is composed of 180 repeat periods grown via MBE in GaAs/AlGaAs material system. The computed band structure of such a laser is shown in Fig. 4.1. The lasing occurs from level 4 to level 3 with a diagonal transition followed by scattering through minibands and LO phonon extraction from level 2 to level 1.

The THz QCL structure consists of a three quantum well active region followed by a one-well injector region in the $\text{Al}_{0.16}\text{Ga}_{0.84}\text{As}/\text{GaAs}$ materials system. The layer sequence of the structure starting from the injector barrier is **52**/103/**17**/107.5/**36**/88/**39.5**/172, where the thicknesses are in Å, the $\text{Al}_{0.16}\text{Ga}_{0.84}\text{As}$ barriers are in bold, and the Si-doped layer ($3 \times 10^{16} \text{ cm}^{-3}$) is

underlined. According to the calculation (Fig. 4.1), lasing is expected at ~3.4 THz with the applied electric field of 7.6 KV/cm.

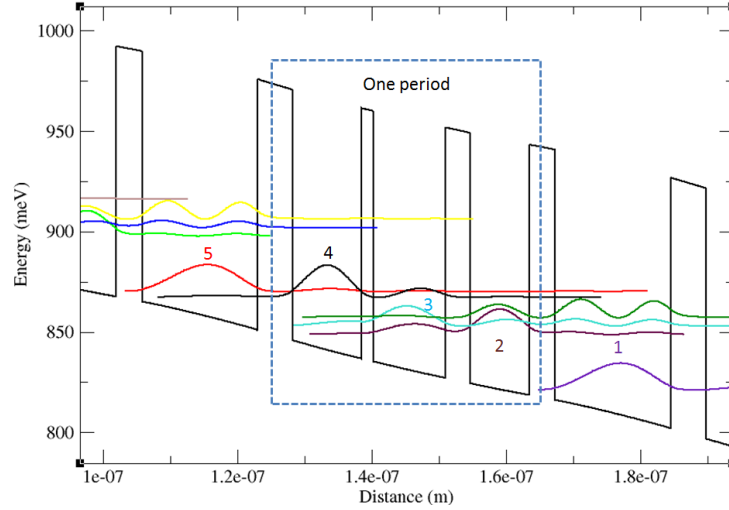


Figure 4.1 Conduction-band diagram and electron subband wave functions squared at T=10 K, calculated self-consistently using Schrödinger–Poisson solver [1]. An electric field of 7.6 KV/cm is applied to align the structure. The GaAs/Al_{0.16}Ga_{0.84}As layer sequence of one period of the active layers starting from the injection barrier is: **52/103/17/107.5/36/88/39.5/172**, where the thicknesses are in Å, Al_{0.16}Ga_{0.84}As barriers are in bold, and the underlined number correspond to a Si-doped layer with a concentration of $3 \times 10^{16} \text{ cm}^{-3}$.

4.3 Modelling and simulation

4.3.1 SISP waveguide simulation introduction

Both a gain medium and a resonator are required for a laser. The THz radiation must be confined and the optical feedback is provided by the resonator. The absorption loss should be kept to a minimum.

In order for lasing to occur, the total gain in the QCL structure must be larger than the total losses, including the waveguide loss α_w and the mirror loss α_m .

The gain coefficient is determined by the following equation,

$$g = \tau^* \left(1 - \frac{\tau_3}{\tau_{43}}\right) \frac{2\pi e z^2}{\lambda \epsilon_0 n_{\text{eff}} L Y} \quad (4.1)$$

Where τ^* is the normalized upper state life time, τ_3 is the lower level life-time, τ_{43} is the intersubband optical-phonon-limited relaxation time, z is the optical

matrix element between the upper and lower radiative states, λ is the wavelength in vacuum, ϵ_0 is the vacuum dielectric constant, n_{eff} is the effective mode index of the waveguide, e is the elementary charge, L is the length of one period of the active region, and γ is the broadening of the optical transition. [37]

The threshold gain g_{th} is defined by

$$\Gamma g_{th} = \alpha_w + \alpha_m, \quad (4.2)$$

where Γ is the confinement factor of the mode in the active region. α_w is the waveguide loss, and α_m is the mirror loss.

Therefore, when the gain is large enough to satisfy equation (4.1), lasing occurs and the threshold current is defined as

$$J_{th} = \frac{\alpha_w + \alpha_m}{g\Gamma} \quad (4.3)$$

The threshold current density will be larger due to the decrease of gain coefficient, if other factors remain the same.

The waveguide loss α_w is given by

$$\alpha_w = 2\alpha \quad (4.4)$$

Where α is the absorption coefficient and the mirror loss α_m can be calculated from

$$\alpha_m = \frac{1}{L} \ln(R) \quad (4.5)$$

where L is the cavity length and R is the Fresnel reflection coefficient at the semiconductor/air interface. The effect of mirror loss α_m can be minimized by using high-reflective mirrors or longer cavity lengths. Also, the longer the cavity, the greater the waveguide absorption loss α_w .

For a given gain coefficient, large Γ and small α are preferable in the waveguide design in order to give a small threshold current density.

The effective mode index n of the waveguide mode is determined by the phase propagation constant β

$$n = \frac{\beta}{k_0} \quad (4.6)$$

$E_y(x)$ can be plotted and therefore Γ can be calculated by

$$\Gamma = \frac{\int_0^d |E_y(x)|^2 dx}{\int_{-\infty}^{+\infty} |E_y(x)|^2 dx} \quad (4.7)$$

where d is the width of the active region. [6]

For a Fabry-Pérot cavity laser, equation (4.5) can be written as

$$\alpha_m = \frac{1}{2L} \ln \left(\frac{1}{R_f R_b} \right) \quad (4.8)$$

where L , R_f , and R_b are the cavity length, front facet reflectivity and back facet reflectivity, respectively.

Therefore, the mirror loss of the laser will be decreased by increasing the back facet reflectivity. This will lead to the decrease of threshold current density, according to equation (4.3).

4.3.2 SISP waveguide simulation results

In order to demonstrate the advantages of using broader area THz QCLs, the gold top waveguide with a modified hybrid THz QCL structure was simulated [47]. The highly doped n+ GaAs layer ($n = 3.5 \times 10^{18} \text{ cm}^{-3}$) with a thickness of 600 nm is included in the simulation. Simulations were carried out for the following set of laser ridge widths: 130 μm , 145 μm , 174 μm , 223 μm , 274 μm , 328 μm , 374 μm and 426 μm . All simulations use a (thinned) substrate thickness of 180 μm .

For each set of simulations, the values for confinement factor Γ , waveguide loss α_w , and threshold gain were calculated, together with the mirror losses for different laser cavity lengths. A facet reflectivity of 0.32 was used, assuming:

$$R_{SISP} = (n_{AR} - 1)^2 / (n_{AR} + 1)^2, \quad (4.9)$$

where n_{AR} is the active region refractive index, representing the reflectivity due to the refractive index difference between the laser and air.

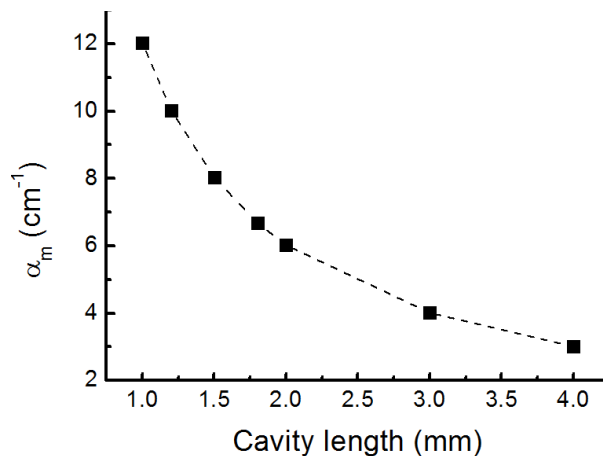


Figure 4.2 Calculated mirror loss as a function of laser cavity length.

Fig. 4.2 shows the mirror loss dependence on laser cavity length. The calculated results show that the value of mirror loss decreases with cavity length, which is expected from equation (4.5).

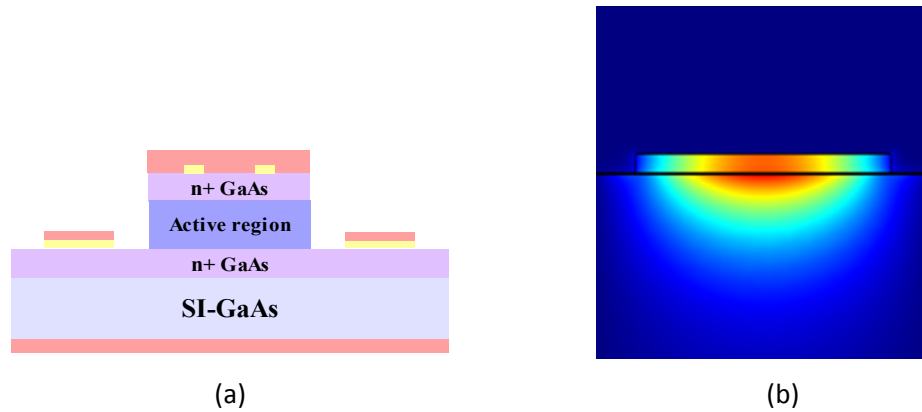


Figure 4.3 (a) Schematics of the SISP waveguide (b) two-dimensional electromagnetic mode calculations for the fundamental lateral modes obtained using finite-element solver (COMSOL).

Fig. 4.3 shows the schematically the SISP waveguide, and a two dimensional model of the mode distribution across the cross-section of a SISP waveguide with a 11 μm thick active region, calculated using a finite element solver (Comsol Multiphysics). From this, the confinement factor Γ can be extracted. In order to determine accurately the waveguide losses, one-dimensional calculations based on transfer-matrix formalism were used for computing the relative permittivity, conductivity and layer refractive indices.

Fig. 4.4 and Fig. 4.5 show the effect of varying the laser ridge width on the confinement factor and waveguide loss for two different active region doping levels. As the waveguide width decreases, the confinement of the mode degrades. The reason is that when the waveguide becomes narrow, the modes are squeezed into the substrate, thus making the confinement factor smaller. [83] This also leads to larger losses at the bottom doped contact.

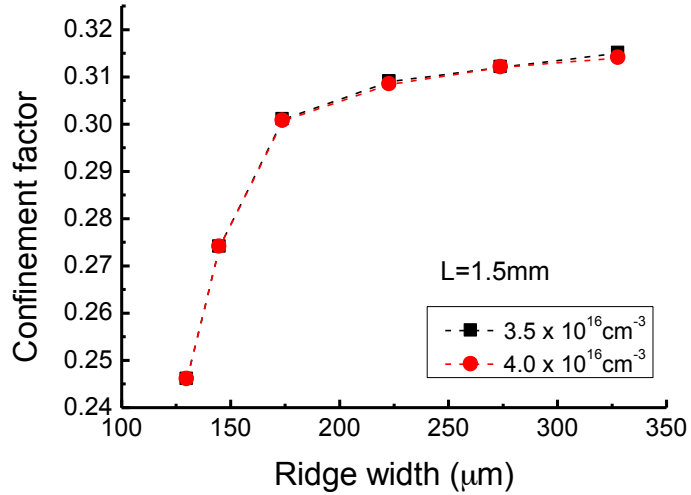


Figure 4.4 2D confinement factor as a function of ridge width for active region doping levels of $3.5 \times 10^{16} \text{ cm}^{-3}$, and $4 \times 10^{16} \text{ cm}^{-3}$. The bottom contact doping is $3.5 \times 10^{18} \text{ cm}^{-3}$ and the laser cavity length was 1.5 mm.

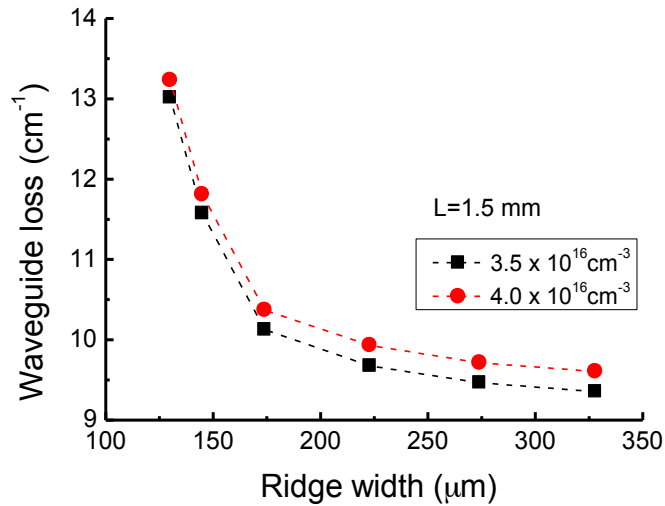


Figure 4.5 2D waveguide loss as a function of ridge width for active region doping levels of $3.5 \times 10^{16} \text{ cm}^{-3}$, and $4 \times 10^{16} \text{ cm}^{-3}$. The bottom contact doping is $3.5 \times 10^{18} \text{ cm}^{-3}$ and the laser cavity length was 1.5 mm.

The waveguide loss thus increases as the laser ridge width decreases. The confinement factor does not, however, change much with the active region doping level, whilst the higher active region doping leads to a higher waveguide loss, as would be expected. The resulting extracted threshold gains are summarized in Table 4.1.

g_{th} (cm^{-1})		Ridge Width (μm)					
		130	145	174	223	274	328
Length (mm)	1	79	72	64	63	62	62
	1.2	72	66	62	61	60	60
	1.5	65	59	56	54	54	57
	1.8	60	55	51	50	49	49
	2	58	52	49	48	47	47
	3	51	46	43	41	41	41

Table 4.1 Threshold gain for devices at different cavity lengths and ridge widths.

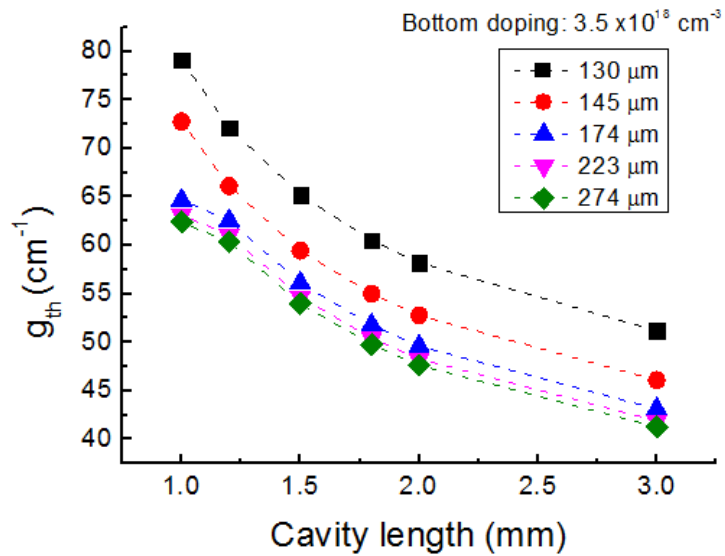


Figure 4.6 2D simulation results of threshold gain as a function of laser cavity length with ridge widths from 130 μm to 274 μm .

Fig. 4.6 is a summary of the threshold gain dependence on cavity length, with g_{th} simulated for different laser ridge width. As the QCL cavity length increases, the threshold gain decreases. For the same cavity length, the threshold gain also decreases as the laser width is increased. Therefore, the threshold current densities are expected to be lower for devices with wider ridges or longer cavity lengths, as expected from equations (4.1) and (4.3).

In Fig. 4.7, simulation results of threshold gain are plotted as a function of ridge width for different laser cavity lengths. The threshold gain decreases with an increase of ridge width, as expected. For a 1 mm long laser, g_{th} is decreased by 21% as the ridge width increases from 130 μm to 328 μm , and decreased by 19.2% when the length is increased to 3 mm. However, there was an sudden increase of the threshold gain for 328 μm -wide and 1.5 mm-

long device. This is possibly due to the imperfection of the cleaved facets which increased the mirror loss.

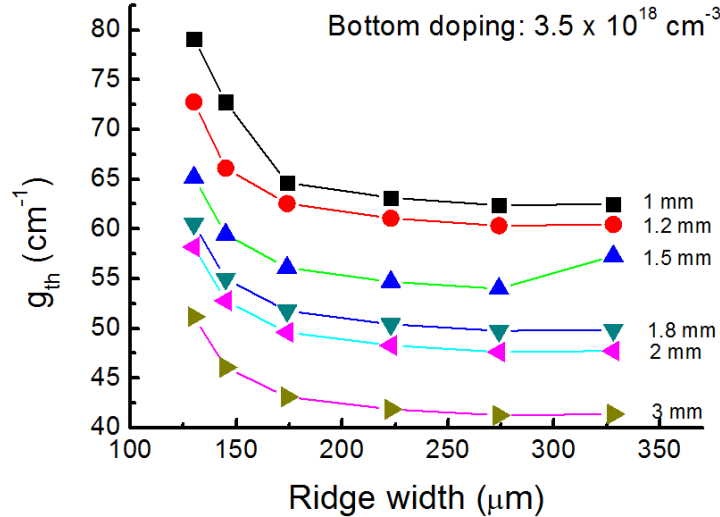


Figure 4.7 Threshold gain as a function of laser ridge width for different cavity lengths with a plasma doping level at $3.5 \times 10^{18} \text{ cm}^{-3}$.

4.4 Experimental Results

4.4.1 Device Measurement

High power THz QCLs are demonstrated by fabricating broad area laser ridges with SISF waveguide. Laser ridges ranged from 145 to 426 μm . The devices were cleaved into 1 to 4.2 mm lengths and bonded epilayer-up onto gold coated copper heat-sinks with indium solder. All testing was carried out with a pulse width of 250 ns and a duty cycle of 2% (a repetition rate of 10 KHz). The optical output power from a single facet of the laser was measured by a Thomas Keating (TK) calibrated absolute power meter mounted directly in front of the cryostat window, without any correction for the collection efficiency. Low temperature testing was carried out with a liquid-helium-cooled cryostat with 1.5 mm-thick polyethylene windows, while the separation between the laser facet and power meter was 3.5 cm. Spectra were measured with a Bruker FTIR in rapid scan mode. [53]

4.4.2 Comparison between simulation and experimental results

Previous simulation results show that by using broader area SISF waveguides and decreasing the mirror losses, higher output power can be

achieved. Experimental results are shown in Fig. 4.8 and Fig. 4.9, and compared with the simulation results.

In Fig. 4.8, two sets of results are given for lasers with 145 μm and 426 μm ridge width. The threshold current densities are compared at heat-sink temperature of 10 K. For both ridge widths, J_{th} decreases with the cavity length, and generally, the threshold current densities of the lasers with 426 μm width are lower than with 145 μm width for the same cavity length, as expected from the simulations (Fig. 4.7).

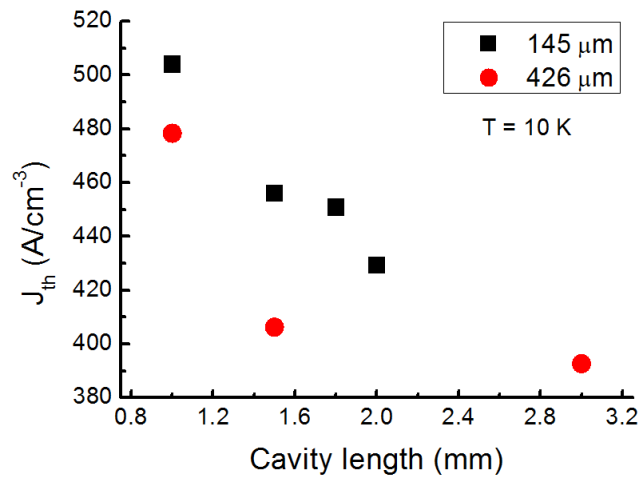


Figure 4.8 Threshold current density as a function of laser cavity length for 145 μm and 426 μm ridge widths, at a heat-sink temperature of 10 K.

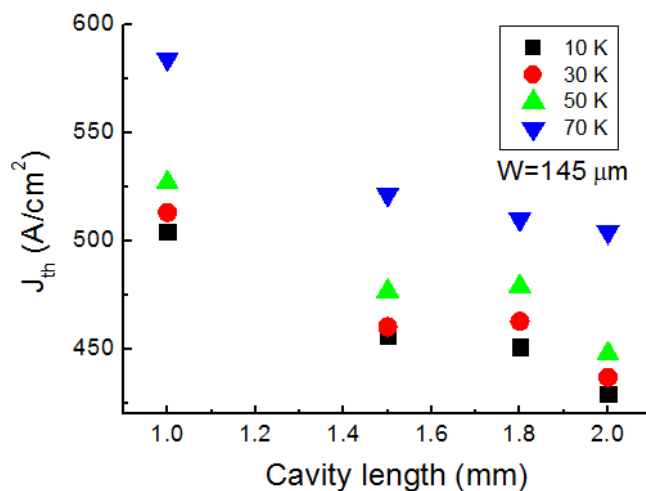


Figure 4.9 Threshold current density as a function of laser cavity length at different heat-sink temperatures.

Fig. 4.9 presents the threshold current density as a function of laser cavity length for 145 μm lasers at heat-sink temperatures of 10 K, 30 K, 50 K, and 70 K. The cavity lengths are 1.0 mm, 1.5 mm, 1.8 mm, and 2.0 mm. For lasers with the same cavity length, the threshold current density increases with the heat-sink temperature, due to the in-plane scattering mechanism and the intersubband scattering and consequently the decrease of upper-state life time. [93] The figure also shows that the threshold current density decreases with the increase of cavity length due to the decrease of mirror loss (equation (4.3) and(4.8)).

The above experimental results in Fig. 4.8 and Fig. 4.9, agree with the simulation results, see Fig. 4.6 and Fig. 4.7. The threshold current density decreases with the increase of laser cavity length. In addition, lower threshold current density is attained from lasers with wider laser ridge width.

4.4.3 Summary of results for different cavity lengths/widths

Dimensions L (mm) \times W (mm)	J_{th} (A/cm ²)	P_{max} (mW)	T_{max} (K)
1.5 \times 145	456	121	102
1.5 \times 174	443	145	105
1.5 \times 223	434	173	102
1.5 \times 374	435	350	102
1.5 \times 426	406	391	105

Table 4.2 Performance of THz QCLs with different ridge widths, for a device Length of 1.5 mm.

Dimensions L (mm) \times W (μm)	J_{th} (A/cm ²)	P_{max} (mW)	T_{max} (K)
1 \times 145	517	30	81
1 \times 223	374	63	80
1 \times 277	436	116	99
1 \times 374	426	113	87
1 \times 426	465	200	100

Table 4.3 Performance of THz QCLs with different ridge widths for a device. Length of 1 mm.

Initially, a standard processing technique was used, from which two sets of devices were measured with a range of laser cavity lengths and widths. The data of devices with 1.5 mm ridge length and five different ridge widths is

shown in Table 4.2, whilst in Table 4.3, results are presented from all devices were cleaved into a 1 mm length.

4.4.4 Facet coating and increasing of the device performance

To increase the output power, larger area ridges were fabricated. A power of 773 mW at 10 K was achieved with a 2% duty cycle from a 3 mm x 426 μm ridge. The L-I-V and spectra of this device are shown in Figs. 4.10 and 4.11, respectively.

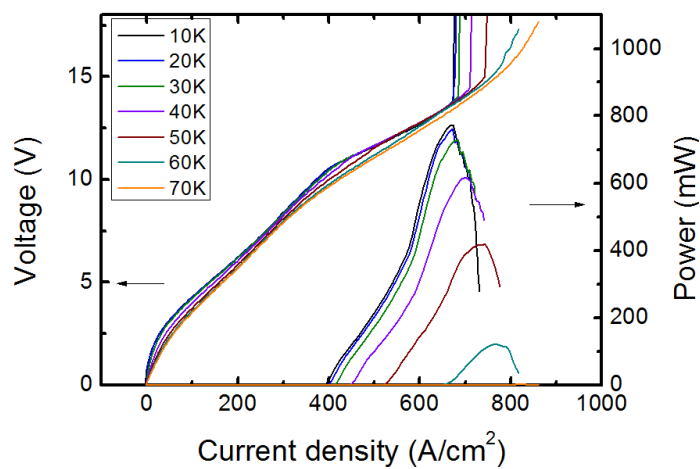


Figure 4.10 L-I-V curves of a high power THz QCL (426 μm x 3 mm) with a hybrid THz QCL active region incorporating a single-quantum-well phonon extraction/injection stage. Results were measured with a 2% pulse duty cycle.

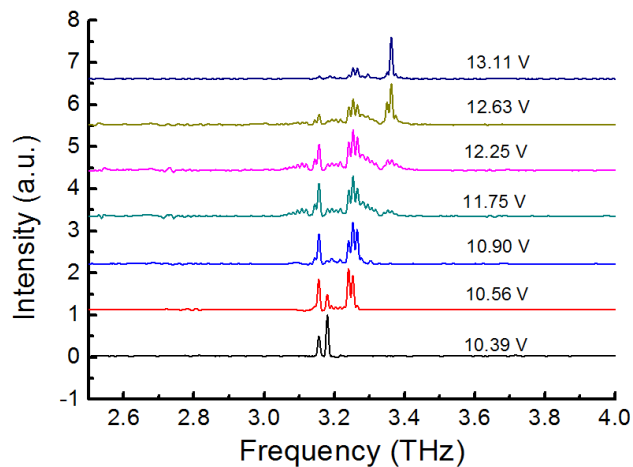


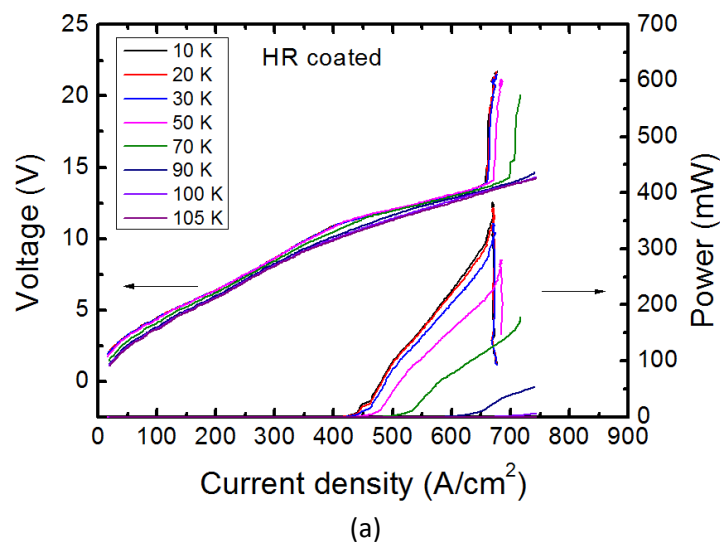
Figure 4.11 Spectra recorded at 10 K with a 2% pulse duty cycle at different biases for a THz QCL of dimensions 426 μm x 3 mm.

At the heat-sink temperature of 10 K, the laser started lasing at a threshold of 393 A/cm^2 , and reached the peak output power 773 mW at the current density of 673 A/cm^2 . The device lased at 3.2 THz near threshold, but ranged from 3.2 to 3.4 THz under different bias, as expected from the design.

In order to increase the output power, a second run of fabrication was undertaken in which a high reflection (HR) coating was applied to the back facet of THz QCLs. HR coating increases reflectivity of the back facet, so the mirror loss of the THz QCL decreases. Therefore, a smaller cavity length can be used for the same mirror loss.

Devices were fabricated using a standard SISP QCL fabrication procedure, and then back facet coated by electron beam evaporation with a high reflection thin film, composed of $\text{SiO}_2(150 \text{ nm})/\text{Ti}(10 \text{ nm})/\text{Au}(150 \text{ nm})/\text{SiO}_2(200 \text{ nm})$.

Fig. 4.12 shows the pulsed mode (2% duty cycle) comparison between HR coated and uncoated THz QCLs. Both devices came from the same SISP processed THz QCL wafer, and had the same ridge width of $328 \mu\text{m}$ and the same cavity length of 1.8 mm . Both devices worked up to 105 K . Further comparisons are made and shown in Fig. 4.13, where V-J and output power as a function of current density (P-J) are shown with and without facet coating are compared at heat-sink temperature 10 K . The facet coated device shows a 7% reduction in threshold current density from 438 to 407 A/cm^2 , and a 37% increase of peak output power from 280 to 380 mW .



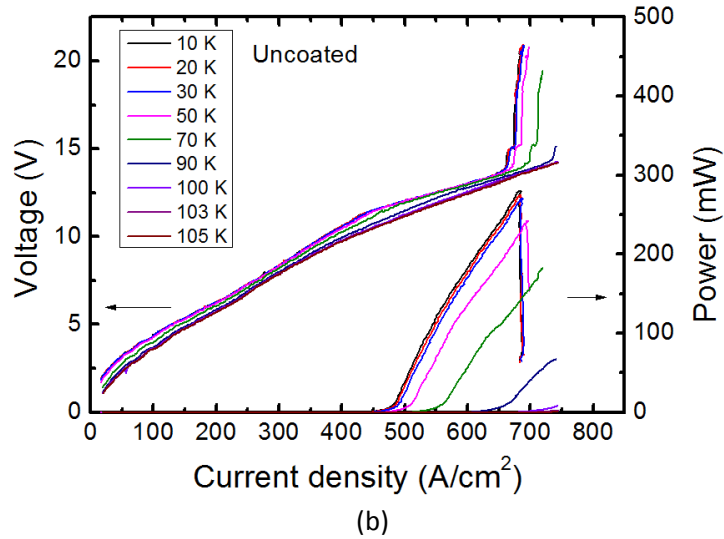


Figure 4.12 L-I-V curves of THz QCLs ($L=1.8$ mm, $W=328$ μm) obtained with a 2% pulse duty cycle at various heat-sink temperatures, (a) HR coated (b) uncoated.

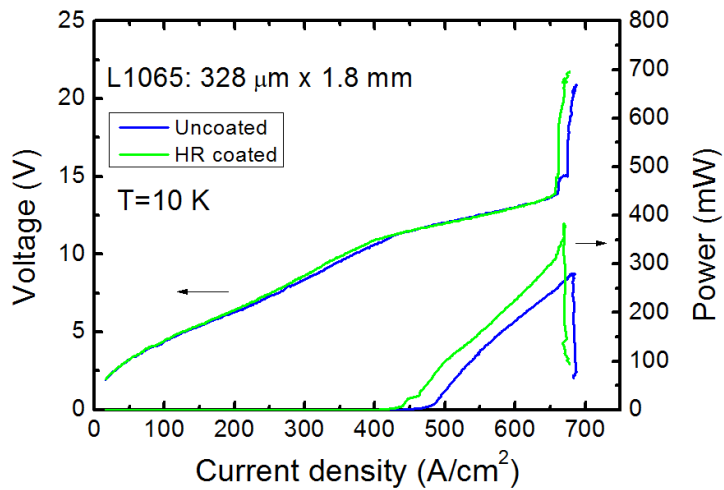


Figure 4.13 L-I-V characteristics comparison between facet coated and uncoated QCL devices for a cavity length of 1.8 mm, and a ridge width of 328 μm .

The threshold current density at different heat-sink temperatures are then plotted in Fig. 4.14, from 10 K to 105 K. The threshold current density of the HR coated device is lower than the uncoated device at all heat-sink temperatures.

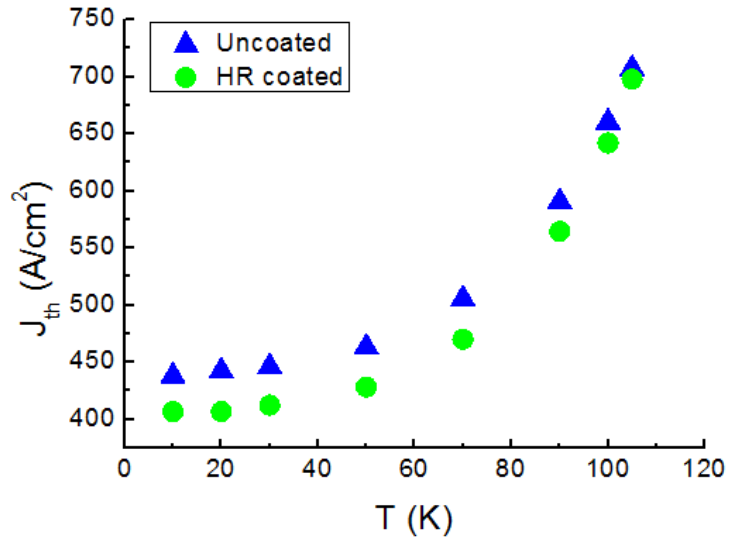
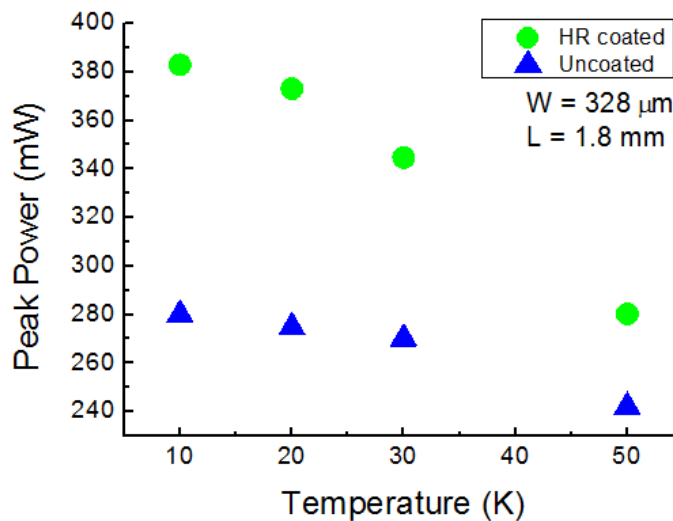


Figure 4.14 Threshold current density comparison between facet coated and uncoated devices as a function of temperature.

Fig. 4.15 then shows the variation of peak output power as a function of heat-sink temperature for both THz QCLs with and without HR-coating. The peak output power decreases with the increase of heat-sink temperature for both devices. For all temperatures, the HR coated device gives a much higher power compared with uncoated device. By normalizing the peak power, it is seen that the peak output power of the HR coated device decreases faster with an increase of heat-sink temperature than the uncoated device. The possible reason is that the lower mirror loss in HR coated device makes the temperature influences on output power more obvious.



(a)

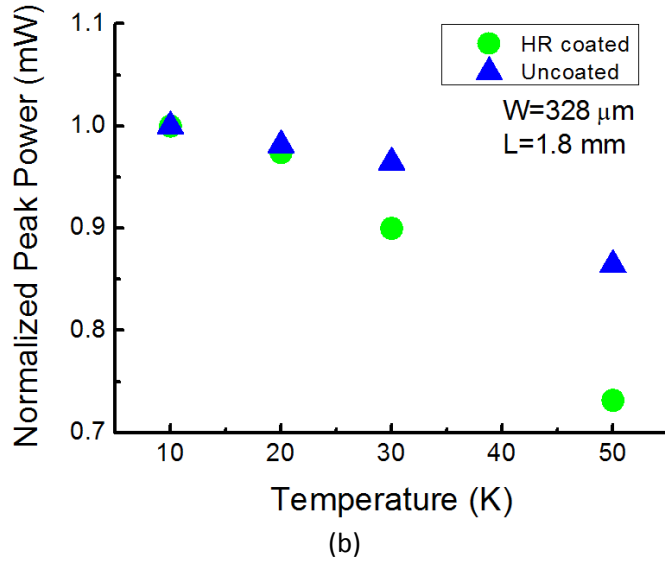


Figure 4.15 Peak output power as a function of heat-sink temperature, (a) measured power, (b) normalized power.

The peak output power of a THz QCL can be described by:

$$P_{max} = \eta N_p \frac{h\nu}{e} \frac{\alpha_{m1}}{\alpha_m + \alpha_w} \left(1 - \frac{\tau_3}{\tau_{43}}\right) (J_{max} - J_{th}) lw \quad (4.10)$$

where $\alpha_{m1} = -\frac{1}{2l} \ln(R_1)$, $\alpha_{m2} = -\frac{1}{2l} \ln(R_2)$, and

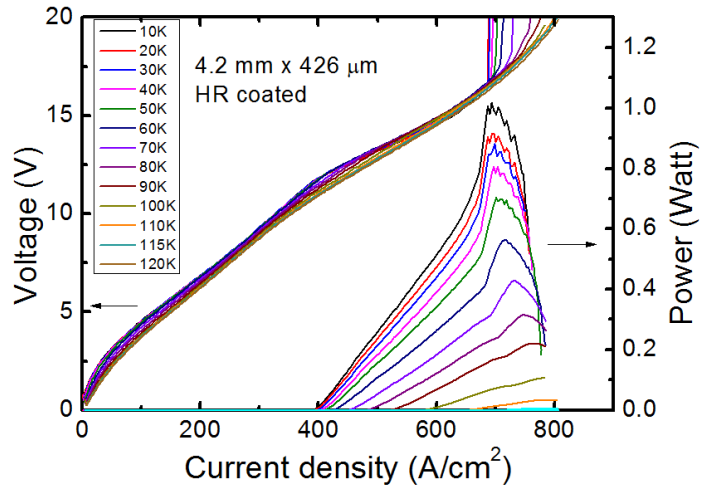
$\alpha_m = \alpha_{m1} + \alpha_{m2}$ is the mirror loss of both the front facet and back facet.

$J_{max} = \frac{eN_s}{2\tau_3}$ is the current density when the lasing reaches its maximum power.

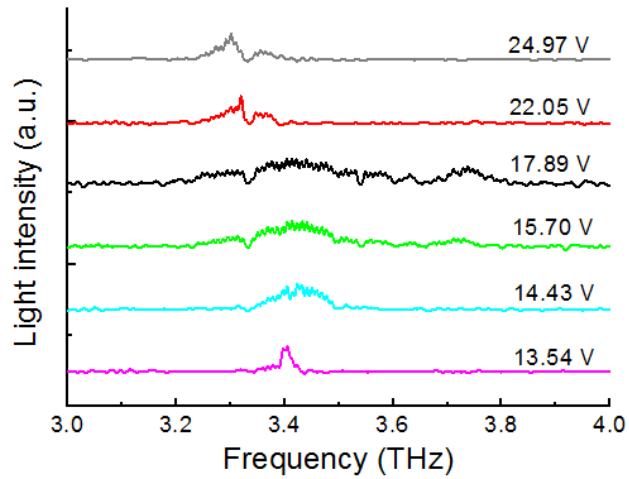
Therefore, according to equation (4.8) and (4.9), since the mirror loss of the back facet is decreased by HR coating, the peak power increases.

To increase the output power further, the device dimensions were increased to 4.2 mm x 426 μm). Fig. 4.16 (a) and (b) show the resulting performance, in pulsed mode with a 2% duty cycle. The device operates up to 120 K with a 1.01 Watt power is obtained at heat-sink temperature of 10 K, and a dynamic range of 294 A/cm². A peak power of 420 mW is obtained at 77 K, with a dynamic range of 167 A/cm².

The spectral properties are shown in Fig. 4.16 (b), as a function of bias. The lasing frequency is between 3.3 THz to 3.5 THz. The spectra becomes wider when the applied voltage increases from 13.54 V to 17.89 V, but becomes narrower after 17.89 V when the lasing reaches the negative differential resistance (NDR) region and the misalignment occurs.



(a)



(b)

Figure 4.16 (a) L–I–V curves (b) spectra of THz QCLs ($L = 4.2$ mm, $W = 426$ μm) obtained with a 2% pulse duty cycle at various heat-sink temperatures.

4.4.5 Threshold current density dependence on device area

The influence of device area on the threshold current density is analysed below. Fig. 4.17 and 4.18 show the threshold current densities as a function of heat-sink temperature for lasers with 426 μm and 145 μm ridge width and different cavity lengths. The threshold current density increases with the increase of heat-sink temperature, as explained in 4.4.2.

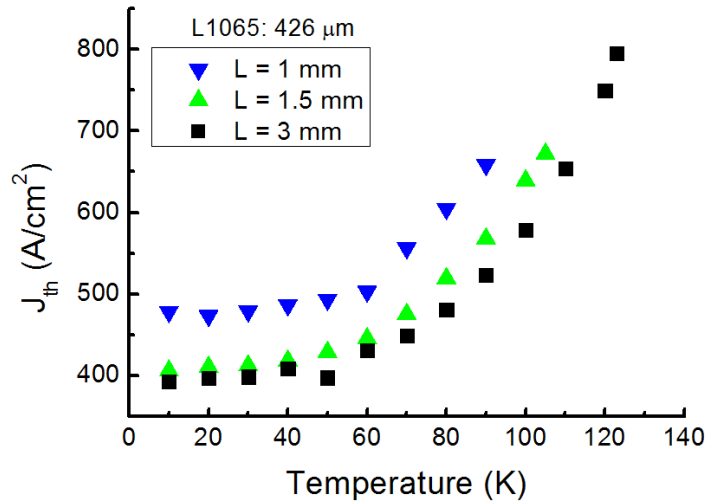


Figure 4.17 Threshold current density as function of heat-sink temperature, for a laser of width 426 μm , and ridge lengths of 1, 1.5, 3 mm.

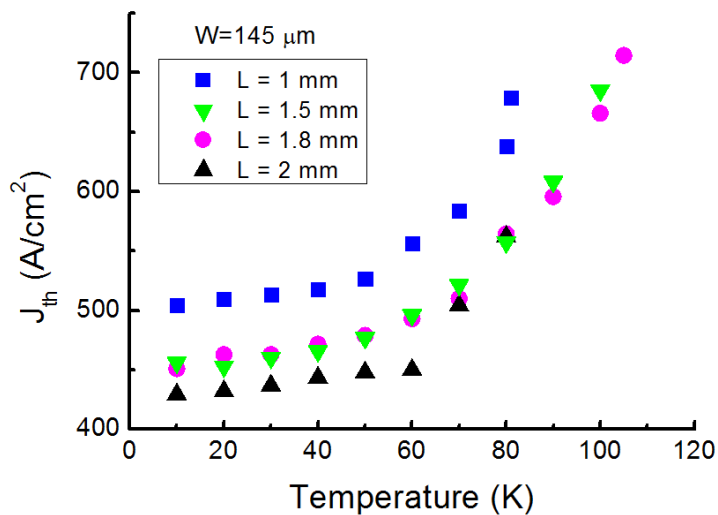


Figure 4.18 Threshold current density as function of heat-sink temperature, a laser width of 145 μm , and ridge lengths of 1, 1.5, 1.8, 2 mm.

For 1 mm, 1.5 mm, and 3 mm long devices with 426 μm ridge width, the threshold current densities at 10 K are 478 A/cm^2 , 406 A/cm^2 and 393 A/cm^2 , respectively.

For a 145 μm ridge width, devices with 1 mm, 1.5 mm, 1.8 mm and 2 mm cavity length are compared. Similarly, the threshold current density increases with the lase cavity length. The threshold current densities at 10 K are 504 A/cm^2 , 456 A/cm^2 , 451 A/cm^2 and 429 A/cm^2 .

For both sets of results, the threshold current density shows relatively weak temperature dependence initially. However, it changes abruptly after 50 K, showing a much faster increase of the J_{th} .

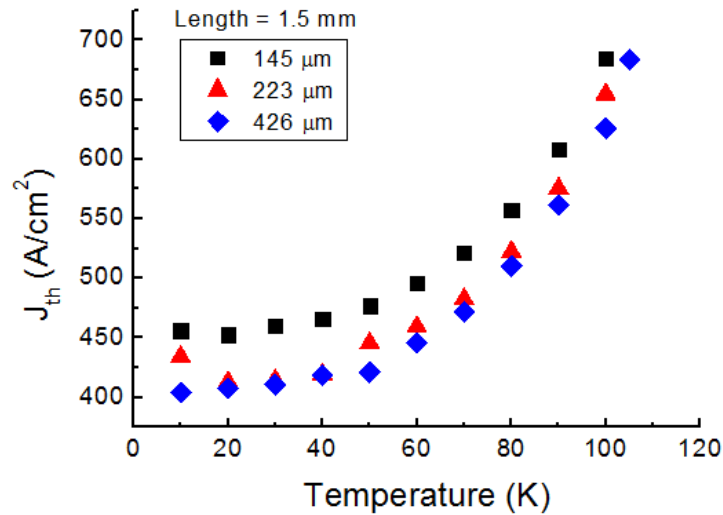


Figure 4.19 Threshold current density as a function of heat-sink temperature for 1.5 mm-long lasers with ridge widths of 145, 174, 223, 374 and 426 μ m.

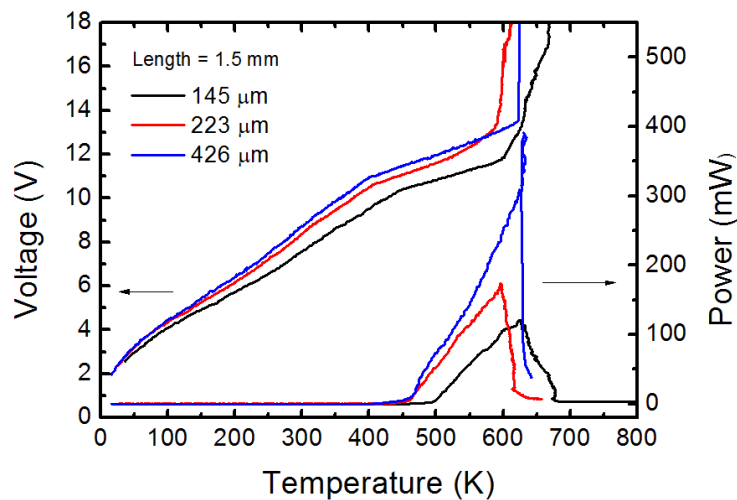


Figure 4.20 L-I-V curves of three THz QCLs ($L=1.5$ mm, $W=145$, 223, 426 μ m) obtained with a 2% pulse duty cycle at heat-sink temperature of 10 K.

Fig. 4.19 and Fig. 4.20 compare 1.5 mm lasers with three different ridge widths. 1.5 mm long devices with 145 μ m, 223 μ m and 426 μ m ridge width are measured and the results compared in Fig. 4.19. It is observed that the

lasing threshold of the 426 μm device is the lowest. Fig. 4.20 shows the L-I-V characteristics of the three devices in Fig. 4.19 at the heat-sink temperature of 10 K. The increase of the J_{th} can be observed, as expected in the simulation (Fig. 4.7).

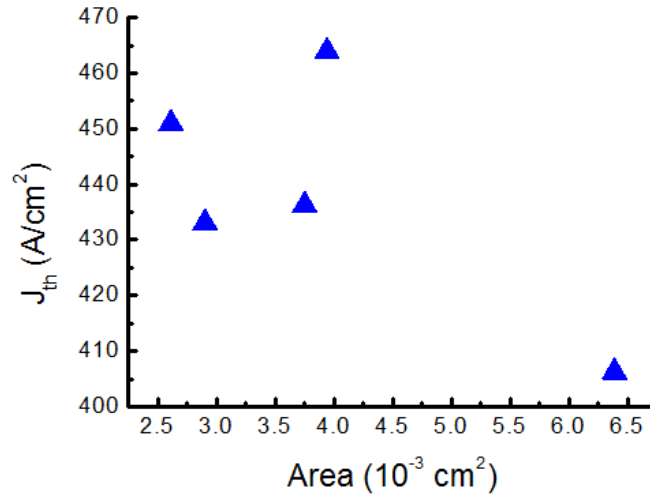


Figure 4.21 Threshold current density as a function of laser area.

Fig. 4.21 presents the threshold current density as a function of the device area. It is shown that the threshold current density decreases with the increase of device area, which agrees with the simulation and discussion in 4.3.2 (Fig. 4.6 and Fig. 4.7).

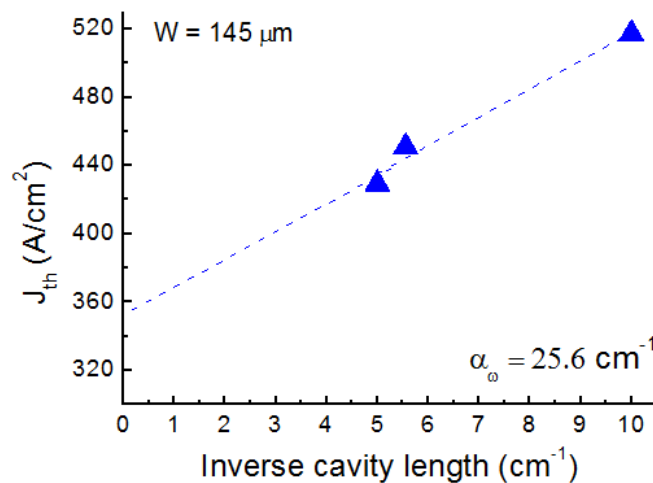


Figure 4.22 Threshold current density as a function of inverse cavity length for devices with 145 μm ridge width and different cavity lengths.

Fig. 4.22 presents a summary of the variation of threshold current densities for lasers with ridge width of 145 μm as a function of inverse cavity length. The data sets are fitted with a linear correlation.

The linear trend can be used to estimate the waveguide loss according to equation (4.3):

$$J_{\text{th}} = \frac{\alpha_w}{g\Gamma} - \frac{1}{L} \frac{\ln R}{g\Gamma} \quad (4.11)$$

where L is the length of the laser ridge and R is the reflection coefficient of the laser facets. A plot of J_{th} against $\frac{1}{L}$ yields $g\Gamma$ and α_w from the gradient and intercept of the linear fitting line.

α_w is estimated and shown in Fig. 4.22. A net modal gain of 0.07 cm/A is extracted from the plot, and the waveguide loss can be estimated as 25.6 cm^{-1} .

4.4.6 Output power dependence on device area

The influence of device area on output power was next investigated. Fig. 4.23 shows the dependence of the peak power on the ridge width of the cleaved device.

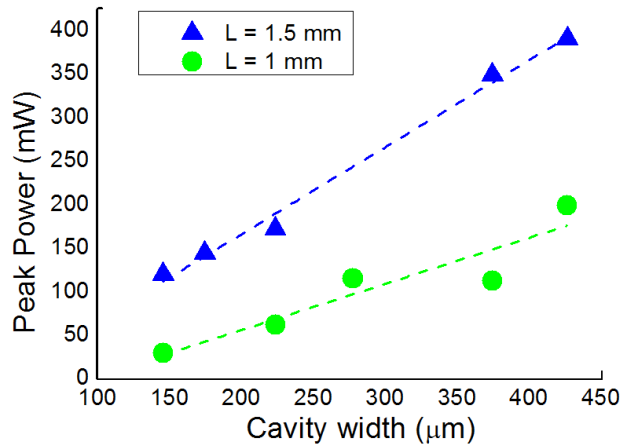
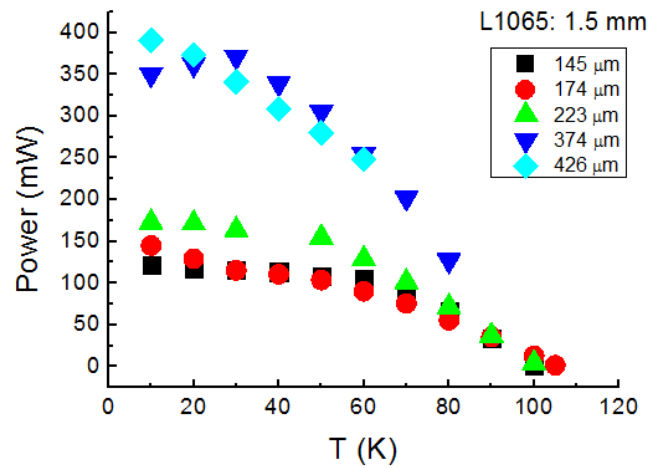


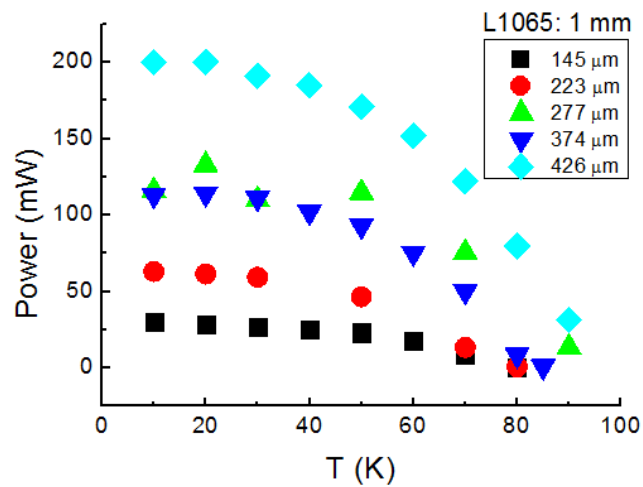
Figure 4.23 Peak power as a function of device ridge width, for devices of length 1 mm and 1.5 mm.

Two sets of devices, with 1.5 mm and 1 mm cavity lengths, were compared. The peak output power increases linearly in power with the cavity width. The longer device showed a higher increase in power with cavity width. For the 1 mm device $\frac{P_{\text{max}}}{W} = 0.53$. For the 1.5 mm device, $\frac{P_{\text{max}}}{W} = 0.98$. This is because

the longer device gives a lower mirror loss, and therefore the heating is less as a consequence of a lower threshold and maximum current for device operation.



(a)



(b)

Figure 4.24 Peak power as a function of heat-sink temperature at different ridge widths (a) cavity length=1.5 mm (b) cavity length=1 mm.

Also, Fig. 4.24 (a) and (b) then show the degradation of power with the increase of heat-sink temperature for devices with 1.5 mm and 1 mm lengths and various ridge widths. For the same heat-sink temperature, there is an obvious decrease of peak power with the decrease of ridge width from 426 μm to 145 μm. It is observed that there is a big change of power between 223 μm and 374 μm. The difference between 223 μm and 374 μm is 151 μm, much larger than the difference between 174 μm and 223 μm. For a device

with a wider ridge width, the power increases as expected, due to the increase of the gain medium.

In Fig. 4.25, the power is shown to depend strongly on the laser length. For the 2 mm device, the peak power at heat-sink temperature of 10 K was 480 mW. For 1 mm device, the peak power was only 113 mW.

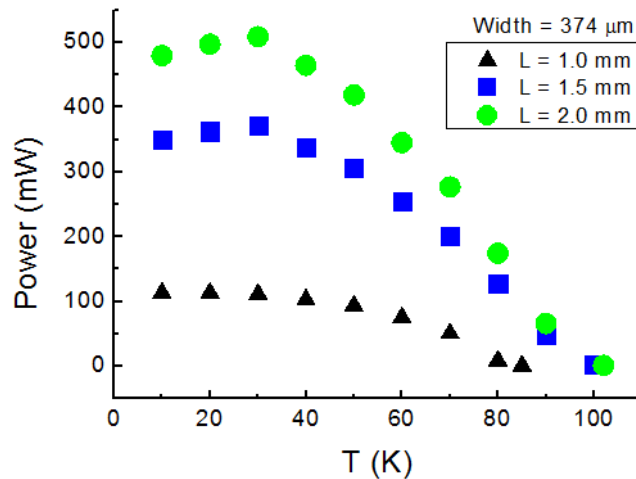


Figure 4.25 Peak power as a function of heat-sink temperature for a cavity width of $374 \mu\text{m}$.

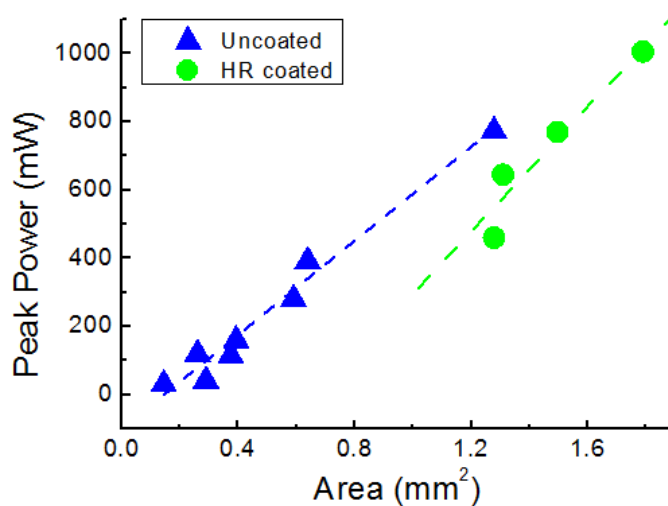


Figure 4.26 Peak power as a function of device area.

Fig. 4.26 summarizes the dependence of the peak power on the area of the cleaved devices at the heat-sink temperature of 10 K. The blue data and linear fitting line represent the result from devices without high reflection coating, and the green data represents the result from HR coated devices.

Both results showed that the peak power increases linearly with the area of the device. The HR coated devices also show a higher rate of increase, possibly due to the decrease of mirror loss and consequently the heating, according to equations (4.3) and (4.5).

4.4.7 Maximum operating temperature dependence on device area

The temperature dependence of the threshold current can be explained by the exponential function as shown in equation (4.12),

$$J_{th} = J_0 \exp\left(\frac{T}{T_0}\right) \quad (4.12)$$

where T is the heat-sink temperature and T_0 is the characteristic temperature with a fitting parameter, J_0 .

The maximum operating temperature can be explained by

$$T_{max} = T_0 \left[\ln\left(\frac{T_0}{J_0 V_{th} R_{th} A}\right) - 1 \right] \quad (4.13)$$

Therefore, for higher maximum operating temperature, lower R_{th} and J_0 are required. There is also a strong dependence of T_{max} on T_0 .

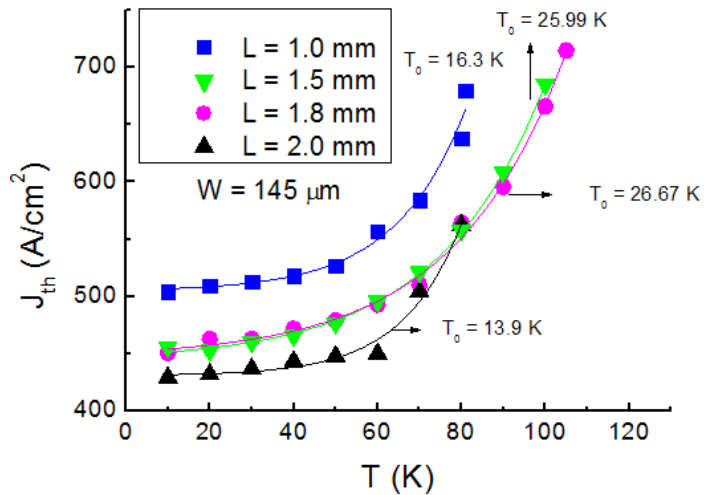


Figure 4.27 Threshold current density as a function of heat-sink temperature for different laser cavity lengths, ridge width=145 μm .

Fig. 4.27 shows the exponential fitting curves for data shown in Fig. 4.18. The data are obtained from devices with 145 μm ridge width, and with the cavity lengths 1 mm, 1.5 mm, 1.8 mm and 2 mm. Based on equation (4.12), the value of T_0 can be obtained from the experimental data to be 16 K, 26 K,

27 K and 14 K for 1.0 mm, 1.5 mm, 1.8 mm and 2.0 mm long lasers, respectively. It is observed that the maximum operating temperature increases with the laser cavity length for 1.0 mm, 1.5 mm and 1.8 mm devices, however, there is an exception for the 2.0 mm device which shows decrease in T_0 as well as the T_{max} . The possible reason for the 2.0 mm long device having a lower T_{max} can be the slight imperfection of the facet cleaving, the possible defects on the device or other damages that could happen during the processing and measurements.

Fig. 4.28 also shows that the maximum operating temperature increased when T_0 has a larger value. The data has been extracted from Fig. 4.27. Typically, for a 1.8 mm with 145 μm width laser, the T_{max} was 109 K with T_0 being 26.7 K. However, it is also not very clear that whether there is a strong dependence of T_{max} on the cavity length.

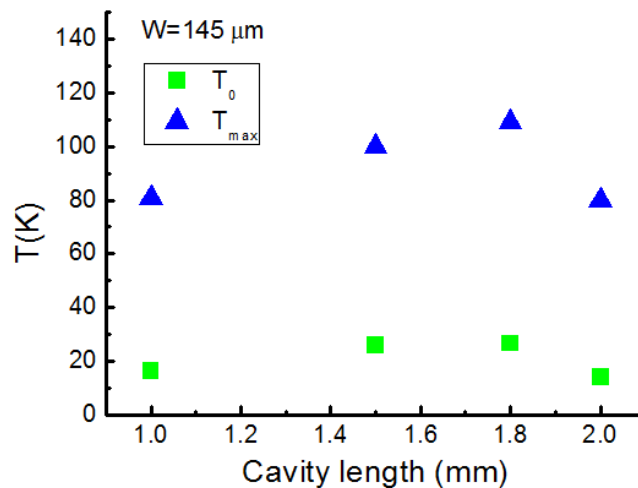


Figure 4.28 Maximum operating temperature and T_0 as a function of laser cavity length.

To investigate further the influence of the device on the maximum operating temperature, more devices were measured and results analysed. Fig. 4.29 shows T_{max} as a function of device area. All devices are measured in pulse mode with 2% duty cycle. The data points represent the experimental data while the blue and green lines represent the approximate linear fittings of the data from uncoated and coated devices. It is observed that T_{max} increases with the device area for both HR coated and uncoated devices, generally. However, more data for HR coated devices may give a clearer conclusion.

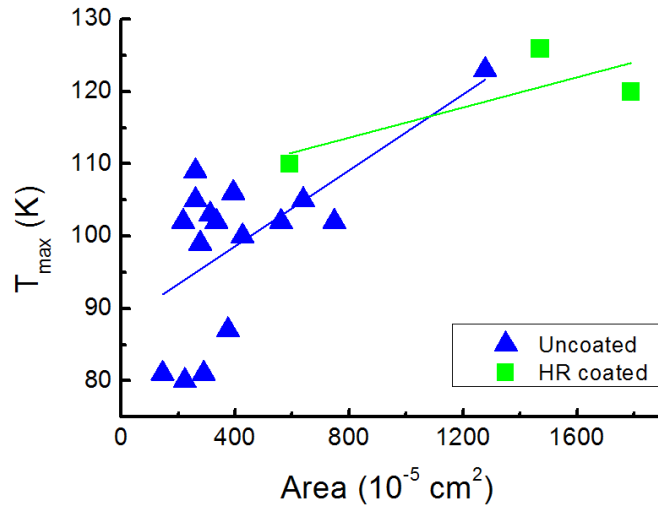


Figure 4.29 Maximum operating temperature as a function of device area.

4.5 Summary

This chapter introduced the development and application of high power THz QCLs, and presents two-dimensional simulation and experimental results on high power THz QCLs. Experimental approaches for improving power performance are discussed and the optimum laser parameters for fabrication have been understood. Using a broad area device has been shown to increase the output power significantly; a total peak power of 1.01 W was achieved from a HR coated device with a ridge width of 426 μm and a cavity length of 4.2 mm, which has been the highest power so far. This work has been published in [53] [72-75].

Chapter 5

Optimization of BTC and hybrid THz QCLs

5.1 Introduction

This chapter reviews the previous research on the improvement of THz QCL performances and investigates the optimization on different BTC and hybrid THz QCL structures. The experimental results of the influence of injector doping level and the background impurity level are presented and analysed theoretically. The pulsed operation as well as the CW operation are studied and the analysis on the optimization of temperature performance is illustrated.

5.1.1 Historical review

The losses in THz QCL devices arise from many factors including free-carrier absorption, impurity scattering, interface roughness, electron-electron scattering, electron-phonon scattering, waveguide losses, and mirror losses. [94] At the extremely low doping concentration in a THz QCL, the losses are dominated by the gold layers in the waveguide and the thin n+ contact layers, but not by the free-carrier absorption in the active region. [95] A higher injector doping leads to a higher current to establish the field required for operation of THz QCLs, which results in a higher threshold current, and free carrier absorption becomes the main loss. [95] For longer wavelength, the effect of free carrier absorption is more important.

The effect of doping concentration within the active region on laser performance has been investigated for both THz QCLs and GaAs and InP based QCLs emitting near 9 μm . [95-101] Most of the previous work reports an increased dynamic range of QCLs with higher doping. For long wavelength QCLs, the waveguide losses are mostly defined by free-carrier absorption. These along with the effect of thermal backfilling define the observed dependence of QCL performance on the injector doping level. Although the optimized doping level is expected to depend on the actual QCL design and the operation wavelength, injector doping dependence has not been addressed in the case of short-wavelength QCLs, where the effect of free-carrier absorption on the waveguide losses is small. [103] A broad range of doping levels, $2.8 - 7.6 \times 10^{15} \text{ cm}^{-2}$ was studied by Ajili et al. in a 3.45 THz BTC active region. A linear dependence was observed between threshold current density J_{th} and injector doping concentration. The

increased doping level also resulted in a red shift of the THz emission frequency due to the active region design. [94] Liu et al. investigated doping characteristics in a 3.2 THz LO-phonon QCL delta doped with a doping gradient in the same sample between $6.0 - 6.9 \times 10^{15} \text{ cm}^{-2}$. The threshold current density J_{th} showed an increasing, but nonlinear correlation with doping density, as expected for free-carrier absorption. [94] It was also reported that the reduced free-carrier absorption in the active region reduced the waveguide losses. [94]

In this chapter, the doping effects on THz QCL performance are investigated further. The influences of injector doping level and background doping level during MBE growth are studied, based on THz QCLs with different active region structures.

5.1.2 Fabrication and measurement

All THz QCL wafers were grown by MBE system on 2-inch SI DSP GaAs substrates. All lasers were fabricated into SISP waveguide devices with 150 μm wide ridges. The laser ridges were defined by wet etching ($\text{H}_2\text{SO}_4: \text{H}_2\text{O}_2: \text{H}_2\text{O}=1:8:40$). The over-layer and backside of the laser were metalized by Ti/Au. The final thickness of the whole device was 200 μm . Laser bars were cleaved from the processed wafers and indium-soldered epilayer-up on Au-plated copper blocks. The facets were left uncoated. After wire bonding, the devices were mounted on a temperature-controlled cold finger of a cryostat. Electrical and optical characteristics of the fabricated laser devices with different injector doping levels were measured at cryogenic heat-sink temperatures above 10 K.

The lasers were measured in both pulsed mode with a repetition rate of 10 KHz with duty cycle of 2% and CW mode at different temperatures. The spectra were measured by FTIR.

5.2 Injector doping

5.2.1 Theoretical analysis

Incorporated impurities influence the electrical and optoelectronic properties of devices. The injector doping level determines the number of available carriers inside the active region, so it is a crucial factor for the QCL performance. A large number of carriers in the upper laser state allow for a

strong population inversion and a high gain, resulting in a high threshold and output power. Simultaneously, however, free-carrier absorption is increased, which scales with n^2 . [95]

For a QCL, the total optical loss is $\alpha = \alpha_w + \alpha_m$, where the mirror loss is $\alpha_m = \ln R/L$, and the reflection index R is determined by the QCL structure and the waveguide design. The waveguide loss is $\alpha_w = \alpha_w^{\text{undoped}} + \Gamma\alpha_w^{\text{abs}}$, which contains the losses of the undoped waveguide structure $\alpha_w^{\text{undoped}}$ and the calculated free carrier absorption $\Gamma\alpha_w^{\text{abs}}$. The dynamic range of the laser is determined subsequently by the doping concentration. Precise judgement of doping levels is essential. The performance of a QCL device results from a compromise between the high output power and the small current consumption necessary for continuous wave operation. [101]

Following reference [102], the expression for maximum current density J_{max} can be written as:

$$J_{\text{max}} = n_s e / \tau \quad (5.1)$$

where n_s is the sheet density of active region doping, e is the electron charge and τ is the global transit time of the electron across one period of the active region. [47]

Following Fig. 5.1, the normalized lifetime τ^* is determined by:

$$\tau^* = \frac{\tau_4}{\tau} \quad (5.2)$$

where τ_4 is the upper level life-time.

The gain coefficient is determined by the following equation,

$$g = \tau^* \left(1 - \frac{\tau_3}{\tau_{43}}\right) \frac{2\pi e z^2}{\lambda \epsilon_0 n_{\text{eff}} L \gamma} \quad (5.3)$$

Where τ^* is the normalized upper state lifetime, τ_3 is the lower level lifetime, τ_{43} is the intersubband optical-phonon-limited relaxation time, z is the optical matrix element between the upper and lower radiative states, λ is the wavelength in vacuum, ϵ_0 is the vacuum dielectric constant, n_{eff} is the effective mode index of the waveguide, e is the elementary charge, L is the length of one period of the active region, and γ is the broadening of the optical transition. [37]

An increase of the transit time τ will result in a decrease of effective upper state lifetime τ^* , and accordingly a decrease in the gain coefficient g of the laser. Since QCLs work up to a temperature where J_{th} and J_{max} become equal [2], the decrease of gain coefficient g will lead to the decrease of T_{max} .

5.2.2 Active regions

Injector doping influences on THz QCL performances have been studied on different structures. Samples with identical growth parameters, but different injector doping levels, were grown, fabricated and characterised. All wafers were grown by MBE based on GaAs/AlGaAs material system with a systematically varied active region doping levels.

The first active region structure is based on a BTC transition with a single-quantum-well phonon extraction/injection stage, with the emission frequency at around 3.1 THz. [47]

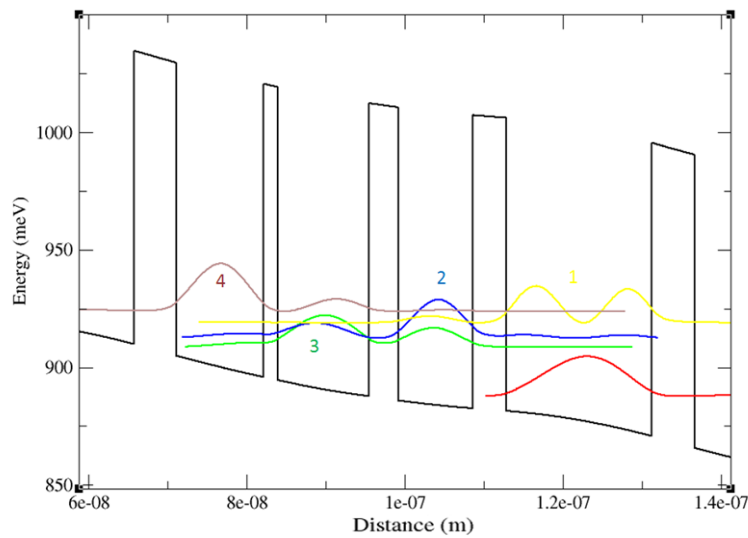


Figure 5.1 Conduction-band diagram and electron subband wave functions squared calculated self-consistently using Schrödinger–Poisson solver of one period of the BTC THz QCL structure, with a single-quantum-well phonon extraction/injection stage under an applied electric field of 7.01 V. The layer sequence of one period of structure, in nanometers, right to left and starting from the injection barrier is **5.5/11.0/1.8/11.5/3.8/9.4/4.2/18.4**, where $\text{Al}_{0.15}\text{Ga}_{0.85}\text{As}$ layers are in bold, and the doped layer is underlined. [47]

As shown in the computed band structure in Fig. 5.1. The doping levels for devices with this structure varied from 2×10^{16} to $6.76 \times 10^{16} \text{ cm}^{-3}$. The reason for choosing this active region design is due to its exceptional temperature performance, as well as a reasonably low threshold and high output power, as explained in reference [47].

A 3.5 THz QCL structure was also studied. The active region is based on the structure reported in [106] (Fig. 5.2), which is a traditional BTC structure. In

this structure, the radiative transition occurs between level $n=8$, isolated in the mini-gap, and a group of three states $n=7, 6$, and 5 in the lower mini-band. Because of the diagonal feature of this laser transition, the total oscillator strength of the radiative transition is significantly low.

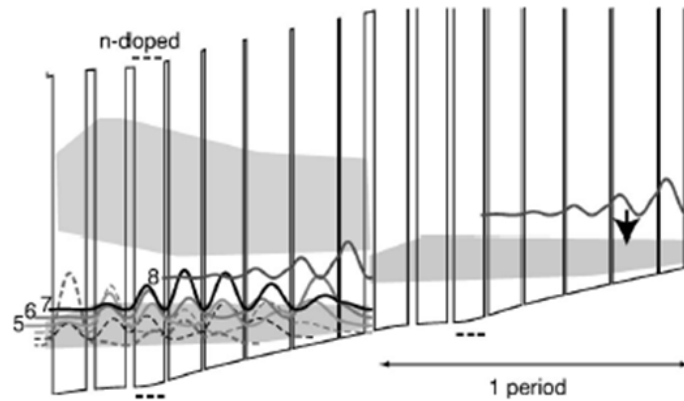


Figure 5.2 Schematic conduction band diagram of one stage of the structure under an average applied electric field of 2.55 KV/cm. The GaAs/ $\text{Al}_{0.15}\text{Ga}_{0.85}\text{As}$ layer sequence of one period of active layers starting from injector barrier is as follows: **3.5/9.0/0.6/16.3/0.9/16.0/1.0/13.8/1.2/12.0/1.5/11.0/2.4/11.0/3.2/12.1**. Thicknesses are in nanometres, GaAs wells are in regular, $\text{Al}_{0.15}\text{Ga}_{0.85}\text{As}$ barriers in bold, and the doped layer is underlined, taken from Ref. [106].

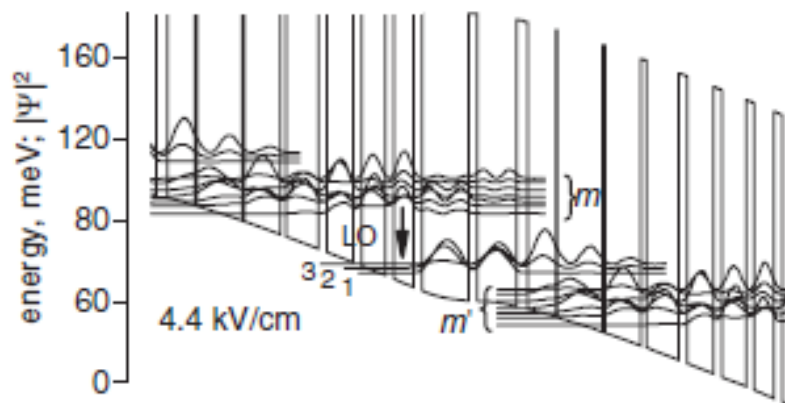


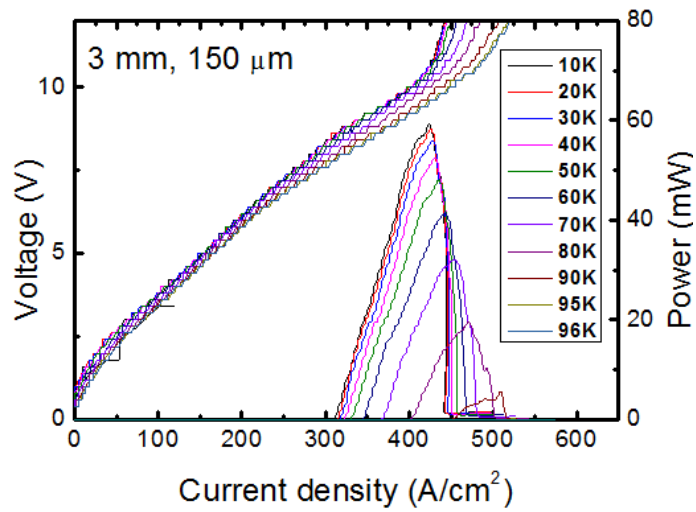
Figure 5.3 Schematic conduction band diagram of two stages of the structure under an applied electric field of 4.4 KV/cm. Layer sequence in nm is as follows: 10.1/**0.5**/16.2/1/12.9/**2**/11.8/**3**/9.5/**3**/8.6/**3**/7.1/**3**/17/**3**/14.5/**4**, (underlined layer is Si doped, figures in bold type are $\text{Al}_{0.15}\text{Ga}_{0.85}\text{As}$ layers), taken from Ref. [46].

Another hybrid design that has been studied is shown in Fig. 5.3. This structure is based on a nine-well design, forming a cascade of alternating

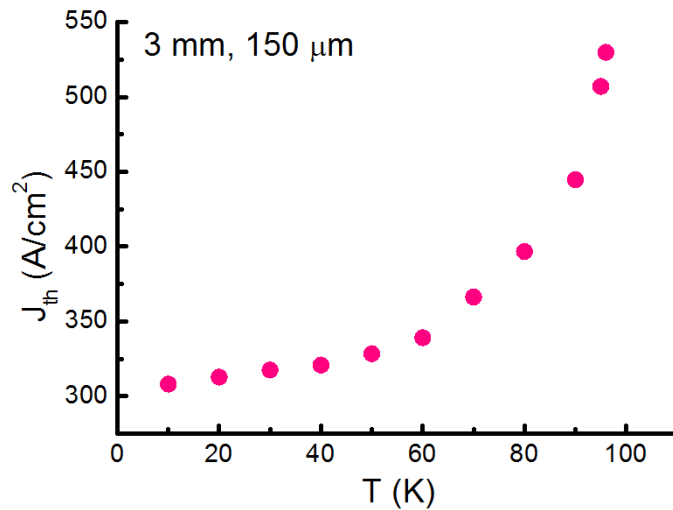
photon and LO-phonon-assisted transitions between two quasi-minibands, emitting at 3.1 THz. [46]

5.2.3 Hybrid structure

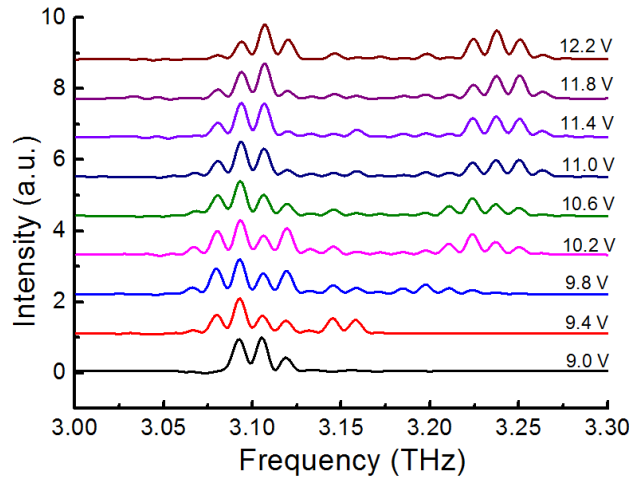
L916 is a typical wafer of the 3.1 THz hybrid structure (Fig. 5.1) [47] doped at $4 \times 10^{16} \text{ cm}^{-3}$. Fig. 5.4 (a) shows the temperature-dependent light as a function of current density of a device with 3 mm length and 150 μm width, measured in pulsed mode.



(a)



(b)



(c)

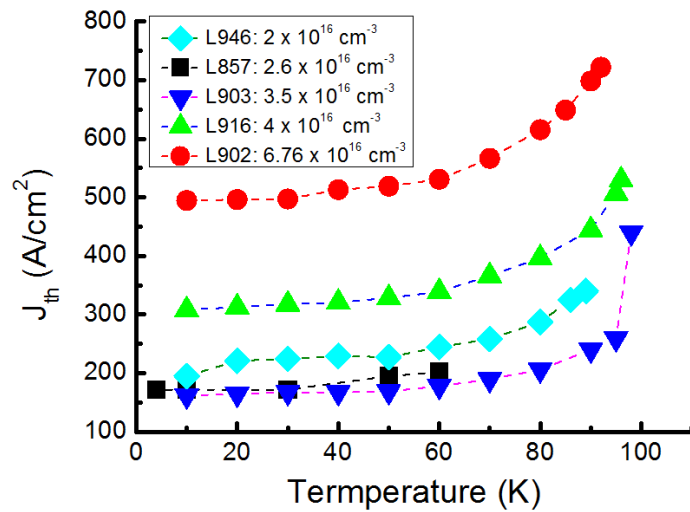
Figure 5.4 Results of L916 with 3 mm length and 150 μm width measured with 2% duty cycle (a) L-I-V characteristics (b) threshold current density as a function of heat-sink temperature (c) spectral characteristic at heat-sink temperature of 10 K.

The laser starts lasing at a threshold current density of 320 A/cm^2 , and a voltage of 8.4 V. The dynamic range is 115 A/cm^2 . The maximum operating temperature is 96 K. Moreover, the device emitted a peak power of 59 mW at the heat-sink temperature of 10 K (Fig. 5.4 (a)). The threshold current density and heat sink temperature have an exponential dependence, as shown in Fig. 5.4 (b). The spectral characteristic of L916 was measured as a function of voltage, as shown in Fig. 5.4 (c). The lasing frequency is between 3.07 THz to 3.25 THz. A peak frequency is located at 3.10 THz, which is in a good agreement with that reported in reference [47]. Both single-mode and multi-mode lasing were observed from different devices. Also, the lasing modes changed from single mode to multi-mode with the increase of the applied voltage.

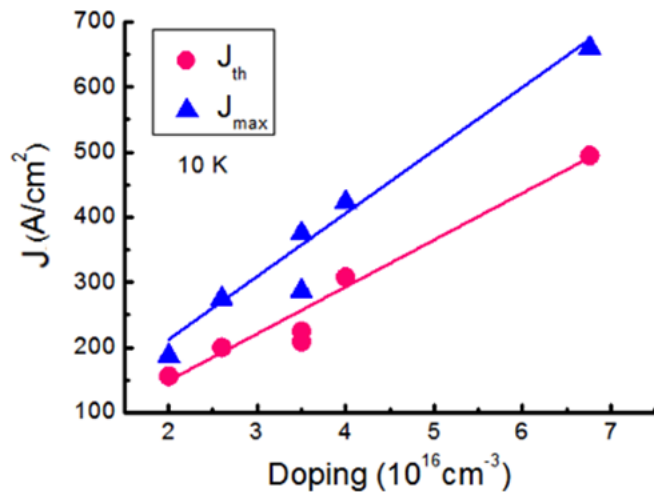
Fig. 5.5 (a) shows the threshold current density as a function of the heat-sink temperature for a group of devices with varied injector doping levels. The device with the lowest injector doping level shows the lowest threshold current density, while J_{th} is the highest for the device with the highest doping level. For each device, J_{th} increases exponentially with heat-sink temperature. Following the discussion in 5.2.1 and equation (4.3), theoretically, the increased injector doping level leads to an increase in the waveguide loss from free carrier absorption $\Gamma\alpha_{\text{w}}^{\text{abs}}$, and consequently J_{th} .

Fig. 5.5 (b) shows the threshold current density J_{th} and the maximum current density J_{max} defined as the current density where the optical power shows a

maximum, as functions of doping concentration, at the heat-sink temperature of 10 K. Both J_{th} and J_{max} increase almost linearly with the injector doping level. As such, the dynamic range of the laser increases with doping concentration. No saturation of J_{th} and J_{max} has been observed within the studied doping range between 2×10^{16} to $6.76 \times 10^{16} \text{ cm}^{-3}$. However, if the injector doping level increases further, saturation would occur due to the increase of waveguide loss and heating.



(a)



(b)

Figure 5.5 (a) Current density as function of heat-sink temperature for devices with different injector doping levels. (b) Current density as a function of doping level, blue symbols represent maximum current density, pink symbols represent threshold current density. The lines are linear fits to the data.

There is an exception in Fig. 5.5 (a), which also includes two devices (wafers L946 and L971) with the same doping level but different J_{th} , due to the growth parameter variation in different growth runs. Overall, Fig. 5.5 (a) and (b) show that the injector doping level affects both J_{th} and J_{max} . An optimum injector doping level needs to be considered to minimize the lasing threshold while maximize the dynamic range and operating temperature.

5.2.4 Other BTC designs

In order to demonstrate the influence of injector doping on laser performance of different THz QCL structures, other THz QCL structures were studied. Similar results of the influence of injector doping were obtained.

Wafer No.	Injector doping level (cm^{-3})	Cavity length (mm)	Ridge width (μm)	T_{max} (pulsed) (K)	J_{th} at 10K (A/cm^2)	P_{max} at 10K (mW)
L1152	2.55×10^{16}	3	150	73	123	9.7
L1152	2.55×10^{16}	1	150	38	171	1
L1171	3.0×10^{16}	3	150	77	180	15
L1171	3.0×10^{16}	1	150	37	250	5.5

Table 5.1 Details of 3.5 THz BTC QCL devices (L1152 and L1171).

Results from wafer L1152 and L1171 with the same BTC structure (Fig. 5.2) [106] are shown in Table 5.1. The doping level for wafer L1171 has been increased by 17.6% compared with L1152, resulting in an increase in the threshold current density of 46.1% for 3 mm devices. The peak power increased by 55.4% for 3 mm devices and 450% for 1 mm device. More comparisons are shown in Fig. 5.6 (a) and Fig. 5.6 (b) for these wafers, L1152 and L1171. Both J_{th} and J_{max} increase with injector doping level at different heat-sink temperatures (Fig. 5.6 (a)), and the dynamic range has been improved for L1171 (Fig. 5.6 (b)). In Fig. 5.6 (b), the NDR region occurs at a similar voltage in these wafers, but at different current densities, depending on doping.

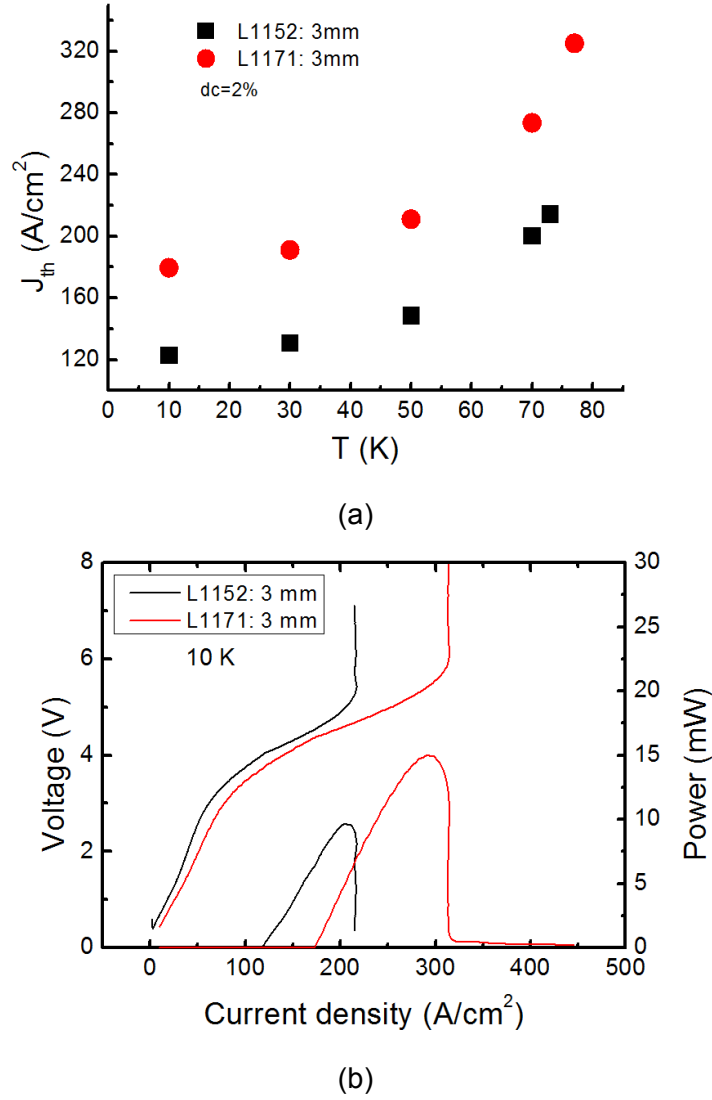


Figure 5.6 (a) Threshold current density as a function of heat-sink temperature for 3 mm L1152 and L1171. (b) L-I-V characteristics at heat-sink temperature of 10 K for 3 mm L1152 and L1171. Devices are measured in pulsed mode. Devices were measured in pulsed mode with 2% duty cycle.

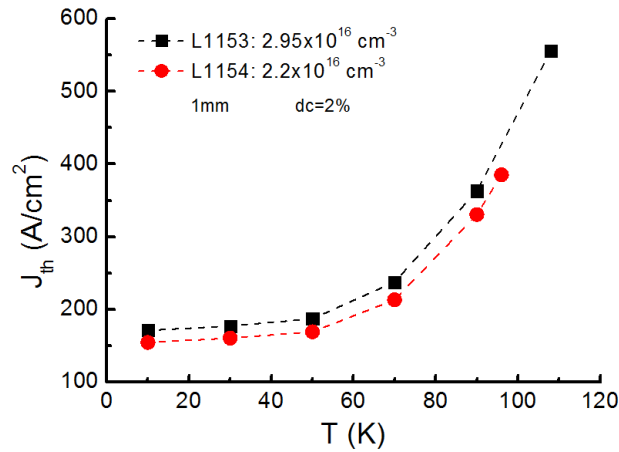
Wafer No.	Active region Structure	Injector doping level (cm ⁻³)	Cavity length (mm)	Ridge width (μm)	T _{max} (pulsed) (K)	P _{max} at 10K (mW)
L1153	Hybrid	2.95 x 10 ¹⁶	3	150	122	90
L1153	Hybrid	2.95 x 10 ¹⁶	1	150	108	43
L1154	Hybrid	2.20 x 10 ¹⁶	3	150	114	84
L1154	Hybrid	2.20 x 10 ¹⁶	1	150	96	28

Table 5.2 Details of 3.1 THz QCL devices (L1153 and L1154).

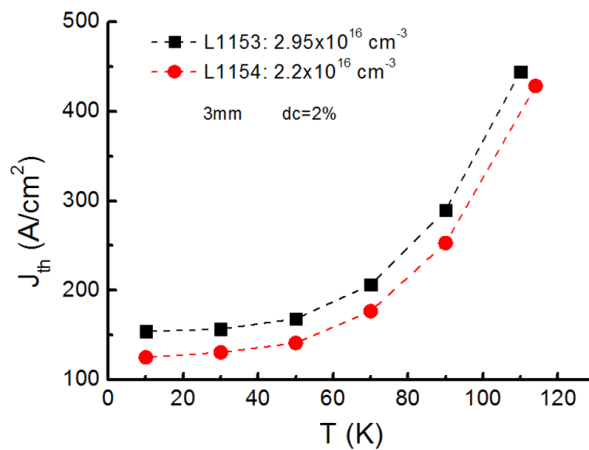
Table 5.2 shows details of wafer L1153 and L1154 with a 9 wells hybrid structure and the designed emission frequency at 3.1 THz [46]. The

schematic band diagram was shown in Fig. 5.3. This structure was designed by Wienold et al. based on LO-phonon-assisted interminiband transitions. [46]

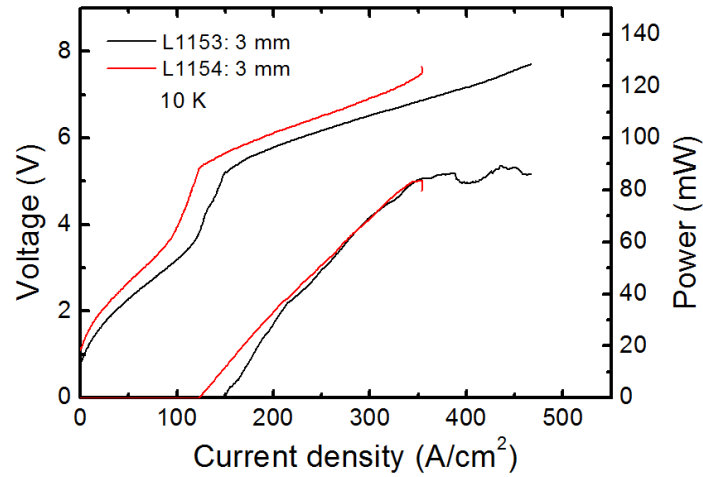
Comparing the pulsed mode measurement results, similar to previous structures, threshold current density increases with the injector doping level for both 1 mm and 3 mm devices (wafer L1153 and L1154), according to Fig. 5.7 (a) and (b). In Fig. 5.7 (c), the L-I-V characteristics of 3 mm L1153 and L1154 are compared. The dynamic range ($J_{\max} - J_{\text{th}}$) of L1153 is 280 A/cm^2 , while ($J_{\max} - J_{\text{th}}$) of L1154 is 225 A/cm^2 . The dynamic range was also improved in L1153. Furthermore, comparing J_{th} between 1 mm and 3 mm devices, for both L1153 and L1154 wafers, as shown in Fig. 5.7 (a) and (b), 1 mm devices have higher J_{th} as expected. This agrees with equation (4.3) and (4.5) in 4.3.1. The mirror loss increases with the decrease of laser cavity length, thus leading to an increase in J_{th} .



(a)



(b)

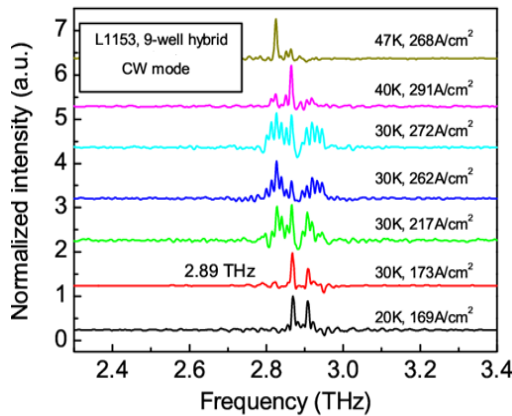


(c)

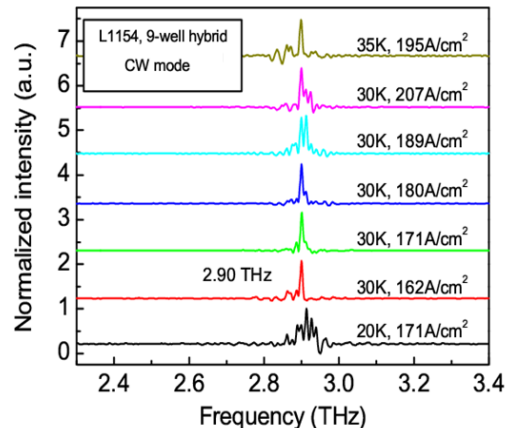
Figure 5.7 (a) Threshold current density as a function of heat-sink temperature for 1 mm L1153 and L1154, (a) threshold current density as a function of heat-sink temperature for 3 mm L1153 and L1154, (b) Length=3 mm, (c) L-I-V characteristics at heat-sink temperature of 10 K for 3 mm L1153 and L1154. Devices are measured in pulsed mode. Devices were measured in pulsed mode with 2% duty cycle.

5.2.5 CW operation

To study further the injector doping influences on THz QCL device performances, the CW mode operation was also investigated with L1153 and L1154. The heat dissipation needs to be minimized in order to achieve CW operation at cryogenic temperatures with reasonable costs. Therefore, this structure with low threshold current densities and operating voltages are desirable. [46]



(a)



(b)

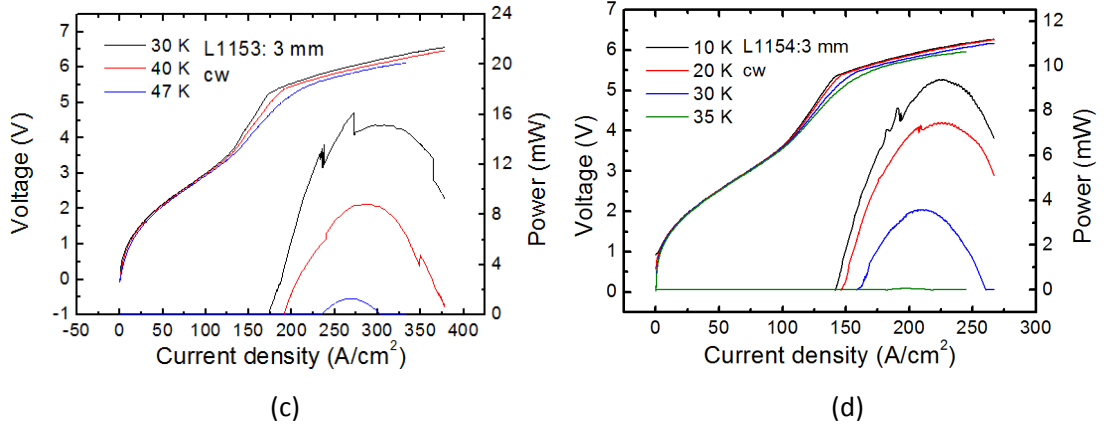
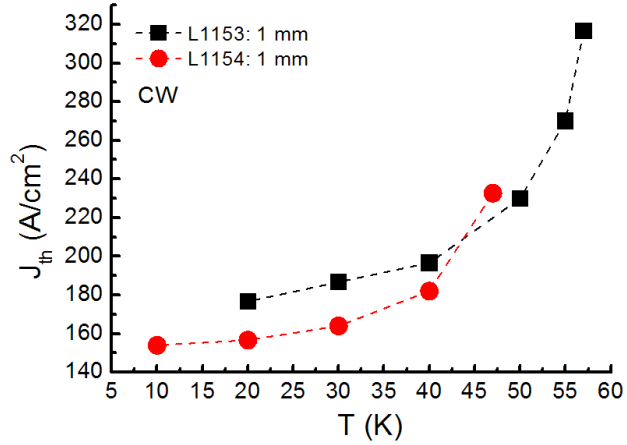


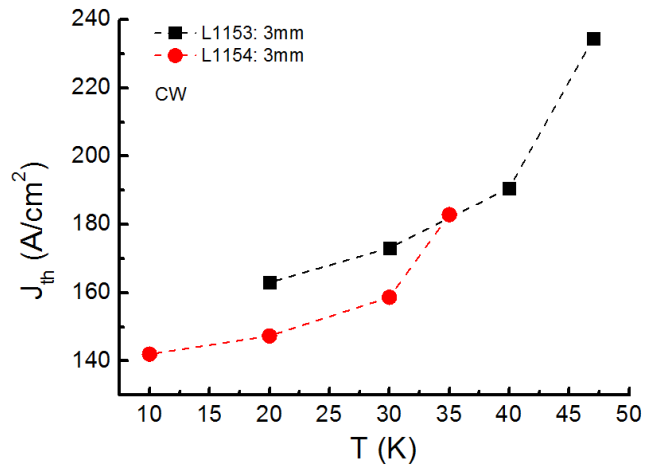
Figure 5.8 CW results of L1153 and L1154 devices, with length=3 mm and, width=150 μm , (a) spectra of L1153 (b) spectra of L1154 (c) L-I-V characteristics of L1153 (d) L-I-V characteristics of L1154.

The L-I-V and spectral characteristics of L1153 and L1154 under CW mode operation are shown in Fig. 5.8. As shown in Fig. 5.8 (a) and (b), lasing emissions are observed between 2.8 to 2.95 THz for 3 mm-long device from wafer L1153, and 2.85 to 2.95 THz for 3 mm-long device from wafer L1154. The central lasing frequency for both devices is at 2.9 THz. Blue shift of the spectra was observed while increasing the current density owing to the Stark effect.

The L-I-V characteristics are shown in Fig. 5.8 (c) and (d). The 3 mm-long L1153 device operated up to 47 K with a peak power of 16 mW at the heat-sink temperature of 30 K. For 3 mm L1154 device, the maximum operating temperature is 35 K with a peak power of 9 mW at 10 K. The heat dissipation was improved by thinning the substrates to 170 μm . Since the injector doping of L1154 is 29.2% lower than L1153, the lasing threshold of L1154 decreased by 9.7% in pulsed mode (Fig. 5.7 (a)) for 1 mm devices, and 18.8% for 3 mm devices (Fig. 5.7 (b)), at heat-sink temperature of 10 K. Whilst in CW mode, at heat-sink temperature of 30 K, the threshold decreased by 12.1% for 1 mm devices (Fig. 5.9 (a)) and 8.1% for 3 mm devices (Fig. 5.9 (b)).



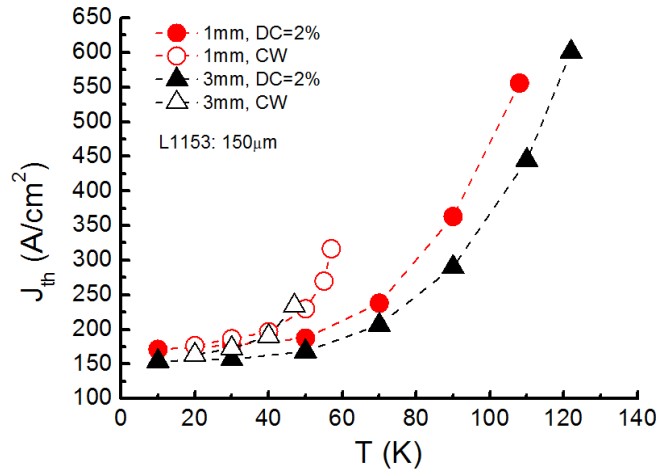
(a)



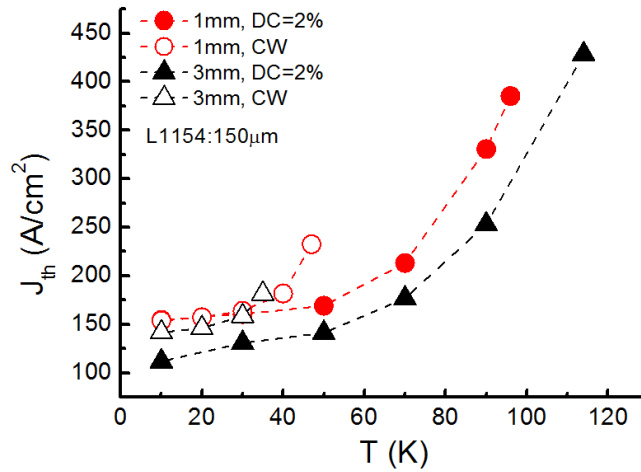
(b)

Figure 5.9 Threshold current density as a function of heat-sink temperature for L1153 and L1154 devices under CW mode, (a) length=1 mm, width=150 μm (b) length=3 mm, width=150 μm .

In CW operation mode, the active region temperature is much higher compared with pulsed mode due to the continuous current flowing through the device. Following equation $J_{th} = J_0 \exp(T_{act}/T_0)$, where T_{act} is the active region temperature. J_{th} increases with T_{act} exponentially. Therefore, J_{th} in CW mode is higher than in pulsed mode. Comparing the results between CW and pulsed measurements, the improvements in threshold are different. For 3 mm-long devices from wafer L1153 and L1154, there is a 20% decrease in J_{th} in pulsed mode, and a 8.1% decrease in CW mode, due to the heating in CW mode.



(a)



(b)

Figure 5.10 Comparison of threshold current density between pulsed and CW results at different heat-sink temperatures, (a) L1153, width=150 μm (b) L1154, width=150 μm.

Fig. 5.10 (a) and (b) summarize results between pulsed and CW measurements for 1 mm-long and 3 mm-long devices from wafers L1153 and L1154. As can be seen, the threshold current density of devices operating in CW mode is higher than the pulsed mode (2% duty cycle). It is observed that both L1153 and L1154 show higher threshold current densities under CW mode compared with the pulsed mode, at the same heat-sink temperatures.

5.2.6 Temperature performance

The performance of our recently-grown hybrid samples [47] (Fig. 5.1) has been analysed further by looking at the influence of doping on the operating temperature.

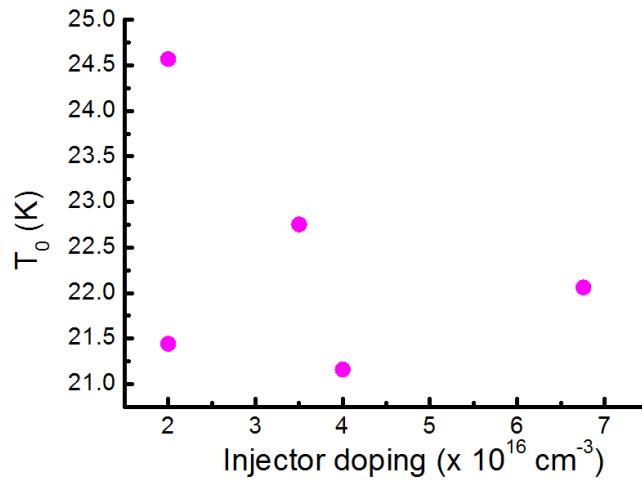
The devices are from wafer L946, L989, L903, L916 and L902, with injector doping level from $2 \times 10^{16} \text{ cm}^{-3}$ to $6.76 \times 10^{16} \text{ cm}^{-3}$. The doping level of each wafer is shown in Table 5.3.

Wafer number	Injector doping level (cm^{-3})
L946	2×10^{16}
L989	2×10^{16}
L903	3.5×10^{16}
L916	4×10^{16}
L902	6.76×10^{16}

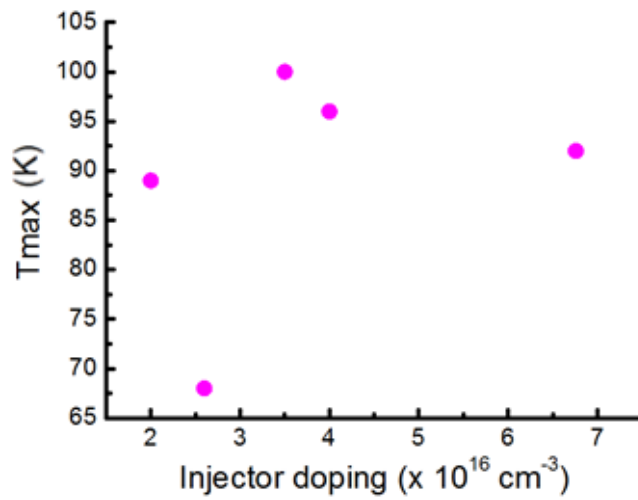
Table 5.3 Hybrid THz QCL wafers with different injector doping levels.

Assuming an exponential variation of the threshold current density with heat-sink temperature, as defined in Equation (4.12), the characteristic temperature T_0 was extrapolated. As shown in Fig. 5.11 (a), the value of T_0 is not dependent on the doping concentration consistently. If the electron backfilling is not negligible, since electrons in the upper subband acquire sufficient energy for emitting an LO-phonon and relaxing to the lower state, the upper state lifetime τ_{21} decreases exponentially based on $\tau_{21}^{-1} \propto \exp[-(E_{LO} - h\nu)/k_B T_e]$, where $h\nu$ is the terahertz photon energy, and k_B is the Boltzmann constant. Therefore, following equation (4.3) and (5.3), the gain coefficient decreases and consequently J_{th} increases. It is implied that electron backfilling of the lower lasing state can be neglected. [83][101]

Fig. 5.11 (b) shows the maximum operating temperature as a function of injector doping level. There is no clear trend between the maximum operating temperature and injector doping level, although the results suggest that samples with a higher doping level have a higher maximum operating temperature.



(a)



(b)

Figure 5.11 (a) Maximum operating temperature as a function of injector doping level, (b) T_0 as a function of injector doping level.

The transit time of devices from (L773, L836, L857, and L866) are compared. All samples have the same hybrid active region structure [47]. The sheet carrier density in the active region of each wafer is shown in Table 5.4. The threshold and maximum current density as a function of the sheet carrier density is shown in Fig. 5.12. The data were measured at the heat-sink temperature of 78 K.

Wafer No.	Sheet carrier density (cm^{-2})
L773	3.68×10^{10}
L836	3.68×10^{10}
L857	4.78×10^{10}
L866	6.44×10^{10}

Table 5.4 Hybrid THz QCL wafers with different sheet carrier densities.

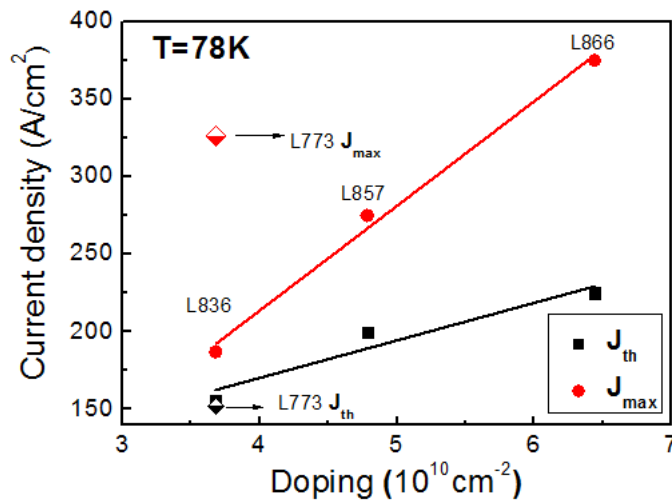


Figure 5.12 Threshold current density (J_{th}) and the maximum current density (J_{max}) at 78 K as a function of sheet carrier density of the active region. Samples were grown in Leeds and DM devices measured by E. Strupiechonski, Y. Halioua, G. Xu, R. Colombelli et al. in Universite Paris-sud 11.

Following Fig. 5.12 and equation (5.1), the obtained transit time in one period of the active region is 31.5 ps, 27.8 ps and 27.5 ps (device L836, L857, L866) as shown in Fig. 5.13. The value of τ is larger than the reference [47] which is 19 ps. Therefore, since the larger transit time will result in more scattering, device performance of the device deteriorates. This can be a possible reason why the maximum operating temperature is lower than the reported result [47].

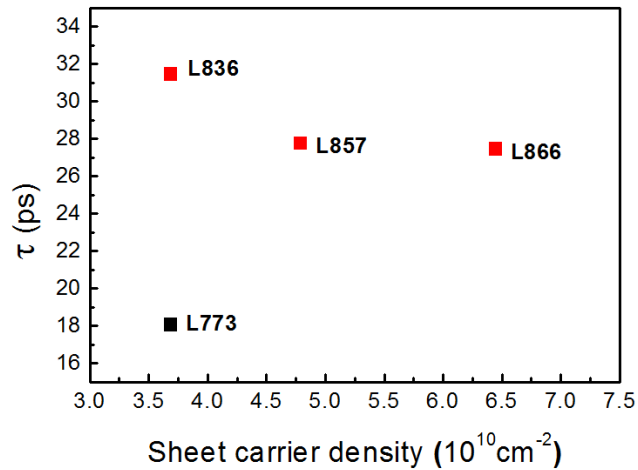


Figure 5.13 Transit time as a function of sheet carrier density.

5.3 Background doping

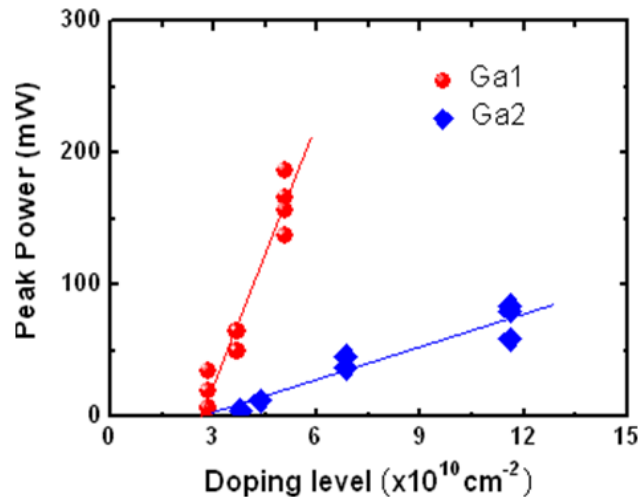
To improve sample quality by MBE growth, the background impurity level needs to be reduced. Several mobility-limiting impurities found in MBE-grown GaAs and AlGaAs have been identified, including carbon, oxygen, sulphur and silicon. [104] Charged impurities in the GaAs lattice are significant sources of mobility-limiting scattering. [104] Unintentional charged impurities can come from a number of sources, including the background vacuum, hot metal surfaces within the growth chamber, the starting GaAs substrate, and the starting elemental materials used for semiconductor growth. [104] For THz QCL devices, it has been argued previously that the level of impurities will influence the scattering and unintentional tunnelling within the device, as well as affecting the lifetimes of the laser levels and the electron injection efficiency [105]. It is not easy to evaluate quantitatively the microscopic mechanism occurring in THz QCLs, especially the influence of lifetimes on the lasing. However, the global transit time of the electron across a period of the active region at resonance can be experimentally determined from J_{max} . [47, 93] Therefore, in addition to calibrating the precise thicknesses or compositions of the layers during THz QCL growth, and achieving growth reproducibility, it is also essential that materials grown be of the highest quality, with low levels of background impurities.

In our work, unintentionally doped bulk GaAs layers were used as a technique for assessing the background quality of the MBE system. Typically, a 15 μm -thick unintentionally doped GaAs layer is grown on a 2-inch Si

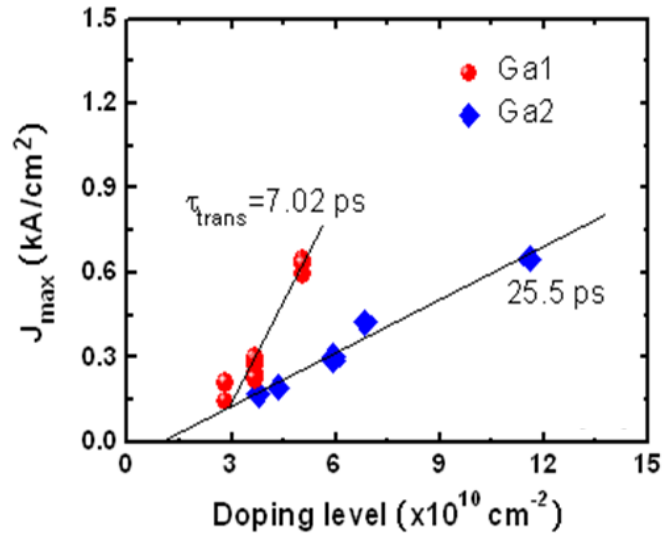
GaAs substrate, and the background doping level is measured by VDP Hall method, which has been explained in Chapter 2 (2.4.1).

In contrast, Beere et al. have used the <4 K mobility of high electron mobility transistors as a gauge to evaluate the material quality, and have correlated this with the QCL device performance [105], observing that the higher the electron mobility, the better the performance. This technique does, however, require access to low temperature characterisation equipment, and the low temperature performance of HEMTs is itself strongly dependent both on the device structure and growth conditions. Whether this, or the more straightforward assessment of bulk GaAs, is the better way for setting up an MBE system for QCL growth remains to be determined, but it is clear that some technique is needed to maximize the yield of high-performance QCL wafers. [107]

Fig. 5.14 (a) and (b) show the dependency of output power and J_{\max} on the injector doping level, with data reported from two sets of samples grown with different Ga cells (Ga1 and Ga2). The structure of all samples in Fig. 5.14 is the hybrid THz QCL design [47] (Fig. 5.1). The devices are measured in pulsed mode with 2% duty cycle. For both sets of samples, the device optical output power and J_{\max} scales almost linearly with the increase of injector doping level (Fig. 5.14 (a)), similar to the trends observed in section 5.2.



(a)



(b)

Figure 5.14 Variation of (a) peak output power and (b) J_{max} with injector doping level. The active region is based on hybrid design in [47]. Two Ga cells (Ga1, Ga2) were used for these growths. Ga1 had high purity, Ga2 was known to be contaminated and hence the GaAs was compensated and of low quality. The total unintentional doping from both cells was, however, $< 2 \times 10^{14} \text{ cm}^{-3}$, – rather less than the intended injection level doping levels.

There is, however, a marked difference between the performance of THz QCLs grown with Ga1 and Ga2, and this arises from the quality of material produced by the two cells. Ga1 produced high quality material, with low background impurity levels, whilst Ga2 was known to be contaminated, growing highly compensated material. For samples grown with Ga2, there was only a small increase in output power with active region doping, such that with n_s of $\sim 1.1 \times 10^{11} \text{ cm}^{-2}$, the output power was only $\sim 60 \text{ mW}$. On the other hand, for samples grown with Ga1, even with $n_s \sim 5 \times 10^{10} \text{ cm}^{-2}$, output powers of up to 180 mW could easily be achieved. This trend was not only observed for this hybrid design, but also all other QCL active region designs investigated.

The dynamic range is much narrower for laser grown with a higher background doping level, as shown in Fig. 5.15, comparing two lasers with the same resonant-phonon design [20]. Fig. 5.16 shows the peak output power of the lasers grown at different background doping levels, and at different heat-sink temperatures. For each measured heat-sink temperature, the peak output power for higher background is lower. Moreover, the maximum operating temperature is higher for the wafer grown at lower

background doping level. The above results suggest that the background doping does significantly affect the temperature performance of THz QCLs.

In order to achieve better THz QCL performance, therefore the background doping level in a MBE system is required to be minimized.

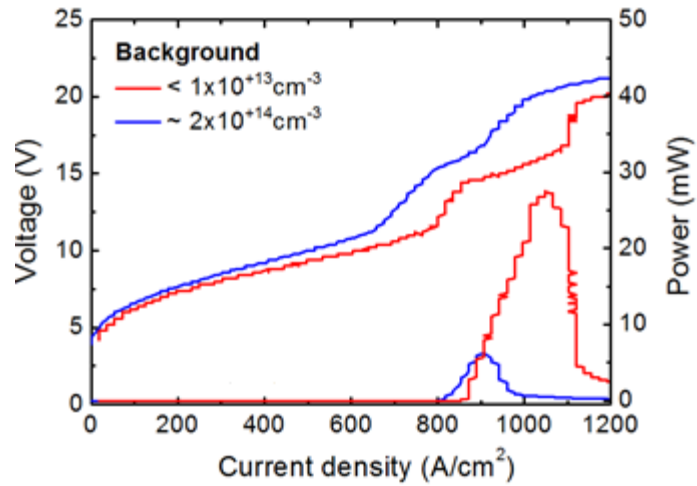


Figure 5.15 L-I-V characteristic at the heat-sink temperature of 10 K for two lasers grown at different background doping levels.

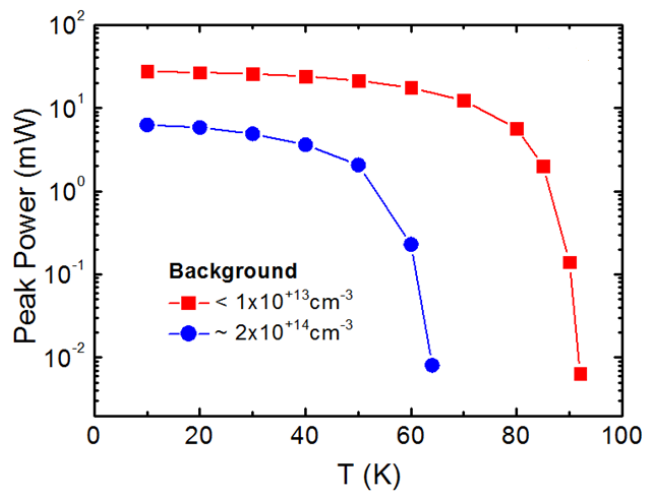


Figure 5.16 Peak power as a function of heat-sink temperature under two background doping levels: $1 \times 10^{13} \text{ cm}^{-3}$, and $2 \times 10^{14} \text{ cm}^{-3}$.

5.4 Summary

Various factors that influence THz QCL performance have been discussed in this chapter. The injector doping concentration of THz-QCLs with different active regions has been varied in order to study doping effects. The J_{th} and J_{max} scale linearly with the doping concentration since a THz QCL needs a certain field for lasing. If the doping is higher also the current has to be higher to establish that field. The output power increases monotonically with doping. [95]

Experimental results show that in order to achieve better output power and higher maximum operating temperature, better material quality is required during the wafer growth, and the optimum injector doping level should be considered for obtaining lower threshold current density and larger dynamic range.

Other important performance characteristics, such as peak optical output power and maximum operating temperature, can be improved by optimizing injector doping level, lowering background impurity level during MBE growth.

This work has also been published in [75] and [79].

Chapter 6

THz QCLs on misorientated substrates

6.1 Historical review on misorientation

6.1.1 Interface roughness

It has been reported that the structural integrity of the (100) GaAs wafer influences the electrical and optical properties of semiconductor devices grown on this surface. [108] For example, a rough surface degrades the mobility of two-dimensional electron gases, the luminescence line-widths of AlGaAs/GaAs/AlGaAs QWs, and the peak current densities of resonant tunnelling diodes, as well as increasing the optical scattering losses of QW laser diodes. [55]

The mechanisms and possible reasons of interface roughness have been researched by different groups. The surface morphology is closely related to the substrate orientation, film thickness, film composition, dopant type and doping concentration. The dopant diffusion in a heavily doped GaAs layer may lead to the degradation of the morphology of the epitaxial layers. [109] For AlGaAs/GaAs hetero-structures, the presence of background impurities on the growth surface can reduce the surface diffusion length of gallium and aluminium, and also some impurities, such as C, can disrupt lateral atomic propagation on the surface, thereby resulting in increased interface and surface roughness. [110] The quality of AlGaAs can strongly influence the AlGaAs/GaAs interface properties, since the surface migration rate of Al is low and the segregation rate of impurities is high in AlGaAs. [110] The surface becomes rougher with the increase of Al composition in an $\text{Al}_x\text{Ga}_{1-x}\text{As}$ layer, especially for $x=15\%–45\%$ [109]. The increase of oxygen incorporation into a GaAs layer may also reduce the surface smoothness of a GaAs/AlGaAs heterostructure. [3] The growth temperature is also a critical factor. When the substrate is grown between 630~690 °C, As deficiencies can occur at the sample surface, due to inefficient cracking of As_4 into As_2 , and produce a rough surface. For growth rates of 1-2 $\mu\text{m}/\text{hour}$ at a growth temperature below ≈ 700 °C, the low-surface mobility of Al atoms is the cause of the roughness. [108]

6.1.2 Effects of misorientation

There are many ways to improve the interface properties in an AlAs/GaAs material system. Examples are using purer sources [110], growing QW SPLs on top of AlGaAs to trap the impurities [108], adding GaAs layers regularly in AlAs and misorientating the substrate toward (111) A. [110] One of the disadvantages of growing GaAs/AlGaAs layers on the (100) substrate is the rippled surface morphology. [55] It has been demonstrated by many researchers that misorientation of (100) GaAs can improve the interface morphology during MBE growth. The reason is that the orientation of the substrate strongly affects the incorporation of impurities and deep levels in the epilayer. It has also been shown that the misorientation approach can reduce the impurity incorporation rate. [110-111] This is possibly due to the reduction of kink density from the edges of terraces when the substrate is misorientated. It can be more difficult for impurities to settle on the surface, and so the surfaces are of higher purity compared with (100) GaAs wafers. [55][112] It has also been found that the direction of the misorientation influences both the static and dynamic nature of the surface steps, due to the alteration of the growth mechanisms. Since the GaAs quality is improved from the misorientation, the 2DEG transport properties can be improved in modulation-doped QW structures. [111]

Previous papers have suggested different angles that produce the best device performance. For example, the optimum misorientation angle of 4° towards (111) A was observed during a mobility study of the 2DEG in modulation-doped structures. However, the smoothest morphology has been reported to be 6° off (100) towards (111) A. The background impurity incorporation rate was reported to be reduced by misorientating substrates of $3-4^\circ$ toward the (111) A surface. [55] It was also suggested that the optimum substrate misorientation angle might depend on different growth conditions. [111]

6.1.3 Chapter outline

Based on previous research, in which the wafer surface condition changes with misorientation angles, it is highly possible that the performance of THz QCL lasers can be improved by misorientating GaAs wafers with critical angles, and using them as the substrates for THz QCLs. In this chapter, the effects of misorientation on THz QCLs are studied experimentally. Two QCL active regions, a BTC and a hybrid structure which are illustrated in 6.3 and

6.4 are examined, in order to find out whether there is any significant effect caused by any variation in the active region structure. Devices with different lengths are measured and compared. The investigated properties include maximum operating temperature, threshold current density, dynamic range, and peak optical power.

6.2 Misorientation and growth mechanism

6.2.1 Introduction

The orientation of a crystallite is determined by a transformation from one reference frame to the local reference frame of the lattice. Misorientation is the shift from one local crystal frame to a different frame. It is defined as the difference in crystallographic orientation between two crystallites in a polycrystalline material. The schematic diagram of the misorientation is shown in Fig. 6.1, where there is a 4° misorientation from the nominal plane. [113]

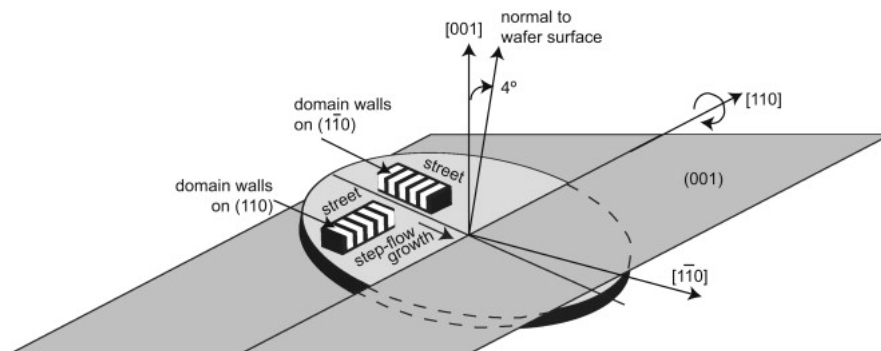


Figure 6.1 A schematic diagram of misorientation. [113]

The growth mechanism involved in GaAs/AlGaAs heterostructure growth is called 'step-flow growth'. The step-flow growth mode comprises a flux of atoms impinging on the substrate surface, followed by the chemisorption and diffusion of the atoms across terraces on the surface. When a step is reached during the growth, some atoms can be desorbed back into the gas phase. Growth proceeds monolayer by monolayer and all steps flow across the surface while in steady state. [114] A simplified step-flow diagram is given in Fig. 6.2, showing a perfectly ordered surface with the steps straight and equally spaced. The common stepped surfaces include a meander formed by individual steps, and step bunches separated by large terraces. [114]

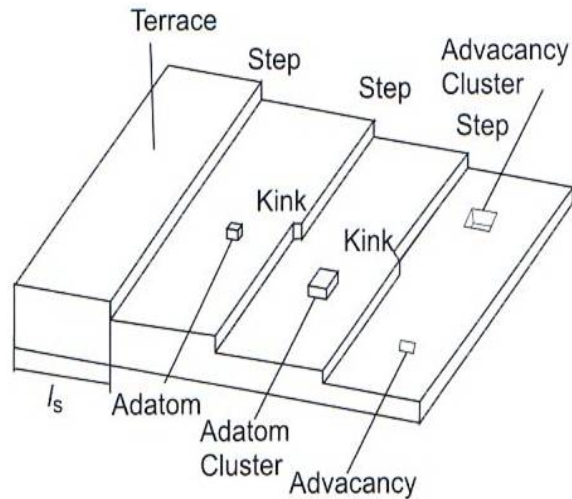


Figure 6.2 A schematic diagram of step-flow growth.

In the case of a THz QCL wafer, thousands of layers are grown during the entire growth process. The interface quality becomes very critical and strongly depends on the steps. In order to achieve better interface quality, step density can be an important factor. This effect decreases as material purity increases. Surface morphology can be improved since the terraces suppress the nucleation of islands in favour of step propagation. Step edges with exposed gallium atoms suppress the incorporation of lattice defects, resulting in straight terraces. [55]

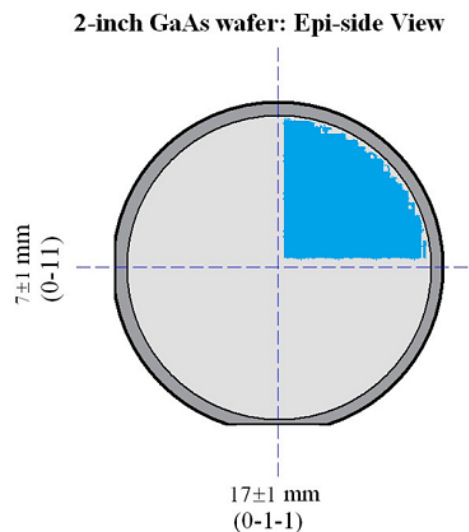


Figure 6.3 Epi-side view of a 2-inch GaAs wafer.

In order to study the influence of misorientation angle on the performance of THz QCLs, samples were grown by MBE on various GaAs substrates, i. e.

(100) substrate, and substrates misoriented by 2° , 4° , and 6° towards (111). The growth procedure followed the general THz QCL growth methodology as explained in Chapter 2. The growth temperature was 585°C and was monitored by pyrometric detector. Each wafer was cleaved into quarters from a 2-inch standard-sized wafer and a quarter wafer of each was mounted on the same substrate holder, in order to keep the film thickness, film composition, doping concentration and background impurity level the same. Fig. 6.3 shows a schematic diagram of a 2-inch GaAs wafer from epilayer side. The shadowed area shows a quarter wafer being cleaved.

6.2.2 Surface morphology

In order to distinguish the surface properties of the misorientated samples, atomic force microscopy (AFM) was used and the roughness of wafer L903 (itself comprising the four quarter wafers each with a different misorientation angle) was measured at a high resolution. AFM is commonly used to identify atoms on a sample surface and evaluate any interaction between atoms.

The difference of sample surface quality is shown in Fig. 6.4. The surface roughness improves upon increasing the misorientation angle. It is observed that the 0° surface is rough and there is an improvement in the sample misorientated by 2° . For 4° and 6° samples, the surface smoothness has been improved further, with 6° having the best surface quality. It is also apparent that the optimization range is narrow among 2° , 4° and 6° samples.

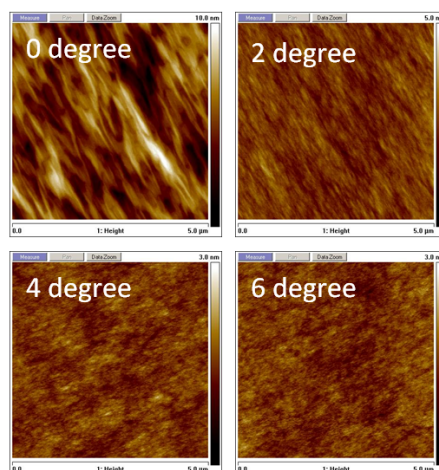


Figure 6.4 Surface profile image measured by AFM on L903 wafers with 0° , 2° , 4° , and 6° misorientation angles.

Fig. 6.5 presents the root mean square (rms) roughness as a function of the misorientation angle. The rms roughness of the THz QCL wafers grown on 0° , 2° , 4° and 6° misoriented GaAs substrates is about 1.8, 0.25, 0.2, and 0.15 \AA , respectively. The rms roughness decreases with the increase of the misorientation angle, and there is an abrupt decrease from 0° to 2° , with the decrease rate becoming relatively mild after 2° , indicating that the difference of surface morphology is greatly affected by the misorientation compared with the (100) surface, while the differences between misorientated substrates are not distinct.

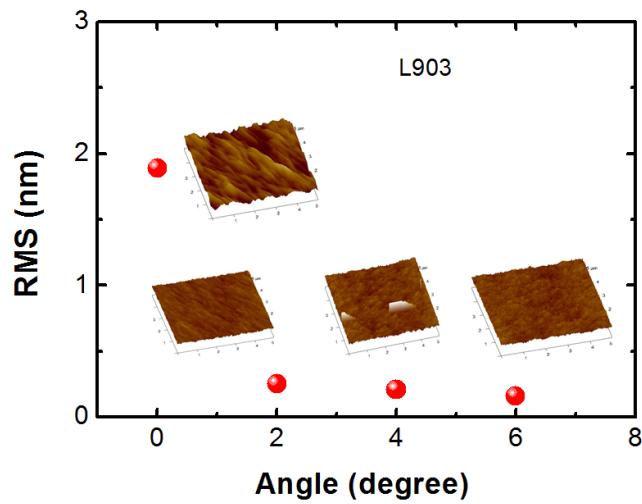


Figure 6.5 Rms roughness as a function of misorientation angle.

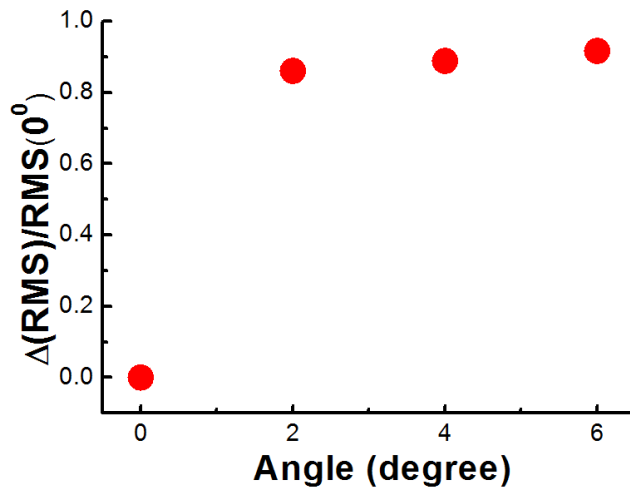


Figure 6.6 The improvement of surface roughness as a function of misorientation angle.

Compared with the 0° sample, the rms roughness decreased by 86.1% for the 2° sample, by 88.9% for the 4° sample, and by 91.7% for the 6° sample, as shown in Fig. 6.6. For misorientation angles from 2° to 6°, there is an approximate linear correlation between the improvement of surface roughness and the increase of misorientation angle.

According to these AFM results, THz QCL wafers grown on misorientated GaAs substrates show much better surface quality, which is in accordance with previous research.

6.3 BTC QCLs on misorientated substrates

6.3.1 Active region structure

The properties of a BTC THz QCL structure grown on misorientated substrates were studied on the L904 wafer set. The QCL active region structure has a nine-well design as shown in the schematic diagram Fig. 6.7 [40].

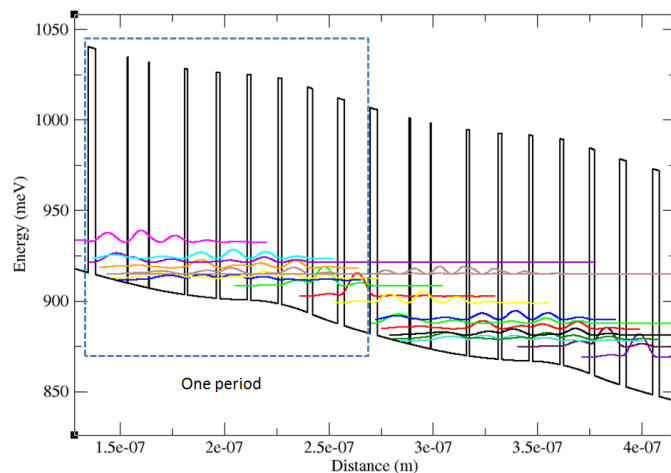


Figure 6.7 Conduction-band diagram and electron subband wave functions squared, calculated self-consistently using Schrödinger–Poisson solver [1] of BTC structure of L904.

The layer thicknesses are given in nanometers with GaAs wells in standard type and $\text{Al}_{0.15}\text{Ga}_{0.85}\text{As}$ barriers in bold. Underlined layers are doped at $1.6 \times 10^{16} \text{ cm}^{-3}$. Layer thicknesses are as follows:

3.5/15.0/0.55/9.6/0.55/16.9/1.4/13.7/1.7/13.1/1.9/12.8/1.9/12.2/2.5/12.1/3.2/12.4. This BTC structure has a longer period, but fewer repeats, compared with other BTC QCLs, thus reducing the electric field required for operation,

and consequently reducing the heating as well as the operating voltage. [40][115]

6.3.2 Results and analysis

Four groups of samples from structure L904, with 1.5 mm, 2.0 mm, 2.5 mm and 3 mm laser ridge lengths and all of 230 μm width, were fabricated at the same time. All devices were fabricated into SISP waveguide THz QCL lasers. In each group, four devices were grown with misorientation angles 0° , 2° , 4° , and 6° toward (111). Table 6.1 lists the main results collected from structure L904, including output power, threshold current density and maximum operating temperature. The measurements were taken using pulsed mode operation with 2% duty cycle.

Wafer No.	Active region structure	Misorientation angle (degree)	Cavity length (mm)	Ridge width (μm)	Power (mW) at 10 K	J_{th} (A/cm^2)	T_{max} (K)
L904	BTC	0°	3	230	2.5	187	72
		2°	3	230	7.5	157	76
		4°	3	230	2.5	167	83
		6°	3	230	10	190	76
		0°	2	230	2.3	143	79.5
		2°	2	230	8.5	136	79.5
		4°	2	230	7	161	81
		6°	2	230	9.3	156	79.5
		0°	1.5	230	13	161	76
		2°	1.5	230	6.3	157	76
		4°	1.5	230	7	176	79
		6°	1.5	230	6	222	52
		0°	2.5	230	6.8	150	80
		2°	2.5	230	7.5	150	80
		4°	2.5	230	11.2	173	80
		6°	2.5	230	9.8	171	79.5

Table 6.1 Measurement details of structure L904 on different misorientated substrates.

According to the comparison between the four different angles for the 3 mm, 2.5 mm, 2 mm and 1.5 mm-long lasers, the 4° devices always show higher T_{max} compared with lasers having other misorientation angles. Fig. 6.8 also shows that the increase of T_{max} is more obvious for the 3 mm-long device. The possible reason is that since mirror loss decreases due to the increase of laser cavity length, and consequently the effect of misorientation on the device performance becomes more obvious. Although 4° lasers operate at a

higher T_{\max} , the differences among them are smaller, compared with lasers having other misorientation angles. In addition, it is observed that the maximum operating temperature increases with misorientation angle from 0° to 4° , but drops to a lower level at 6° . However, between 0° and 6° , there is no clear conclusion on which has a consistently lower T_{\max} . Therefore, the results suggest that the 4° sample has a slightly higher operating temperature for this structure.

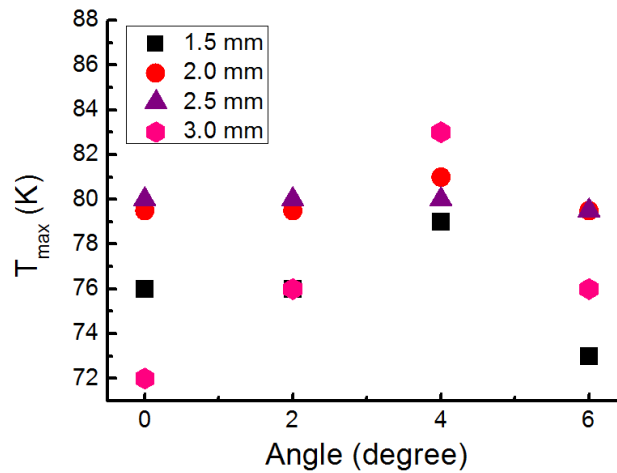


Figure 6.8 Maximum operating temperature as a function of misorientation angle for L904.

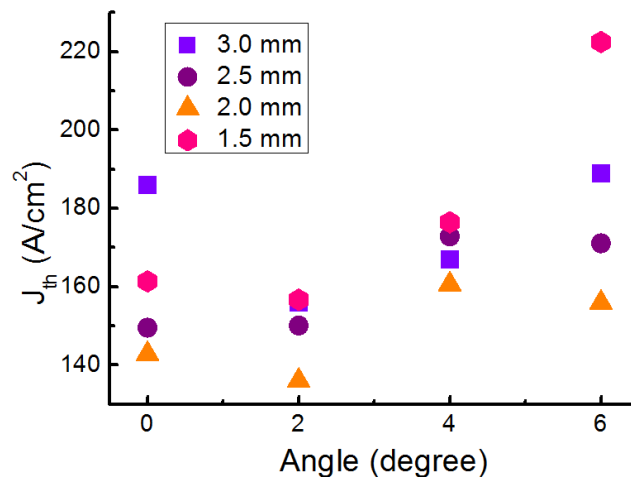


Figure 6.9 Threshold current density at 10 K as a function of misorientation angle.

Considering the threshold current density, the 2° lasers show the lowest J_{th} , whilst the 6° lasers have the highest J_{th} , as shown in Fig. 6.9. J_{th} decreases from 0° to 2° and then increases from 2° to 6° , for both the 1.5 and 3 mm

lasers. However, in the cases of the 2 and 2.5 mm lasers, the 6° laser with 2 mm length shows a lower threshold compared with the 4° sample, while the 0° laser with 2.5 mm length operates at a slightly higher threshold than the 2°. These observations suggest a possible improvement in J_{th} in the samples with 2° misorientation angle, while the other three angles show a variety of possibilities without a clear trend.

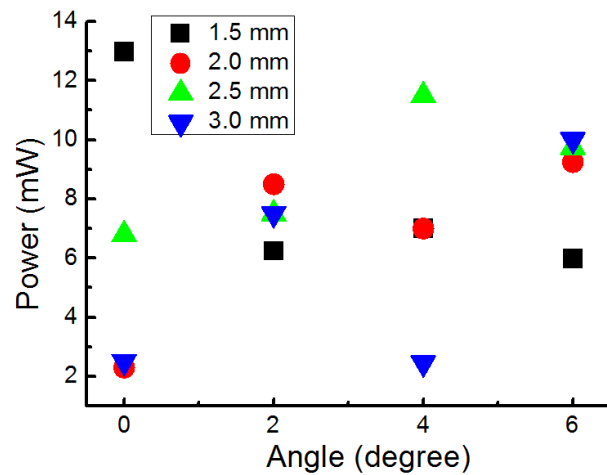
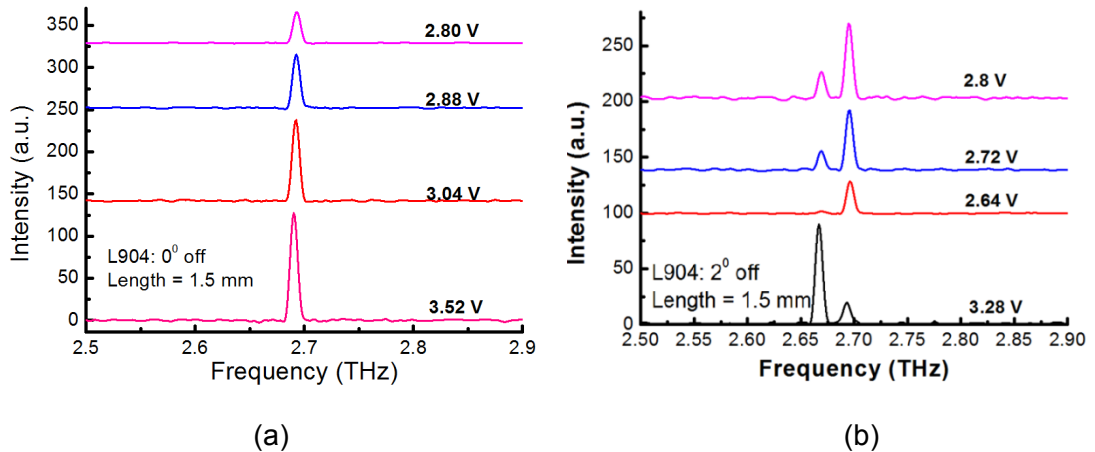


Figure 6.10 Peak power at heat-sink temperature of 10 K as a function of misorientation angle for wafer L904.

The power performances of devices with 0°, 2°, 4°, and 6° misorientation angles are also compared. In Fig. 6.10, the power has been measured at a heat-sink temperature of 10 K. However, no clear correlation can be attributed since the power does not vary with the misorientation angle in a consistent way for devices with different lengths.



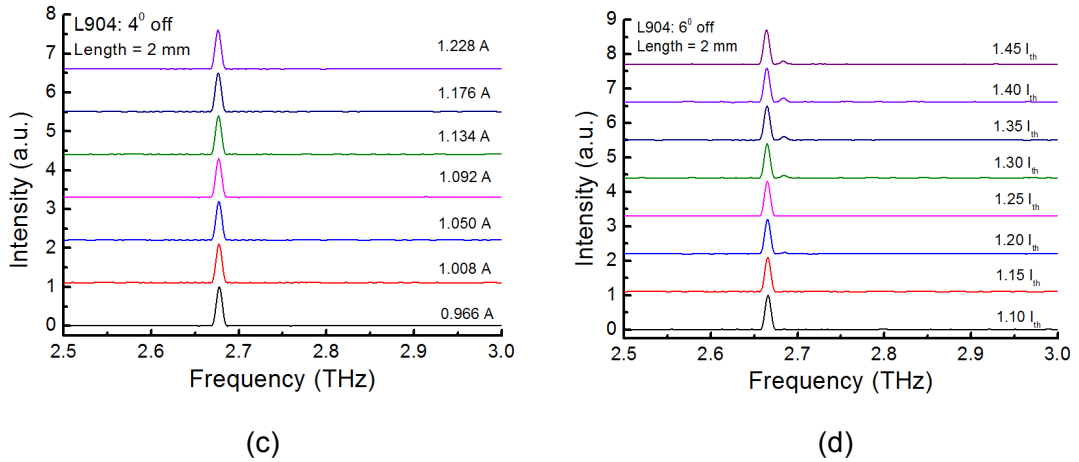
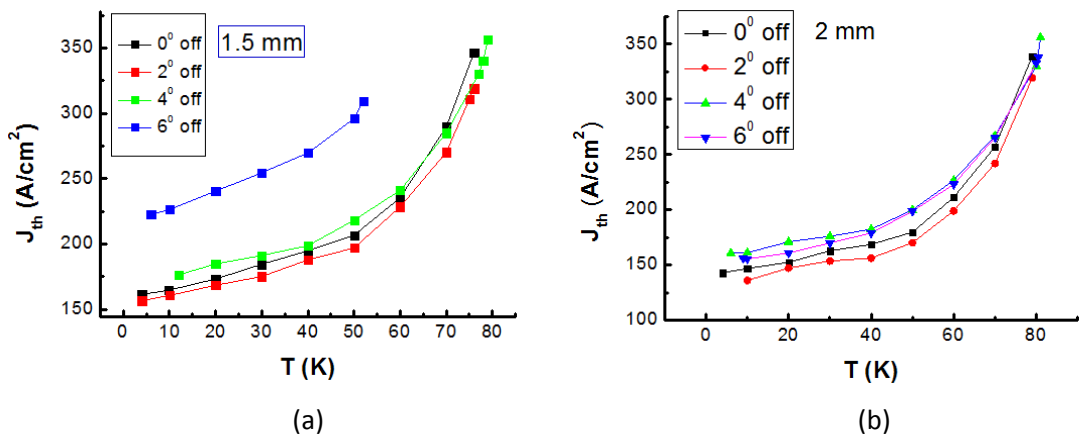
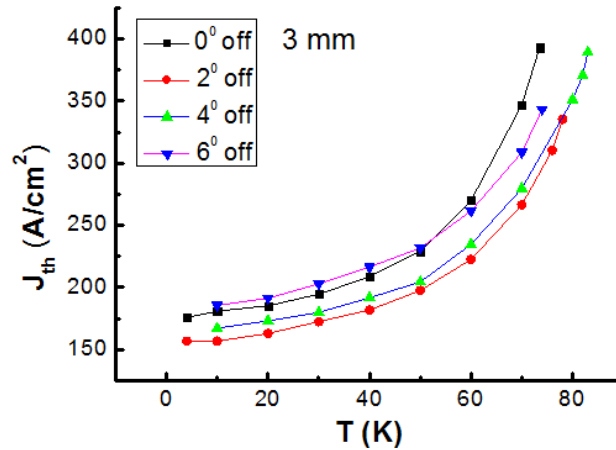


Figure 6.11 Spectral characteristics of L904 (a) 0° off, 1.5 mm (b) 2° off, 1.5 mm (c) 4° off, 2 mm (d) 6° off, 2 mm.

Spectral properties are presented in Fig. 6.11. The spectra are collected by FTIR measurement at different applied biases at a heat-sink temperature of 10 K. Fig. 6.11 (a) and (b) present the spectra from the 1.5-mm-long-L904 wafers with misorientation angles of 0° and 2°, respectively, while Fig. 6.11 (c) and (d) show the spectra of 2-mm-long L904 wafers with angles 4° and 6°, respectively. The central emission frequencies for all devices are between 2.65 to 2.7 THz. Some variations in single-mode and multi-mode features are observed. For example, the 2° laser shows a more obvious multi-mode feature, while the 0° and 4° lasers are single-mode devices. However, this difference is not necessarily related to the misorientation angles.





(c)

Figure 6.12 Current density as a function of heat-sink temperature for L904 for (a) 1.5 mm, (b) 2 mm, and (c) 3 mm-long devices.

Fig. 6.12 shows the threshold current density as a function of heat-sink temperature, with 1.5 mm, 2 mm and 3 mm devices from structure L904 being compared. The current density increases exponentially with heat-sink temperature for all misorientation angles. For all three different lengths, the 2° devices show a consistent lowest current density at each heat-sink temperature. In Fig. 6.12 (a), for the 1.5-mm-long devices, the 0° laser showed much higher current densities than for the other angles.

From the above results on the BTC structure L904, T_{\max} and J_{th} show some consistent relationship on the misorientation angle of THz QCL wafers, although some differences in performances are observed. The 4° might have a slight advantage on temperature performance and the 2° shows a lower threshold in most cases. The power performance does not clearly relate to the angle. However, further experiments on BTC structures will be required before a convincing conclusion can be reached.

6.4 Hybrid THz QCLs on misorientated substrates

Based on the initial results from the BTC structure discussed above, a hybrid QCL structure was next studied in order to attempt to understand more clearly the misorientation effects on THz QCLs. The hybrid active region was explained in Chapters 2 and 4, and combines two fundamental designs, BTC and RP [47]. The designed frequency used here was around 3.1 THz.

Three series of wafers were grown, L903, L989 and L991, and devices fabricated into SISF waveguides. Comparisons were made between devices with identical growth and fabrication parameters although with different wafer orientations.

L903 samples were grown on four quarter wafers with mis-orientation degrees 0° , 2° , 4° and 6° . L989 and L991 were grown on two half wafers with different misorientation angles, with the same hybrid structure as L903. The data from L989 is presented in Table 6.2. 2-mm and 3-mm-long devices were characterised.

Device	Cavity length (mm)	T_{\max} (K)	Power at 10K (mW)	J_{th} at 10K (A/cm^2)
L989: 0°	2	71	7.9	188
L989: 4°	2	82	14.6	168
L989: 0°	3	88	29	189
L989: 4°	3	86	13.8	160

Table 6.2 Details of 2-mm long and 3-mm long L989 devices.

6.4.1 Spectral property

Fig. 6.13 (a) and (b) show the spectral properties of two 2 mm-long lasers from L989 with 0° and 4° misorientation angles. Both lasers emit at 3.1~3.25 THz and both show multi-mode spectral properties. Fig. 6.14 (a) and (b) compare the spectra from 3-mm-long L903 devices with 0° and 4° misorientation angles. Similarly, both show multi-mode spectra. However, it is observed that in the 0° devices, for both L989 and L903, the emission frequency ranges are narrower than for the 4° lasers, especially at higher biases.

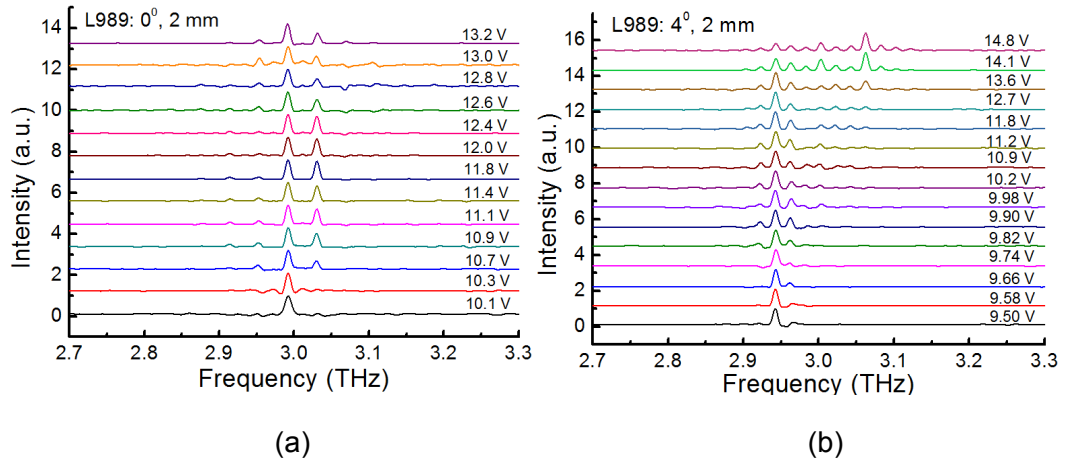


Figure 6.13 Spectral characteristics of L989 (a) 0° off, 2 mm (b) 4° off, 2 mm.

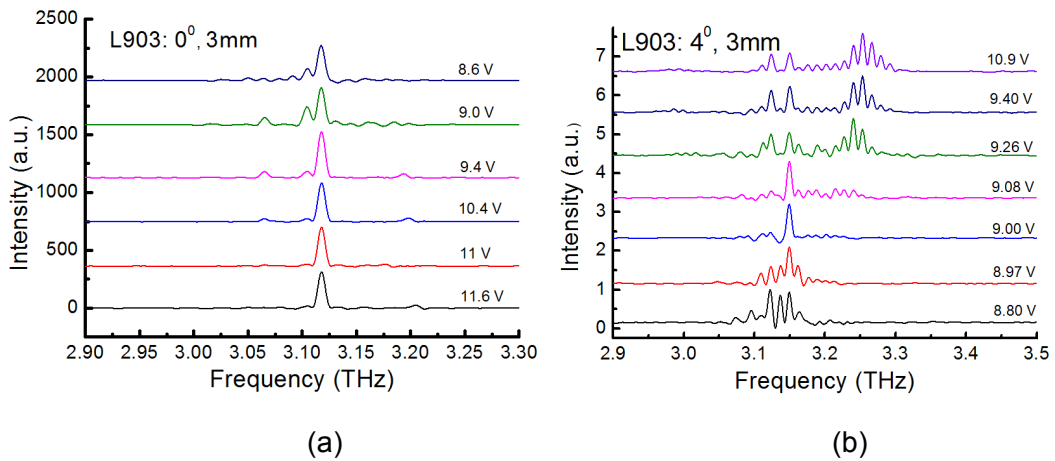


Figure 6.14 Spectral characteristics of L903 (a) 0° off, 3 mm (b) 4° off, 3 mm.

6.4.2 Maximum operating temperature

Considering the maximum temperature performance in L989, at a 4° misorientation angle, there is a slight decrease in T_{\max} for a 3-mm-long laser, but an 11 K improvement occurs in a 2-mm-long laser, as shown in Fig. 6.15 and Table 6.2. The temperature performance is slightly better in 4° in most cases, while the optimization range is not as large as expected.

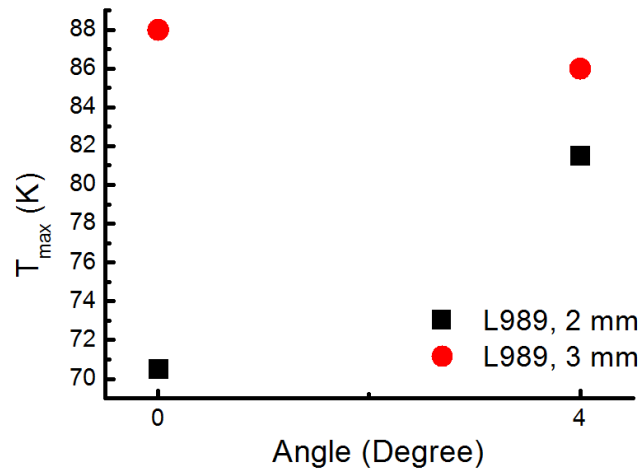


Figure 6.15 Maximum operating temperature as a function of misorientation angle for L989.

6.4.3 Threshold current density and dynamic range

The threshold current densities and dynamic ranges were compared. Fig. 6.16 shows the result from wafer L989. Two devices were measured, being 2 mm and 3 mm-long lasers with a 150 μm ridge width. For both device lengths, the threshold current density was lower for the 4° misorientation angle. There was a 12% decrease of J_{th} for the 2-mm-long devices and an 18% for the 3-mm-long devices. In addition, the difference of J_{th} between the 2-mm and 3-mm-long devices was larger when at a 4° misorientation angle; 29 A/cm^2 compared with 20 A/cm^2 .

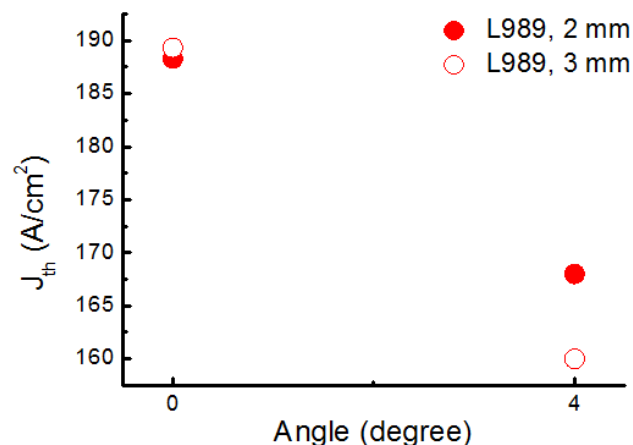


Figure 6.16 Threshold current density as a function of misorientation angle for L989 with 150 μm width and 2 mm/3 mm cavity lengths.

The current density as a function of heat-sink temperature is plotted in Fig. 6.17, where both L989 and L991 devices are compared. The devices are 3 mm long and 150 μm wide. It is shown that for L989, the 4° sample always operates at lower current densities, while for L991, the 4° laser also has a slightly lower threshold current density.

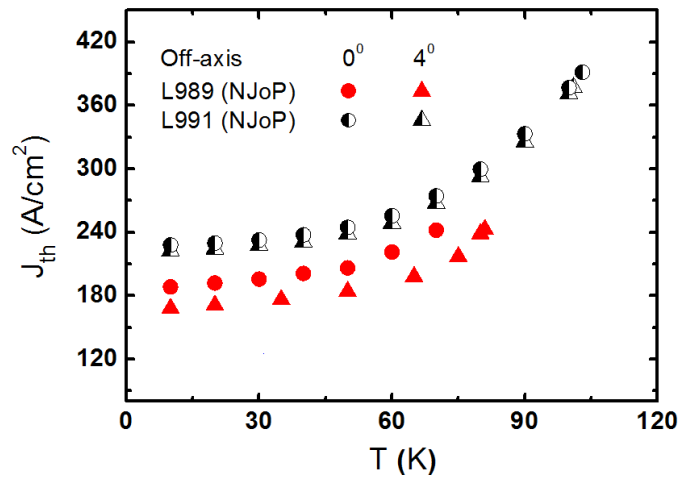


Figure 6.17 Threshold current density as a function of heat-sink temperature for L989 and L991 devices with 0° and 4° misorientation angles.

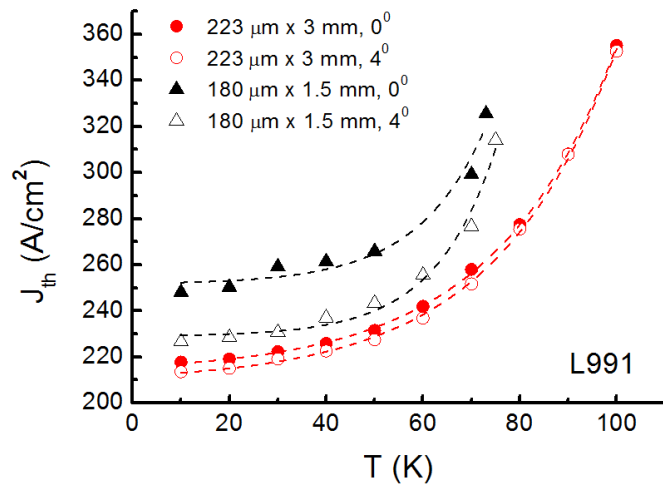


Figure 6.18 J_{th} as a function of heat-sink temperature of wafer L991.

Fig. 6.18 shows the current density as a function of heat-sink temperature for two groups of L991 devices. Each group has the same laser ridge width and cavity length, but with different misorientation angles (0° and 4°). The first two samples were fabricated into a wider ridge and longer length, which are 223 μm and 3 mm. The other two samples are 180 μm wide and 1.5 mm

long. Both groups show similar results; namely that the 4° lasers have lower current densities. Therefore, this effect does not appear to be related with the laser area.

The dynamic range is analysed in Fig. 6.19. 3-mm-long L989 devices with 0° and 4° misorientation angles were studied. For both angles, the dynamic range increases with the heat-sink temperature and then decreases. The peak of the dynamic ranges appear at different temperatures for the 0° and 4° samples. Considering the laser with the 0° angle, the dynamic range reaches the maximum at the heat-sink temperature of approximately 20 K, while for the 4° sample, the maximum appears later at 30 K. There is a possible relationship between the laser dynamic range and the misorientation angle. Moreover, the dynamic range of the 4° laser is much larger than the 0° at each measured heat-sink temperature, and the difference of dynamic range generally decreases with the increase of heat-sink temperature, due to heat-dissipation.

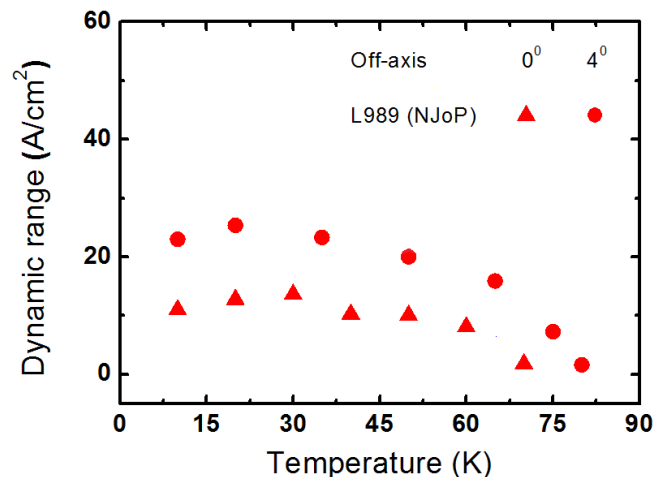


Figure 6.19 Dynamic range as a function of heat-sink temperature for L989 0° and 4° samples.

6.4.4 Power performance

The peak output power at different heat-sink temperatures was compared between samples with different misorientation angles. The power was measured by a TK power meter without considering collection efficiency, and the calibration approach kept the same for different measurements. Fig. 6.20 shows the peak output power as a function of heat-sink temperature. L991 and L989 devices are compared between 0° and 4° angles. The black

curves and symbols represent results from L991, and the red ones from L989.

The output power decreases with the heat-sink temperature in all cases. Both the 4° samples show higher power at each heat-sink temperature. As the temperature increases, the difference in output power between 0° and 4° becomes smaller, due to the heat dissipation effect.

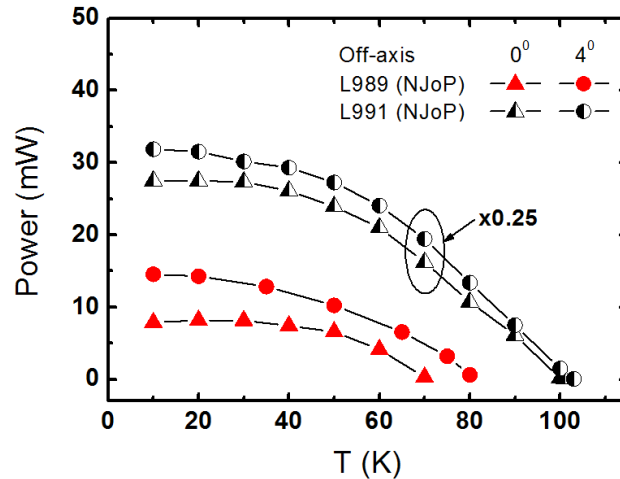


Figure 6.20 Dynamic range as a function of heat-sink temperature for L989 and L991 with 0° and 4° off samples.

6.5 Summary

It has been demonstrated that the misorientation of (100) GaAs substrates has some effect on the material properties of THz QCLs. Surface morphology can be greatly improved by misorientating the GaAs substrate. Even a 2° misorientation angle can achieve a much smoother sample surface, and the results showed that the best surface morphology and interface sharpness were obtained on the (100) tilted 6° off toward (111) GaAs substrate, within the four angles studied.

From experiments based on two different THz QCL active region structures grown on misorientated substrates, some interesting initial results emerge although there is no single conclusion on the best misorientation angle to optimize all laser parameters simultaneously. A 4° angle achieved slightly lower threshold current densities, and higher power for the 3.1 THz hybrid structure. Higher temperature performance has been observed in 4° samples in the BTC structure, and a lower threshold occurs in 2° samples.

Although the initial results do not show a compelling relationship between the misorientation angle and THz QCL performance, the misorientation angle appears to influence the device parameters, and possibilities for optimization of THz QCLs are discussed and suggested. This topic merits further study and more QCL structures ought be investigated in order to reach a clearer conclusion.

Chapter 7

Conclusion and further work

7.1 Conclusions

The primary emphasis of this thesis is on the performance enhancement of THz QCLs based on MBE growth, device fabrication and electrical characterisation. The development of THz technology, including different sources and applications, is reviewed. The reproducibility of high performance THz QCLs are investigated and laser parameters are studied. BTC and hybrid THz QCL structures are grown, fabricated and characterised with varied growth and fabrication parameters, and possibilities for their further improvement are suggested. The growth of THz QCLs on different substrate orientations is explored.

The key achievements are the demonstration of high power THz QCLs for the first time with output power exceeding 1 watt, the optimization on the injector doping of THz QCLs with different designs, and the high quality material growth. The enhancement in THz QCL performances are essential in future applications such as imaging and remote sensing.

7.1.1 Material quality of THz QCLs

To optimize the material quality of THz QCLs, improving the growth reproducibility, such as the growth rate stability, and Si doping calibration accuracy, interface roughness and decreasing the background impurity level are essential considerations.

The MBE system and standard procedures of MBE growth, including growth calibration (flux, growth rate and temperature), the growth process of THz QCLs, and factors affecting the material quality, are described in Chapter 2, Chapter 5, and Chapter 6. The pyrometric method is useful in determining the layer thicknesses and alloy compositions. Compared with x-ray diffraction measurements, this method provides more accurate information on the growth rate. It can also be used in compensating the growth rate drift, as discussed in chapter 5, which significantly improves the layer uniformity and growth reproducibility of THz QCLs. The Si doping has to be calibrated accurately and efficiently. Two different approaches, the VDP Hall approach and the SIMS method, are compared in Chapter 2. It is found that the VDP Hall method is a simple way for doping calibration and provides accurate

results, whilst the SIMS method has the advantage of calibrating multiple doping levels from the growth of only one sample. The comparisons between these two methods have suggested that both can be considered in the Si doping calibration.

The incorporation of background impurities during the growth of THz QCLs affects the scattering, unintentional tunnelling within the laser and the lifetimes of the laser levels and the electron injection efficiency. The background impurity level can be determined by growing an unintentionally doped bulk GaAs layer and the VDP Hall measurement. The results and discussions in Chapter 5 have suggested that high background doping degrades the laser performance, including adversely affecting the power, dynamic range and maximum operating temperature. The comparison is made between samples grown by two Ga cells with different background impurity levels. The samples grown by a contaminated cell emitted lower output power and there was only a small increase of the output power when increasing the injector doping level. The dynamic range is also much narrower. In addition, the maximum operating temperature is lower for the wafer grown at a higher background doping level. Therefore, in order to achieve better THz QCL performance, the background doping level in a MBE system is required to be minimized.

It has been suggested by different research groups that surface morphology influences the electrical and optical properties of devices. One way to improve the surface morphology is to misorientated (100) GaAs substrates towards (111) direction. The effect is compared between samples grown on 0°, 2°, 4° and 6° (100) GaAs substrates on a BTC QCL structure, and 0° and 4° on a hybrid QCL structure. It has been observed from the experiments that the misorientation improves the surface smoothness of THz QCLs significantly. 2°, 4° and 6° samples have achieved much smoother surfaces compared with 0° samples, and the surface smoothness increases with the angle of misorientation. For the BTC structure, although some differences in performances have been observed, the 4° might have a slight advantage on temperature performance and the 2° shows a lower threshold in most cases. The power performance does not clearly relate to the angle. For the hybrid structure, between 0° and 4° samples, the 4° samples show higher power than 0° samples. The 4° lasers also have lower threshold current densities. Therefore, the maximum operating temperature, threshold current density and peak output power are affected by the misorientation angles;

Notwithstanding, the influences of the misorientation are still not conclusive, according to the initial results.

7.1.2 Optimization on device performances

The optimization of THz QCL performances has been investigated in output power, operating temperature, threshold current density and dynamic range on both hybrid and BTC structures.

The power performance of THz QCLs is studied in Chapter 4. High power in THz QCLs can be achieved by fabricating broad area laser ridges with SISP waveguide. The power optimization approaches are determined by theoretical analysis and simulations. The shift of frequency from 3.1 THz to 3.4 THz helps increase the power. The peak power increases linearly with the area of the device. An HR coating on the back facet improves the THz QCL power and threshold performances effectively. Comparing the two 1.8 mm-long and 328 μm -wide devices, the facet coated device shows a 7% reduction in the threshold current density, and a 36.7% increase of peak output power, in comparison with the device with an uncoated back facet. T_{max} has been observed to increase with the device area for both HR coated and uncoated devices, according to a group of data. However, more data for HR coated devices may give a clearer conclusion. The highest power for THz QCLs (426 μm x 3 mm) without HR coating achieved 773 mW at 10 K with 2% duty cycle, at the current density of 673 A/cm². 1 Watt output power has been achieved from a 426- μm -wide and 4.2-mm-long device, with a 180- μm -thick substrate.

The injector doping level is an essential factor that influences THz QCL performances. Samples with identical growth parameters, but different injector doping levels, were compared. Higher injector doping level results in a high threshold and output power, due a stronger population inversion and a higher gain. It is observed that the threshold current density increases with the injector doping as well as the dynamic range, but with the consequence of device heating. However, there is no clear trend between the maximum operating temperature and injector doping level, although the results suggest a higher doping level leads to a higher maximum operating temperature. Comparing the L-I-V and spectral characteristics of THz QCLs with emission frequency between 2.8 ~ 2.95 THz under CW mode operation, higher threshold current densities in CW mode are shown. It was also found that the improvement of J_{th} in pulsed mode is more obvious than in CW mode for

the same injector doping level. The transit time in one period of the active region for devices with the same active region structure was also investigated. It was observed that the devices with larger transit time have a less good performance, lower T_{\max} , in particular, possibly due to the scattering.

7.2 Further work

The work in this thesis is based on the growth and device optimization of GaAs/AlGaAs THz QCLs. However, following previous work, there is still much to improve in their material quality, and different device fabrication techniques are yet to be explored for both SISP and DM waveguide devices. The main goal is to improve the maximum operating temperature, the peak output power, lower the threshold current density and improve the heat dissipation.

Firstly, the maximum operating temperature can be improved further. The current active region designs have their advantages and disadvantages. RP structure has achieved the best maximum operating temperature up to 200 K. The possible way is to experiment with new active region designs or improve conventional designs by refining the fundamental parameters of THz QCL structures, such as upper and lower state lifetimes, gain and oscillator strength. Secondly, since the THz QCLs investigated here are based on a GaAs/AlGaAs material system, new materials can be considered in future research, such as InP based materials including InGaAs/GaAsSb. [116] Material quality can also be improved further, which involves more precise control and investigation into different growth parameters, such as growth temperature, as well as the optimization in both SISP and DM waveguide device fabrication. The fabrication procedure can be modified by trying different etching techniques to create better laser ridges, improving metal layers and trying new laser waveguides. Chapter 3 mentions that different wet etchants can result in isotropic and anisotropic laser ridge edge profile, and previous devices were all based on the same anisotropic etchant, so further work on THz QCLs by varying laser ridge profile, using different etching techniques, such as dry etching, can be carried out.

Considering the power performance: since the previous high power THz QCLs could only operate in pulsed mode, due to the high threshold current density which produces excessive heating, heat dissipation can be improved

further to lower the lasing threshold, for example, by considering a different substrate material which has a better heat dissipation than of GaAs. Single mode lasers with higher power can be investigated, for example, by combining the DFB laser and the higher power laser, or possibly considering the tapered laser ridge design in device fabrication. Other QCL structures with different emission frequencies are also worth studying, since high power is desirable for most THz QCLs in most applications.

Bibliography

- [1] R. Paiella (ed), Intersubband Transitions in Quantum Structures, ISBN: 9780071457927, (2005).
- [2] Edited by A. Baronov, E. Tournie, Semiconductor lasers, fundamentals and applications, Woodhead publishing series in electronic and optical materials, (2013).
- [3] J. Faist, L. Ajili, G. Scalari, M. Giovannini, M. Beck, M. Rochat, H. Beere, A. G. Davies, E. H. Linfield and D. Ritchie, Terahertz Quantum Cascade Laser, Philosophical Transactions: Mathematical, Physical and Engineering Sciences, Vol. 362, No. 1815, The Terahertz Gap: The Generation of Far-Infrared Radiation and its Applications, pp. 215-231, (2004).
- [4] D. J. Paul, Quantum Cascade Lasers, Physics and Applications of Terahertz Radiation, Springer Series in Optical Sciences, Vol. 173, pp 103-121, (2014).
- [5] R. A. Lewis, A review of terahertz sources, J. Phys. D: Appl. Phys. 47 374001 (11pp), (2014).
- [6] M. Tonouchi, Cutting-edge terahertz technology, Nature Photonics, Vol.1, (2007).
- [7] H. W. Hübers, S. G. Pavlov, and A. D. Semenov, R. Köhler, L. Mahler, and A. Tredicucci, H. E. Beere and D. A. Ritchie, E. H. Linfield, Terahertz quantum cascade laser as local oscillator in a heterodyne receiver, OPTICS EXPRESS, Vol. 13, No. 15, (2005).
- [8] J. Darmo, V. Tamosiunas, G. Fasching, J. Kröll, and K. Unterrainer, M. Beck, M. Giovannini, and J. Faist, C. Kremser and P. Debbage, Imaging with a Terahertz quantum cascade laser, OPTICS EXPRESS, Vol. 12, No. 9, (2004).
- [9] G. Scalari, C. Walther, M. Fischer, R. Terazzi, H. Beere, D. Ritchie, and J. Faist, THz and sub-THz quantum cascade lasers, Laser & Photon. Rev. 3, No. 1-2, 45-66, (2009).
- [10] L. Ajili, Quantum cascade lases at terahertz frequencies, Thesis, (2007).
- [11] R. F. Kazarinov, R. A. Suris, "Possibility of amplification of electromagnetic waves in a semiconductor with a superlattice". Fizikai Tehnika Poluprovodnikov 5 (4): 797–800, (1971).

- [12] J. Faist, F. Capasso, D. L. Sivco, C. Sirtori, A. L. Hutchinson, A. Y. Cho, Quantum cascade laser, *Science*, Vol. 264, 553–556, (1994).
- [13] J. Faist, F. Capasso, C. Sirtori, D. L. Sivco, J. N. Baillargeon, A. L. Hutchinson, S. G. Chu, and A. Y. Cho, "High power mid-infrared ($\sim 5 \mu\text{m}$) quantum cascade lasers operating above room temperature", *Appl. Phys. Lett.* 68, 3680, (1996).
- [14] Y. Bai, S. R. Darvish, S. Slivken, W. Zhang, A. Evans, J. Nguyen, and M. Razeghi, "Room temperature continuous wave operation of quantum cascade lasers with watt-level optical power", *Appl. Phys. Lett.* 92, 101105, (2008).
- [15] A. Lyakh, C. Pflügl, L. Diehl, Q. J. Wang, Federico Capasso, X. J. Wang, J. Y. Fan, T. Tanbun-Ek, R. Maulini, A. Tsekoun, R. Go, and C. Kumar N. Patel, "1.6 W high wall plug efficiency, continuous-wave room temperature quantum cascade laser emitting at $4.6 \mu\text{m}$ ", *Appl. Phys. Lett.* 92, 111110, (2008).
- [16] J. Faist, C. Gmachl, F. Capasso, C. Sirtori, D. L. Sivco, J. N. Baillargeon, and A. Y. Cho, "Distributed feedback quantum cascade lasers", *Appl. Phys. Lett.* 70, 2670, (1997).
- [17] R. Maulini, M. Beck, J. Faist, and E. Gini, "Broadband tuning of external cavity bound-to-continuum quantum-cascade lasers", *Appl. Phys. Lett.* 84, 1659, (2004).
- [18] S. Khanal, L. Zhao, J. L. Reno and S. Kumar, Temperature performance of terahertz quantum-cascade lasers with resonant phonon active-regions, *J. Opt.* 16, 094001, (2014).
- [19] R. Köhler, A. Tredicucci, F. Beltram, H. Beere, E. H. Linfield, A. G. Davies, D. Ritchie, R. Iotti, and F. Rossi, Terahertz semiconductor-heterostructure laser, *Nature*, Vol.417, pp.156-159, (2002).
- [20] S. Fatholouloumi, E. Dupont, C. W. I. Chan, Z. R. Wasilewski, S. R. Laframboise, D. Ban, A. Matyas, C. Jirauschek, Q. Hu, and H. C. Liu, Terahertz quantum cascade lasers operating up to $\sim 200\text{K}$ with optimized oscillator strength and improved injection tunnelling, *Optics express*, Vol.20, No.4, (2006).
- [21] A. Tredicucci, R. Köhler, L. Mahler, H. E. Beere, E. H. Linfield and D. A. Ritchie, Terahertz quantum cascade lasers – first demonstration and novel concepts, *Semicond. Sci. Technol.* 20, S222-S227, (2005).

- [22] Y. Ren, R. Wallis, Y. D. Shah, D. S. Jessop, R. Degl'Innocenti, A. Klimont, V. Kamboj, H. E. Beere, and D. A. Ritchie, Single mode terahertz quantum cascade amplifier, *Applied Physics Letters* 105, 141102, (2014).
- [23] D. Bachmann, N. Leder, M. Rosch, G. Scalari, M. Beck, H. Arthaber, J. Faist, K. Unterrainer, and J. Darmo, Broadband terahertz amplification in a heterogeneous quantum cascade laser, *Optics Express*, Vol. 23, No. 3, (2015).
- [24] A. Campa, L. Consolino, M. Ravaro, D. Mazzotti, M. S. Vitiello, S. Bartalini, and P. D. Natale, High-Q resonant cavities for terahertz quantum cascade lasers, *Optics Express*, Vol. 23, No. 3, (2015).
- [25] N. K. Saat, P. Dean, S. P. Khanna, M. Salih, E. H. Linfield and A. G. Davies, Switching Circuit to Improve the Frequency Modulation Difference-Intensity THz Quantum Cascade Laser Imaging, *AIP Conference Proceedings* 1657, 040004, (2015).
- [26] M. Krall, M. Martl, D. Bachmann, C. Deutsch, A. M. Andrews, W. Schrenk, G. Strasser, and K. Unterrainer, Coupled cavity terahertz quantum cascade lasers with integrated emission monitoring, *Optics Express*, Vol. 23, Issue 3, pp. 358 -3588, (2015).
- [27] P. Dean, J. Keeley, A. Valavanis, K. Bertling, Y. L. Lim, T. Taimre, R. Alhathloul, L. H. Li, D. Indjin, A. D. Rakic, E. H. Linfield, and A. G. Davies, Active phase-nulling of the self-mixing phase in a terahertz frequency quantum cascade laser, *Optics Letters*, Vol. 40, Issue 6, pp. 950-953, (2015).
- [28] L. Consolino, A. Campa, M. Ravaro, D. Mazzotti, M. S. Vitiello, S. Bartalini, and P. D. Natale, Saturated absorption in a rotational molecular transition at 2.5 THz using a quantum cascade laser, *Applied Physics Letters* 106, 021108, (2015).
- [29] W. Miao, Z. Lou, G. Xu, J. Hu, S. Li, W. Zhang, K. Zhou, Q. Yao, K. Zhang, W. Duan, S. Shi, R. Colombelli, H. E. Beere, and D. A. Ritchie, Demonstration of a fully integrated superconducting receiver with a 2.7 THz quantum cascade laser, *Optics Express*, Vol. 23, No. 4, (2015).
- [30] M. S. Vitiello, G. Scalari, B. Williams, and P. D. Natale, Quantum cascade lasers: 20 years of challenges, *Optics Express*, Vol. 23, No. 4, (2015).
- [31] M. A. Belkin, Q. J. Wang, C. Pflügl, A. Belyanin, S. P. Khanna, A. G. Davies, E. H. Linfield, and F. Capasso, High-Temperature Operation of

Terahertz quantum cascade laser sources, *Journal of Selected Topics in Quantum Electronics*, Vol. 15, No. 3, (2009).

[32] T. Grange, Nanowire terahertz quantum cascade lasers, *Applied Physics Letters* 105, 141105, (2014).

[33] S. Jung, A. Jiang, Y. Jiang, K. Vijayraghavan, X. Wang, M. Troccoli & M. A. Belkin, Broadly tunable monolithic room-temperature terahertz quantum cascade laser sources, *Nature Communications*, 5: 4267, (2014).

[34] D. Turcinkova, M. Ines Amanti, G. Scalari, M. Beck and J. Faist, Electrically tunable terahertz quantum cascade lasers based on a two-sections interdigitated distributed feedback cavity, *Applied Physics Letters* 106, 131107, (2015)

[35] Y. Bonetti and J. Faist, Quantum cascade lasers entering the mid-infrared, *Nature photonics*, Vol. 3, (2009).

[36] C. Sirtori, F. Capasso, J. Faist, A. L. Hutchinson, et al. Resonant tunneling in quantum cascade lasers, *IEEE Journal of quantum electronics*, VOL. 34, NO. 9, (1998).

[37] C. Gmachl, F. Capasso, D. L. Sivco and A. Y. Chi, Recent progress in quantum cascade lasers and applications, *Rep. Prog. Phys.* 64, 1533-160, (2001).

[38] G. Scalari, C. Walther, M. Fischer, R. Terazzi, H. Beere, D. Ritchie, and J. Faist, THz and sub-THz quantum cascade lasers, *Laser & Photon. Rev.* 3, No.1-2, 45-66, (2009).

[39] M. Rochat, L. Ajili, H. Willenberg, and J. Faist, et.al., Low-threshold terahertz quantum-cascade lasers, *Appl. Phys. Lett.*, Vol.81, No.8, (2002).

[40] S. Barbieri, J. Alton, H. E. Beere, J. Fowler, E. H. Linfield, 2.9 THz quantum cascade lasers operating up to 70K in continuous wave. *Appl. Phys. Lett.* 85,1674, (2004).

[41] B. S. Williams, S. Kumar, Q. Hu and J. L. Reno, Resonant-phonon terahertz quantum-cascade laser operating at 2.1 THz ($\lambda \cong 141 \mu\text{m}$). *Electronics Letters*, Vol. 40, No. 7, (2004).

[42] G. Scalari, N. Hoyler, M. Giovannini, and J. Faist, Terahertz bound-to-continuum quantum-cascade lasers based on optical phonon scattering extraction, *Appl. Phys. Lett.* 86, 181101, (2005).

- [43] K. Vijayraghavan, B. S. ; M. S. E, Terahertz generation with quantum cascade lasers, Dissertation in partial fulfillment of the requirements for the degree of Doctor of Philosophy, (2014).
- [44] E. H. C. Parker, The technology and physics of molecular beam epitaxy, ISBN 0-306-41860-6, (1985).
- [45] V80H-10 Molecular Beam Epitaxy Operator's Manual, (2000).
- [46] M. Wienold, L. Schrottke, M. Giehler, R. Hey, W. Anders and H. T. Grahn, Low-voltage terahertz quantum cascade lasers based on LO-phonon-assisted interminiband transitions, *Electron. Lett.*, 45, 1030, (2009).
- [47] M. Amanti, G. Scalari, R. Terazzi, M. Fischer, M. Beck, J. Faist, A. Rudra, P. Gallo and E. Kapon, Bound-to-continuum terahertz quantum cascade laser with a single-quantum-well phonon extraction/injection stage, *New J. Phys.*, 11, 125022, (2009).
- [48] L. Schrottke, M. Wienold, R. Sharma, X. Lü, K. Biermann, R. Hey, A. Tahraoui, H. Richter, H. W. Hubers and H. T. Grahn, Quantum-cascade lasers as local oscillators for heterodyne spectrometers in the spectral range around 4.745 THz, *Semicond. Sci. Technol.* 28, 035011, (2013).
- [49] H. E. Beere, J. C. Fowler, J. Alton, E. H. Linfield, D. A. Ritchie, R. Köhler, A. Tredicucci, G. Scalari, L. Ajili, J. Faist, S. Barbieri, MBE growth of terahertz quantum cascade lasers, *J. of Cryst. Growth*, 278, 756, (2005).
- [50] A. Andrews, T. Roch, A. Benz, G. Fasching, W. Schrenk, K. Unterrainer, G. Strasser, Optimization of MBE growth parameters for GaAs-based THz quantum cascade lasers, *AIP Conf Proc*, 893, 51, (2007).
- [51] T. Roch, A. Andrews, G. Fasching, A. Benz, W. Schrenk, K. Unterrainer, G. Strasser, High-quality MBE growth of $\text{Al}_x\text{Ga}_{1-x}$ As-based THz quantum cascade lasers, *Cent Eur J Phys.*, 5, 244, (2007).
- [52] Z. R. Wasilewski, MBE growth of THz quantum cascade lasers, in *Molecular Beam Epitaxy: from research to mass production*, M. Henini, ed., (Elsevier Inc., 2013).
- [53] L. H. Li, L. Chen, J. Zhu, J. Freeman, P. Dean, A. Valavanis, A. G. Davies, E. H. Linfield, Terahertz quantum cascade lasers with >1 Watt output powers, *Electron. Lett.* 50, 309, (2014).
- [54] S. P. Khanna, S. Chakraborty, M. Lachab, N. M. Hinchcliffe, P. Dean, E. H. Linfield, and A. G. Davies, Terahertz frequency quantum cascade lasers:

growth and measurement, *Terahertz Science and Technology*, 1, 22-27, (2008).

[55] R. F. C. Farrow, *Molecular Beam Epitaxy—Applications to Key Materials*, Noyes Publications, (1995).

[56] M. A. Herman, H. Sitter, *Molecular Beam Epitaxy Fundamentals and Current Status*, Springer-Verlag, (1989).

[57] M. A. Belkin, J. A. Fan, S. Hormoz, F. Capasso, S. P. Khanna, M. Lachab, A. G. Davies, and E. H. Linfield, Terahertz quantum cascade lasers with copper metal-metal waveguides operating up to 178K, *Optics Express*, Vol. 16, Issue 5, pp. 3242-3248, (2008).

[58] K. Kosiel, J. K. Traczyk, P. Karbownik, A. Szerling, et.al, "Molecular-beam epitaxy growth and characterisation of mid-infrared quantum cascade laser structures," *Microelectronics Journal* 40, 565-569, (2009).

[59] A. J. Spring Thorpe, T. P. Humphreys, A. Majeed, and W. T. Moore, In situ growth rate measurements during molecular beam epitaxy using an optical pyrometer, *Appl. Phys. Lett.*, 55, 2138, (1989).

[60] M. Cardona, in *Proceedings of the International Conference on Semiconductors of Physics*, Prague. (Academic, New York, London), p.388, (1960).

[61] S. P. Khanna, The growth, fabrication and measurement of terahertz quantum cascade lasers, Ph.D. Thesis, University of Leeds, (2008).

[62] I. C. Bassignana, D. A. Maccquistan and A. J. SpringThorpe, Problems in the use of epitaxial AIAs layers as calibration standards for the Al content of AlGaAs/GaAs layer, in *Institute of Physics Conference Series - Gallium Arsenide and Related Compounds 1991*, G. B. Stringfellow, ed. (Institute of Physics Publishing), pp. 247–250, (1992).

[63] W. G. Breiland and K. P. Killeen, A virtual interface method for extracting growth rates and high temperature optical constants from thin semiconductor films using in situ normal incidence reflectance, *J. Appl. Phys.* 78, 6726, (1995).

[64] C. H. Kuo, S Anand, R. Droopad, K Y. Choi, and G. N. Maracas, Measurement of GaAs temperature-dependent optical constants by spectroscopic ellipsometry, *J. Vat. Sci. Technol. B*, 12, 1214, (1994).

[65] S. Adachi, GaAs, AIAs, and $Al_xGa_{1-x}As$ Material parameters for use in research and device applications, *J. Appl. Phys.*, 58 (3), R1 - R29, (1985).

- [66] S. P. Khanna, M. Salih, P. Dean, A. G. Davies, E. H. Linfield., Electrically tunable terahertz quantum-cascade laser with a heterogeneous active region, *Appl. Phys. Lett.*, 95, 181101, (2009).
- [67] C. Worrall, J. Alton, M. Houghton, S. Barbieri, H. E. Beere, D. Ritchie, and C. Sirtori, "Continuous wave operation of a superlattice quantum cascade laser emitting at 2 THz," *Opt. Express* 14, 171, (2006).
- [68] R. Köhler, A. Tredicucci, F. Beltram, H. E. Beere, E. H. Linfield, A. G. Davies, D. A. Ritchie, R. C. Iotti and F. Rossi, "Terahertz semiconductor-heterostructure laser," *Nature*, 417, 156, (2002).
- [69] S. Kumar, C. W. I. Chan, Q. Hu, and J. L. Reno, "A 1.8-THz quantum cascade laser operating significantly above the temperature of ω/k_B ," *Nature Physics* 7, 166–171, (2011).
- [70] M. S. Vitiello, G. Scamarcio, V. Spagnolo, S. S. Dhillon and C. Sirtori, "Terahertz quantum cascade lasers with large wall-plug efficiency," *Appl. Phys. Lett.* 90, 191115, (2007).
- [71] R. S. Balmer, C. Pickering, A.J. Pidduck, T. Martin, Modelling of high temperature optical constants and surface roughness evolution during MOVPE growth of GaN using in-situ spectral reflectometry, *J. Crystal Growth* 245, 198–206, (2002).
- [72] J. Zhu, L. H. Li, L. Chen, J. Freeman, P. Dean, A. Valavanis, A. G. Davies, E. H. Linfield, Terahertz-frequency quantum cascade lasers with >1-watt output power, UK Semiconductors, Sheffield, (2014).
- [73] L. H. Li, L. Chen, J. Zhu, J. R. Freeman, P. Dean, A. Valavanis, A. G. Davies, E. H. Linfield, THz quantum cascade lasers with output power over 1W, IQCLSW2014 International Quantum Cascade Lasers School and Workshop, (2014).
- [74] A. Valavanis, P. Dean, L. H. Li, A. D. Burnett, J. Keeley, S. Chowdhury, R. Alhathloul, L. Chen, J. Zhu, Y. J. Han, et.al. High-power(>1-Watt) terahertz frequency quantum cascade lasers for stand-off imaging, SET-210 Specialist Meeting on Novel Infrared laser technology for modern battlefield requirements, Salisbury, UK, (2014).
- [75] L. H. Li, J. Zhu, L. Chen, A. G. Davies, E. H. Linfield, The MBE growth and optimization of high performance terahertz frequency quantum cascade lasers, *Optics Express*, Vol. 23, No.3, 2720-2729, (2015).
- [76] Y. Halioua, G. Xu, S. Moudji, L. Li, J. Zhu, E. H. Linfield, A. G. Davies, H. E. Beere, D. A. Ritchie, R. Colombelli, Phase-locked arrays of surface-

emitting graded-photonic-heterostructure terahertz semiconductor lasers, *Optics Express*, Vol. 23, No. 5, (2015).

[77] A. Valavanis, Y. J. Han, N. Brewster, P. Dean, R. Dong, L. Bushnell, M. Oldfield, J. Zhu, L. H. Li, A. G. Davies, B. Ellison and E. H. Linfield, Mechanically robust waveguide integration and beam shaping of terahertz quantum cascade lasers, *Electronics Letters*, Vol. 51, No. 13, (2015).

[78] T. Fobbe, H. Nong, R. Schott, S. Pal, S. Markmann, N. Hekmat, J. Zhu, Y. Han, L. Li, P. Dean, E. H. Linfield, A. G. Davies, A. D. Wieck, and N. Jukam, Improving the out-coupling of a metal-metal terahertz frequency quantum cascade laser through integration of a hybrid mode section into the waveguide, submitted to *Applied Physics Letters*.

[79] J. Zhu, L. H. Li, P. Dean, E. H. Linfield, and A. G. Davies, Growth and Optimization of Terahertz frequency quantum cascade lasers, UK Semiconductors, Sheffield, (2013).

[80] Y. J. Han, L. H. Li, J. Zhu, A. Valavanis, J. R. Freeman, P. Dean, A. G. Davies, E. H. Linfield, Silver-based surface plasmon waveguide for terahertz quantum cascade lasers, IQCSLW2014 International Quantum Cascade Lasers School and Workshop, (2014).

[81] A. Valavanis, Y. J. Han, N. Brewster, P. Dean, R. Dong, L. Bushnell, M. Oldfield, J. Zhu, L. H. Li, A. G. Davies, B. N. Ellison and E. H. Linfield, A robust waveguide integration, beam shaping and heat-sinking scheme for terahertz quantum cascade lasers, *ITQW*, (2015).

[82] D. Rui, Y. Han, I. Kundu, N. Brewster, L. Li, L. Chen, J. Zhu, L. Bushnell, M. Oldfield, et al. Waveguide-integrated terahertz-frequency quantum cascade lasers for trace-gas detection applications, UK semiconductors, (2015).

[83] B. S. Williams, Terahertz quantum cascade lasers, *Nature Photonics*, Vol.1, pp 517-525, (2007).

[84] K. Unterrainer, R. Colombelli, C. Gmachl, F. Capasso, H. Y. Hwang et al., Quantum cascade lasers with double metal-semiconductor waveguide resonators, *Applied Physics Letters*, Vol. 80, No. 17, pp 3060, (2002).

[85] B. S. Williams, S. Kumar, H. Callebaut, Q. Hu and J. L. Reno, Terahertz quantum-cascade laser at $\lambda \approx 100\mu\text{m}$ using metal waveguide for mode confinement, *Applied Physics Letters*, Vol. 83, No. 11, pp 2124, (2003).

[86] J. S. Yu, S. Slivken, A. J. Evans, and M. Razeghi, High-Performance Continuous-Wave Operation of $\lambda \sim 4.6\ \mu\text{m}$ Quantum-Cascade Lasers Above

Room Temperature, IEEE Journal of Quantum Electronics, Vol.44, No.8, pp 747-754, (2008).

[87] A. G. Baca, C. I. H. Ashby, Fabrication of GaAs Devices, Published by: The Institution of Electrical Engineers, London, United Kingdom, (2005).

[88] B. S. Williams, Terahertz quantum cascade lasers, submitted in partial fulfilment of the requirements for the degree of Doctor of Philosophy at Massachusetts Institute of Technology, (2003).

[89] B. S. Williams, S. Kumar, Q. Hu and J. L. Reno, High-power terahertz quantum-cascade lasers, Electronics Letters, Vol. 42, No. 2, (2006).

[90] M. Brandstetter, et. al, High power terahertz quantum cascade lasers with symmetric wafer bonded active regions, Appl. Phys. Lett. 103,171113, (2013).

[91] A. W. M. Lee, Q. Qin, et. al, High-power and high-temperature THz quantum-cascade lasers based on lens-coupled metal-metal waveguide, Optics Letters, Vol. 32, No.19, (2007).

[92] A. W. M. Lee, Q. Qin, S. Kumar, B. S. Williams, Q. Hu, and J. L. Reno, High-power and high-temperature THz quantum-cascade lasers based on lens-coupled metal-metal waveguides, Optics Letters, Vol.32, No.19, 2840-2842, (2007).

[93] J. Faist, Quantum cascade lasers, Chap. 7, (2013).

[94] A. M. Andrews, A. Benz, C. Deutsch, G. Fasching, K. Unterrainer, P. Klang, W. Schrenk, G. Strasser, Doping dependence of LO-phonon depletion scheme THz quantum-cascade lasers, Materials Science and Engineering B, 152-155, (2008).

[95] A. Benz, G. Fasching, A. M. Andrews, and K. Unterrainer, T. Roch, W. Schrenk, and G. Strasser, The influence of doping on the performance of terahertz quantum-cascade-lasers, Optical Terahertz Science and Technology, (2007).

[96] M. Giehler, R. Hey, H. Kostial, S. Cronenberg, T. Ohtsuka, L. Schrottke and H. T. Grahn, Lasing properties of GaAs/ (Al, Ga) As quantum-cascade lasers as a function of injector doping density, Applied Physics Letters, Vol. 82, 671, (2003).

[97] V. D. Jovanović, S. Höfling, D. Indjin, N. Vukmirović, Z. Ikonić, P. Harrison, J. P. Reithmaier, and A. Forchel, Influence of doping density on

electron dynamics in GaAs/ AlGaAs quantum cascade lases, Journal of Applied Physics, Vol. 99, 103106, (2006).

[98] S. Höfling, V. D. Jovanović, D. Indjin, J. P. Reithmaier, A. Forchel, Z. Ikonić, N. Vukmirović, P. Harrison, A. Mirčetić and V. Milanović, Dependence of saturation effects on electron confinement and injector doping in GaAs / Al_{0.45}Ga_{0.55}As quantum-cascade lasers, Applied Physics Letters, Vol. 88, 251109, (2006).

[99] C. Mann, Q. Yang, F. Fuchs, W. Bronner, K. Köhler, and J. Wagner, Influence of injector doping concentration on the performance of InP-based quantum-cascade lasers, IEEE Journal of Quantum Electronics, Vol. 42, No. 10, (2006).

[100] L. Ajili, G. Scalari, M. Giovannini, N. Hoyler and J. Faist, Doping in quantum cascade lasers. II. GaAs/Al_{0.15}Ga_{0.85}As terahertz devices, Journal of Applied Physics, Vol. 100, 043102, (2006).

[101] T. Aellen, M. Beck, N. Hoyler, M. Giovannini, and J. Faist, Doping in quantum cascade lasers. I. InAlAs-InGaAs/InP midinfrared devices, Journal of Applied Physics 100, 043101, (2006).

[102] J. Faist, Wallplug efficiency of quantum cascade lasers: Critical parameters and fundamental limits, Appl. Phys. Lett. 90, 253512, (2007).

[103] E. Mujagić, M. Austerer, S. Schartner, M. Nobile, L. K. Hoffmann, W. Schrenk, G. Strasser, M. P. Semtsiv, I. Bayrakli, M. Wienold, and W. T. Masselink, Impact of doping on the performance of short-wavelength InP-based quantum-cascade lasers, Journal of Applied Physics 103, 033104, (2008).

[104] M. J. Manfra, Molecular beam epitaxy of ultra-high quality AlGaAs/GaAs Heterostructures: Enabling Physics in Low-Dimensional Electronic Systems, arXiv:1309.2717 [cond-mat.mes-hall], (2013).

[105] H. E. Beere, J. C. Fowler, J. Alton, E. H. Linfield, D. A. Ritchie, R. Köhler, A. Tredicucci, G. Scalari, L. Ajili, J. Faist, S. Barbieri, "MBE growth of terahertz quantum cascade lasers," J. of Cryst. Growth, 278, 756, (2005).

[106] G. Scalari, L. Ajili, and J. Faist, et al., Far-infrared ($\lambda \approx 87\mu\text{m}$) bound-to-continuum quantum-cascade lasers operating up to 90 K, Applied Physics Letters, Vol.82, No.19, (2003).

[107] L. H. Li, J. Zhu, L. Chen, A. G. Davies, and E. H. Linfield, The MBE growth and optimization of high performance terahertz frequency quantum cascade lasers, Optics Express 23(3): 2720-2729, (2015).

- [108] P. R. Pukite, G. S. Petrich, S. Batra, and P. I. Cohen, The Meandering of Steps on GaAs (100), *Journal of Crystal Growth* 95, 269-272, (1989).
- [109] H. W. Yu, E. Y. Chang, H. Q. Nguyen, J. T. Chang, C. C. Chung, C. I. Kuo, Y. Y. Wong, and W. C. Wang. Effect of substrate misorientation on the material properties of GaAs/Al_{0.3}Ga_{0.7}As tunnel diodes, *Applied physics letters* 97, 231903, (2010).
- [110] N. Chand and S. N. G. Chu, Origin and improvement of interface roughness in AlGaAs/GaAs heterostructures grown by molecular beam epitaxy, *Applied Physics Letters* 57, 1796, (1990).
- [111] D. C. Radulescu, G. W. Wicks, W. J. Schaff, A. R. Calawa, and L. F. Eastman, Influence of substrate misorientation on defect and impurity incorporation in GaAs/AlGaAs heterostructures grown by molecular-beam epitaxy, *Journal of Applied Physics* 63 (10), (1989).
- [112] L. Sirigu, A. Rudra, E. Kapon, M. I. Amanti, G. Scalari, and J. Faist, A terahertz quantum cascade laser grown by low-pressure metalorganic vapour phase epitaxy, *Applied Physics Letters* 92, 181111, (2008).
- [113] <https://en.wikipedia.org/wiki/Misorientation>.
- [114] G. S. Bales, and A. Zangwill, Morphological instability of a terrace edge during step-flow growth, *Physical Review B*, Vol (41) No.9, (1990).
- [115] J. R. Freeman, J. Madeo, A. Brewer, S. Dhillon, O. P. Marshall, N. Jukam, D. Oustinov, J. Tignon, H. E. Beere, and D. A. Ritchie, Dual wavelength emission from a terahertz quantum cascade laser, *Applied Physics Letters* 96, 051120, (2010).
- [116] <http://thzlabs.tuwien.ac.at/index.php/research/thz-qcls>

List of Abbreviations

AFM	Atomic force microscopy
Al	Aluminium
AES	Auger electron spectroscopy
BEP	Beam equivalent pressure
BTC	Bound-to-continuum
CW	Continuous wave
CSL	Chirped superlattice
DFB	Distributed feedback
DM	Double metal
FDS	Frequency domain spectroscopy
FEL	Fast entry lock
FTIR	Fourier Transform Infrared Spectrometer
Ga	Galium
HR	High reflection
L-I-V	Light output-current-voltage
LO	Longitudinal optical
MBE	Molecular beam epitaxy
MIG	Monitor ion gauge
MOVPE	Metal-organic vapour-phase epitaxy
P-J	output power vs current density
QCL	Quantum cascade laser
QMS	Quadrupole mass spectrometer
Rms	Root mean square
RP	Resonant phonon
RHEED	Reflection high energy electron diffraction
SIMS	Secondary ion mass spectrometry

SISP	Surface-plasmon
SL	Superlattice
SPL	Superlattice
TDS	Time domain spectroscopy
THz	Terahertz
VDP	Van der Pauw
V-J	Voltage vs current density
XPS	X-ray photoelectron spectroscopy

List of Symbols

ϵ_0	the vacuum dielectric constant
e	elementary charge
n_2	refractive index in growth layer
n_1	refractive index in air
n_s	sheet density
B	magnetic field
I	current
V_H	Hall voltage
R_s	sheet resistance
μ	Hall mobility
ρ	bulk resistivity
G	growth rate
G_{QCL}	the average growth rate of the QCL
d	layer thickness
x_{Al}	Aluminium mole fraction
x_{QCL}	the average aluminium composition of the QCL
d_{GaAs}	thickness of the GaAs wells in one period of active region
d_{AlGaAs}	thickness of the AlGaAs wells in one period of active region
t_{AlGaAs}	the growth time of the AlGaAs barriers
t_{GaAs}	the growth time of the GaAs wells
α_w	waveguide loss
$\alpha_w^{\text{undoped}}$	the losses of the undoped waveguide structure
α_w^{abs}	the calculated free carrier absorption
α_m	mirror loss
R_f	front facet reflectivity
R_b	back facet reflectivity

R	Fresnel reflection coefficient at the semiconductor/air interface
R_{SISP}	the facet reflectivity of a SISP THz QCL
β	phase propagation constant
g	gain coefficient
Z	optical matrix element
λ	the wavelength in vacuum
n_{eff}	effective mode index of the waveguide
γ	the broadening of the optical transition
τ^*	normalized lifetime
τ	global transit time
τ_1	lower level life-time
τ_{21}	the intersubband optical-phonon limited relaxation time
T	heat-sink temperature of a THz QCL
T_0	characteristic temperature
g_{th}	threshold gain
Γ	optical confinement factor
J_{th}	threshold current density
J_{max}	maximum current density
n_{AR}	the active region refractive index
P_{max}	the peak output power of a THz QCL

Appendix A Fabrication procedures of THz QCLs

A.1 Fabrication procedures for SISP THz QCLs

No.	Steps	Details
1	Cleaning with acetone	ultrasonic cleaning for 2 minutes at 10% power
2	Cleaning with IPA	ultrasonic cleaning for 2 minutes at 10% power
3	Drying by nitrogen gas	
4	Plasma ashing	50 W/5 minutes
7	Photoresist (S1813) spinning	5000 rpm, 30 s
8	Soft baking	115 °C/1 minute
9	Photolithography	1.5 mW/cm ² for 1 minutes
10	Developing	90 s in MF319
11	DI water rinsing	
12	Nitrogen gas drying	
13	Photolithography for laser ridge	3.9–4 mW/cm ² for 6–7 seconds
14	Soft baking	115 °C/1 minute
15	Developing	75 seconds in MF319
16	DI water rinsing	
17	Nitrogen gas drying	
18	Mounting sample on glass	One drop of photoresist/115 °C/1 minute
19	Ridge etching	Etchant: H ₂ SO ₄ :H ₂ O ₂ :H ₂ O=1:8:40
20	DI water rinsing	
21	Nitrogen gas drying	
22	Measuring surface profile	

23	Removing sample from glass	With acetone
24	1 to 8	Without ultrasonic cleaning
25	Photolithography for bottom contact	3.9–4 mW/cm ² for 6–7 seconds
26	Chlorobenzene Curing	2 minutes without rinsing
27	Nitrogen gas drying	
28	Developing	75 s in MF319
29	DI water rinsing	
30	Nitrogen gas drying	
31	HCL cleaning	Cleaning with HCL: H ₂ O=1:1 for 1 minute
32	AuGeNi for bottom contact	0.65 g/200 nm
33	Lift off	
34	1 to 4	
35	Annealing	430 °C/1 minute
36	Measure bottom contact resistance	R≈5-20 Ω
37	1 to 8	Without ultrasonic cleaning
38	Photolithography for top contact	3.9–4 mW/cm ² for 6–7 seconds
39	26 to 31	
40	AuGeNi for top contact	0.35 g/100 nm
41	Lift off	
42	1-8	Without ultrasonic bath
43	Photolithography	3.9-4 mW/cm ² for 6-7 seconds
44	26 to 31	
45	Over layer metallisation	Ti: 20 nm/Au: 150 nm
46	Lift off	

47	1 to 4	
48	Mounting sample on glass	With soft wax, samples upside down
49	Back side thinning	Etchant: H ₂ SO ₄ :H ₂ O ₂ :H ₂ O=1:8:1
50	DI water rinsing	
51	Nitrogen gas drying	
52	surface profile measuring	By micrometre
53	Removing sample from glass	In Trichloroethylene
54	1 to 4	Without ultrasonic cleaning
55	surface profile measuring	By micrometre
56	1 to 4	In plasma ashing: sample both upside up (5 minutes) and down (5 minutes)
57	Backside metallisation	Ti: 20 nm/Au: 100 nm
58	1 to 4	
59	Annealing (sintering)	270 °C/4 minutes
60	Cleaving	
61	Ceramics mounting	Mount ceramic pads on copper blocks with GE vanish Heat at 100 °C for 5 minutes
62	Indium spreading	Heat the copper blocks at 142 °C with small pieces of Indium on top of it, Spread the Indium when it melts
63	sample loading	Decrease hot plate temperature to 100 °C, mount laser samples on Indium layer, with mirrors parallel to the edge of copper blocks (longer)
64	Wire bonding	Hot plate at 100 °C

A.2 Fabrication procedures for DM THz QCLs

No.	Steps	Details
1	Cleaning with acetone	ultrasonic cleaning for 2 minutes at 10% power
2	Cleaning with IPA	ultrasonic cleaning for 2 minutes at 10% power
3	Drying by nitrogen gas	
4	Plasma ashing	50 W/5 minutes
5	Ti/Au for both wafers	Ti: 20 nm/Au: 600 nm
6	1-4	Without ultrasonic cleaning
7	Thermo-compression bonding	
8	1-4	Without ultrasonic cleaning
9	Samples cleaving	Size: 6 × 6 mm
10	1-4	With ultrasonic cleaning
11	Mount samples on glass slides	
12	SI substrate chemical removing	Remove 80% of the substrate (520 μm)/wet etching (Etchant: H ₂ SO ₄ :H ₂ O ₂ :H ₂ O=1:8:1)
13	SI substrate chemical removing	Citric Acid(100 g with 100 ml water):H ₂ O ₂ =4:1, remove about 30 μm GaAs until the colour changes (AlGaAs, green colour)
14	DI water rinsing	1 minute in beaker / 10 seconds with flow DI water
15	Nitrogen gas drying	
16	1-4	Without ultrasonic bath
17	Remove the etch stop layer	Immerse the sample in (50%) hydrofluoric acid (HF) for ≈15 - 30 seconds, remove the left 550~600 nm GaAs, etchant: H ₂ SO ₄ :H ₂ O ₂ :H ₂ O = 1:8:160
18	Remove samples from	10 minutes in Trichloroethylene

	glass slides	
19	1-4	Without ultrasonic cleaning
	Photoresist spinning	5000 rpm, 30 s
20	Soft baking	115 °C/90 seconds
21	Photolithography for top contact	3.9-4 mW/cm ² for 6-7 seconds
22	Chlorobenzene Curing	2 minutes
23	Developing	75 s in MF319
24	14-15	
25	Plasma ashing	25 W/70 s
26	Ti/Au for top contact	Ti: 20 nm/Au: 150–200 nm
27	Lift off	With Acetone
28	1-4	Without ultrasonic cleaning
29	Photoresist spin-coating	Test vacuum before load sample/5000 rpm/ steps: 4 seconds / 30 seconds
30	Soft baking	115 °C/2 minutes
31	Photolithography for edge bead remove	Exposure: 1.5 mW/cm ² for 2 minutes
32	Developing	90 s
33	14-15	
34	Photolithography for ridge etching	3.9-4 mW/cm ² for 6-7 seconds
35	Soft baking	115 °C/1 minute
36	Developing	75 s in MF319
37	14-15	
38	Mounting sample on glass	one drop photoresist/115 ⁰ C/1 minute
39	Ridge etching	Etchant: H ₂ SO ₄ :H ₂ O ₂ :H ₂ O=1:8:1, Etching thickness< thickness of the active region
40	14-15	

41	Measuring surface profile	
42	Removing sample from glass	In Acetone
43	1-4	Without ultrasonic cleaning
44	Mounting sample (upside down) on glass	With soft wax
45	Back side thinning	Etchant: H ₂ SO ₄ :H ₂ O ₂ :H ₂ O=1:8:1
46	14-15	
47	surface profile measuring	By micrometre
48	Removing sample from glass	10 minutes in Trichloroethylene
49	1-4	Without ultrasonic bath/In plasma ashing: sample both up-side up (5 minutes) and down (5 minutes)
50	Ti/Au for back side	Ti: 20 nm/Au: 150 nm
51	1-4	Without ultrasonic bath
52	Cleaving	
53	1 to 4	Without ultrasonic bath
54	Ceramics mounting	Mount ceramic pads on copper blocks with GE vanish Heat at 100 °C for 5 minutes
55	Indium spreading	Heat the copper blocks at 142 °C with small pieces of Indium on top of it, Spread the Indium when it melts
56	Sample loading	Decrease hot plate temperature to 100 °C, mount laser samples on Indium layer, with mirrors parallel to the edge of copper blocks (longer)
57	Wire bonding	Hot plate at 100 °C